



VILNIUS UNIVERSITY
FACULTY OF CHEMISTRY AND GEOSCIENCES
INSTITUTE OF GEOSCIENCES
DEPARTMENT OF GEOLOGY AND MINERALOGY

Auksė Baltulytė

Geology

Master thesis

**Microstructural analysis of granites and their alterations in
Kabeliai granites: implications from mineral chemical composition**

Scientific adviser
dr. Laurynas Šiliauskas

Vilnius 2025



VILNIAUS UNIVERSITETAS
CHEMIJOS IR GEOMOKSLŲ FAKULTETAS
GEOMOKSLŲ INSTITUTAS
GEOLOGIJOS IR MINERALOGIJOS KATEDRA

Auksė Baltulytė

Geologija

Magistro baigiamasis darbas

Granitų ir jų pakitimų Kabelių granituose mikrostruktūrinė analizė: mineralų cheminės sudėties pritaikymas

Darbo vadovas
dr. Laurynas Šiliauskas

Vilnius 2025

TABLE OF CONTENTS

Abbreviation list	2
1. INTRODUCTION.....	3
2. REGIONAL GEOLOGY	4
3. LOCAL GEOLOGY	7
3.1 The Kabeliai granites.....	7
4. Materials and methods	9
4.1 Sample description	9
4.2 Whole rock chemistry.....	9
4.3 Microscope studies	10
4.3.1 SEM (Scanning electron microscope)	10
4.3.2 EPMA (Electron probe micro-analyser).....	10
4.4 Physicochemical conditions	10
4.4.1 Temperature and pressure.....	11
4.4.2 Oxygen fugacity and H ₂ O contents of magma	12
4.4.3 Halogen fugacity.....	13
5. Results	14
5.1 Whole rock chemistry.....	14
5.2 Microstructural description.....	14
5.3 Mineral Chemistry	20
5.3.1 Major Minerals	20
5.3.2 Secondary minerals.....	27
5.3.3 Accessory minerals.....	29
5.4 Physicochemical conditions	32
5.4.1 Temperature and Pressure	32
5.4.2 Oxygen fugacity and H ₂ O content of magma.....	35
5.4.3 Halogen fugacity.....	38
6. Discussion	39
6.1 Magma emplacement conditions	39
6.2 Late-stage melt crystallisation and post-magmatic alterations.....	39
6.3 The oxygen fugacity, water content and volatiles	40
6.4 Regional context.....	41
7. Conclusions	43
8. Acknowledgements	44

9.	References	45
	Summary.....	52
	Santrauka	53
10.	Appendix	54

ABBREVIATION LIST

Mineral abbreviations according to IMA – CNMNC approved mineral symbols (Warr, 2021):

Ab albite;

Amp amphibole;

Ant anatase;

Ap apatite;

Bt biotite;

Cal calcite;

Chl chlorite;

Hem hematite;

Ilm ilmenite;

Kfs K-feldspar;

Mag magnetite;

Pl plagioclase;

Py pyrite;

Sd siderite;

Ttn titanite;

Qz quartz.

1. INTRODUCTION

The Kabeliai intrusion is approximately 25 km in diameter and is situated between southern Lithuania and northwestern Belarus (Sundblad et al., 1994). It forms part of the larger Marcinkonys complex, which includes a variety of granitoid types along with relicts of amphibolites, paragneisses, and granitic pegmatites (Marfin et al., 1982). These relicts are also found intermixed with granites in the Kabeliai intrusion. According to Sundblad et al. (1994), the granites of the Kabeliai intrusion are K-feldspar granitoids, made up of quartz, plagioclase, K-feldspar, and biotite, exhibiting predominantly peraluminous to metaluminous chemistry. Geochronological studies indicate that the Kabeliai granites crystallised around 1505 ± 11 Ma (Sundblad et al., 1994). Their geological setting, age, and geochemical characteristics are similar to, yet distinct from, those of the Mazury A-type granites and the anorthosite-mangerite-charnockite-granite (AMCG) complexes of northeastern Poland.

The M7 borehole is particularly interesting because it is the only known location within the Kabeliai intrusion where disseminated vein mineralisation containing up to 3% Cu and 1% Mo has been found. However, a significant challenge remains in determining the size of this mineralised body, as the crystalline basement is buried beneath Phanerozoic sediments, with the only information available coming from the drill core.

This thesis aims to investigate the Kabeliai granites from the M7 borehole to reconstruct the conditions of intrusion emplacement and subsequent alteration that might be related to Cu-Mo mineralisation. To date, no comprehensive study has been conducted to reconstruct the magmatic and post-magmatic evolution of this intrusion. The key objectives of this research are:

- To conduct a detailed petrographic and mineral chemical investigation of the selected samples (M7 drill core).
- To determine the intensive parameters of the intrusion emplacement and post-magmatic alterations (T , P , f_{O_2} , etc.).
- To assess the fluid volatile content, based on biotite chemistry and its implications.

This study integrates published and unpublished bulk rock geochemical data from Sundblad et al. (1994), Motuza and Demina. For mineral chemistry, Scanning Electron Microscopy (SEM) with Energy Dispersive Spectroscopy (EDS) was used, and for the detailed investigations of apatite, magnetite-hematite assemblages, Electron Probe Micro-Analysis (EPMA) was applied. Additionally, multiple geothermometric and geobarometric methods were employed: Ti in biotite thermometry (Henry et al., 2005), amphibole thermobarometry (Ridolfi, 2021), zircon saturation thermometry (Watson and Harrison, 1983; Boehnke et al., 2013), apatite saturation thermometry (Harrison and Watson, 1984) and apatite–biotite geothermometer (Zhu and Sverjensky, 1992). Furthermore, calculations of oxygen fugacity (Wones & Eugster, 1965; Ridolfi et al., 2010), water content (Ridolfi et al., 2010), and volatile components (Muñoz, 1984, 1992; Zhu & Sverjensky, 1992; Coulson et al., 2001; Rasmussen & Mortensen, 2013) were performed to constrain the conditions of crystallisation and post-magmatic evolution.

2. REGIONAL GEOLOGY

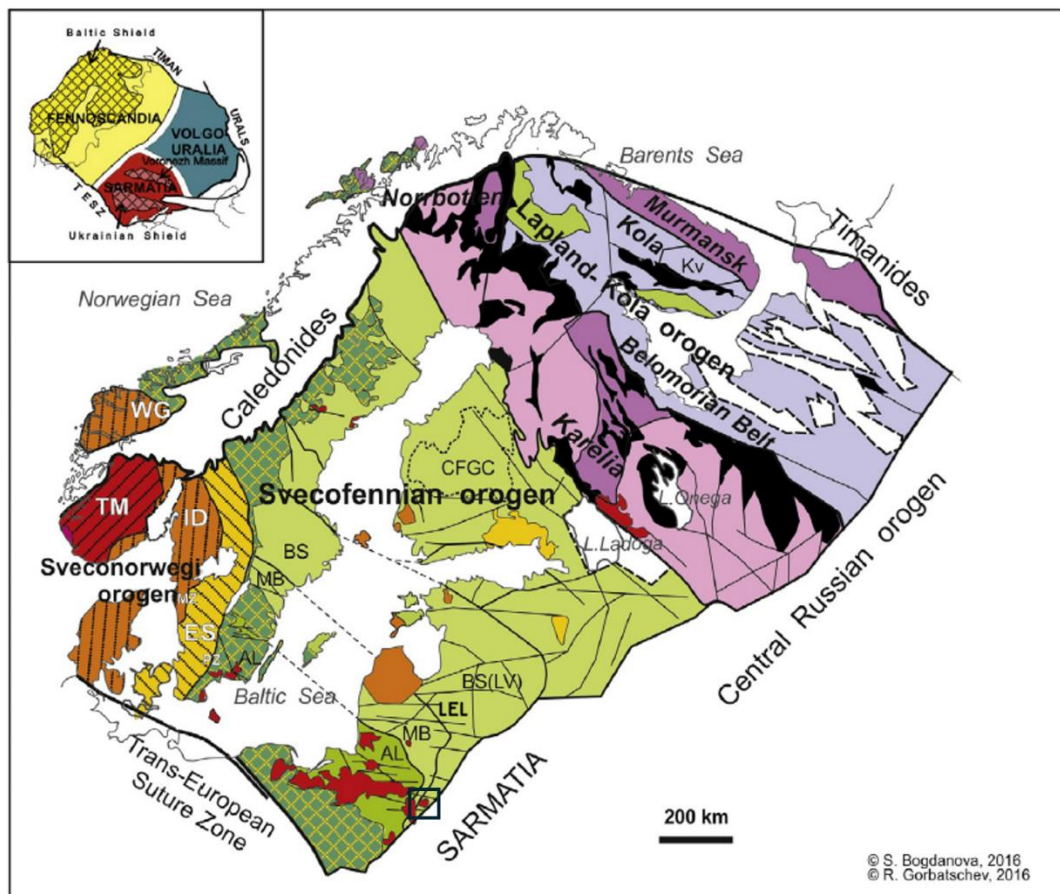
The Fennoscandian segment is a large area in Northern Europe and together with Volgo – Uralia and Sarmatia forms the East European Craton (EEC). It is bounded in the east by Volgo - Sarmatia and in the south by the Trans-European Suture Zone (Fig. 1). Major orogenies of the shield occurred during the Archean and Paleoproterozoic eras (Fig. 1). The growth of Mesoproterozoic crust appears widespread throughout the shield area while the younger Neoproterozoic crust is found only in the western part (Fig. 1). In the western region, the crust has been partly reworked during the Caledonian Orogeny (Fig. 1).

The most extensive crust formation in the Fennoscandian southeast involved a series of episodic events referred to as the Svecofennian Orogen between 1.75 to 2.0 Ga (billion years; Bogdanova and Gorbatschev, 2016). These events include the accretion and collision of microcontinents, oceanic and continental arcs, and the formation of back-arc basins. This led to a gradual consolidation of the continental crust, which continued its growth by establishing a southwest-facing subduction zone after ca. 1.86 Ga (Bogdanova and Gorbatschev, 2016). The oblique convergence of Volgo-Sarmatia and Fennoscandia from the southeast influenced the accretionary growth of the crust in the Svecofennian orogen at 1.80 - 1.82 Ga (Bogdanova et al., 2015). After that, the crustal aggregation stopped at around 1.75 Ga ago, and crustal accretion shifted and continued towards southwest (Bogdanova et al., 2015). The younger Mesoproterozoic AMCG (anorthosite, mangerite, charnockite and mangerite complex) and A-type granitoid magmatism in the southeast part occurred over several episodes: ca. 1.62 - 1.67 Ga, 1.57 - 1.60 Ga, 1.45 – 1.54 Ga (Fig. 1; Bogdanova et al., 2016).

The belt-shaped tectonic domains in the southeastern region of the Fennoscandian segment correlate across the Baltic Sea and shows a trend of domains younging to the southwest (Fig. 1). The Bergslagen/Livonia (BS/LV) domain, with an age of approximately 1.87-1.89 Ga, stretches in southeastern Lithuania and continue in central Latvia, and Estonia, extending into southeastern Sweden (Fig. 1; Bogdanova and Gorbatschev, 2016). The Mid-Baltic Belt (MB), dated at ca. 1.84-1.86 Ga, commences in northern Poland and continues through southern Lithuania, western Latvia, the Baltic Sea (1.85 Ga), Gotland Island, and southeastern-central Sweden (Transscandinavian Igneous Belt-0 (TIB-0) 1.85-1.86 Ga) (Fig. 1; Salin et al., 2019; Salin et al., 2021a; Salin et al., 2021b; Skridlaite et al., 2021). The Amberland (AL) domain (ca. 1.82-1.83 Ga) extends across western Lithuania and northern Poland, continuing through the Baltic Sea (Fig. 1; Bogdanova and Gorbatschev, 2016). The northern part of Poland and some areas of western Sweden belong to the Transscandinavian Igneous Belt 1 (TIB-1) with a dated age of ca. 1.76-1.81 Ga (Fig.1; Bogdanova and Gorbatschev, 2016), while Blekinge (south Sweden part), southern Baltic sea bedrock and

Pomerania (west north Poland) in NE Poland bedrock map are presented as Pomorze-Blekinge domain with an age of 1.75- 1.77 Ga (Krzeminska et al., 2021).

The crust in the southern part of Lithuania and northeastern Poland was intruded by the Mazury AMCG complex approximately 1.50-1.55 billion years ago (Skridlaite et al., 2003b, 2008) and by the Kabeliai pluton at ca. 1.50 billion years ago (Sundblad et al., 1994). About 100 km to the north of the Mazury Complex, another east-west A-type granitoid intrusion ca. 1.45-1.46 Ga in Lithuania (Pramedžiuva, Pamituvys, Gėluva, Nemuno-Žemaičių Naumiesčio) extends westward to the Danish island of Bornholm, which is mainly composed of 1.45 Ga granitoids (Zarins, Johansson, 2009; Johansson et al., 2016). Similar rocks are also found in the Blekinge region of southern Sweden, including Karlshamn intrusions (Johansson et al., 2006; Cecys et al., 2007).



- [a) purple, b) light blue, c) pink] Archean crust: a) 3.5-2.7 Ga, b) 2.8-2.7 Ga, c) reworked within the Lapland-Kola collisional orogen
- [black] Early Paleoproterozoic volcanic belts and sedimentary basins within the Archean crust (2.5-1.95 Ga)
- [a) yellow, b) green] Paleoproterozoic crust: a) 1.95-1.85 Ga, b) 1.83-1.82 Ga
- [green hatched] Transscandinavian Igneous Belt (1.81-1.66 Ga)
- [ES (yellow), ID (orange), TM (red)] Sveconorwegian orogen (1.1-0.95 Ga) including Gothian and Bamble terranes:
ES - Eastern Segment (1.71-1.66 Ga), ID - Idefjorden (1.66-1.55 Ga),
TM - Telemarkian (1.52-1.48 Ga), WG - Western Gneiss Region (1.66-1.63 Ga)
- [a) orange, b) yellow, c) red, d) purple] AMCG- and A-type granitoid magmatism:
a) 1.67-1.62 Ga, b) 1.60-1.57 Ga, c) 1.54-1.45 Ga, d) 0.93-0.92 Ga
- [dashed line] Aulacogens, intracratonic basins (1.5-0.7 Ga)
- [solid line] Boundaries of tectonic domains
- [wavy line] Faults

1 Figure. The Precambrian crust of the Fennoscandian segment. The different colors represent rock ages from the Archean and Proterozoic eons (Bogdanova S. et al., 2016). The investigated area is marked by a square in the picture. The abbreviations for the tectonic domains are: AL – Amberland Belt; BS – Bergslagen lithotectonic unit; BS(LV) – Bergslagen - Livonia unit; CFGC – Central Finland Granitoid Complex (Keitele microcontinent); ES – Eastern segment; ID – Idefjorden terrane; Kv – Keivy tectonic block; LEL – Latvian – East Lithuanian domain; MLD – Mid-Lithuanian domain; MZ – Mylonite Zone; PZ – Protogine Zone; TM – Telemark terrane; WG – Western Gneiss Region.

3. LOCAL GEOLOGY

The studied Kabeliai granites are situated in southern Lithuania. The intrusion has a diameter of approximately 25 km (Stein et al., 1998). Most of the intrusion is situated in the Latvian-East Lithuanian domain (LEL), which is a part of the larger Bergslagen/Livonia unit (Fig. 1). The domain is bordered to the east by the Belarus–Podlasie Granulite (BPG) Belt, which belongs to the Sarmatia segment, and to the west by the Mid-Baltic Belt (MB). The LEL domain crystalline basement may have formed in a subduction-related environment (Bogdanova et al., 2015; Siliauskas et al., 2018). Due to extensional tectonics, the crust was interrupted by several events of different degrees of metamorphism and magmatism between 1.50 - 1.80 Ga (Bogdanova et al., 2016).

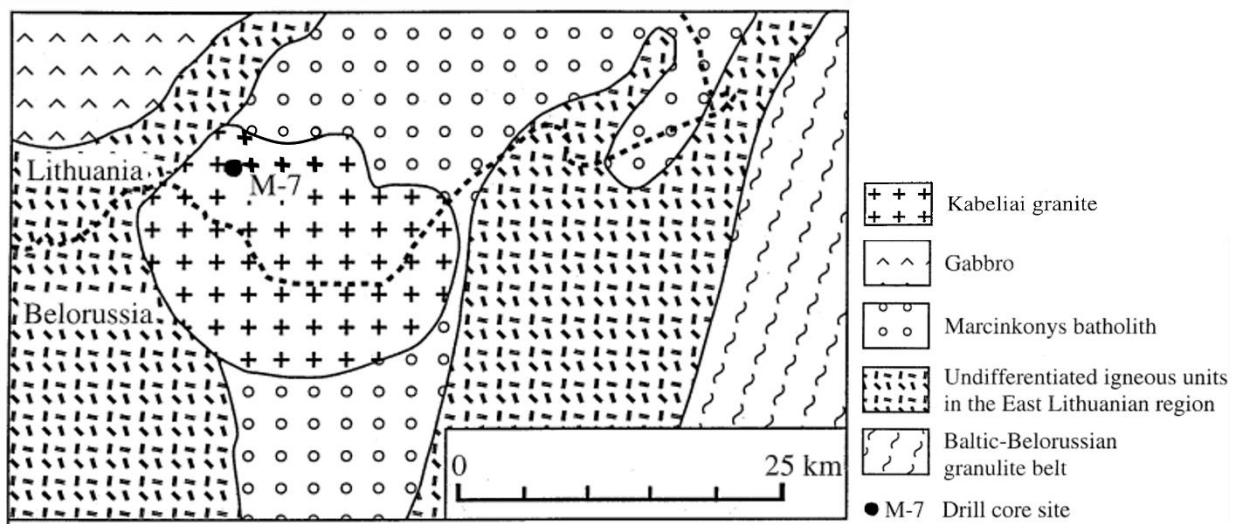
In Latvia, the LEL domain consists of mafic, intermediate to felsic metavolcanics, metasediments and metamorphosed Fe-Mn-rich quartzites (Bogdanova et al., 2015). The dated age of the metavolcanic rock from north Latvia is 1870 ± 13 Ma ago (Mansfeld, 2001). The LEL domain in the south of Lithuania consists of felsic metavolcanic and intrusive rocks and metasediments (marbles, metagreywackes). The dated igneous rocks at ca. 1.87 - 1.89 Ga old are a part of the oldest known crust found in Lithuania (Siliauskas et al. 2018). They are interrupted by the 1.84-1.86 Ga Randamony Complex, which consists of gabbros, diorites, granodiorites, and granites (Skridlaite et al., 2011), marking an Andean-type continental margin established at the time (Bogdanova et al., 2015).

The Paleoproterozoic crust-forming units were intruded by younger Mesoproterozoic AMCG magmas, forming an east-west to southeast-northwest trending line of intrusions. The most studied in the region is the Mazury AMCG complex, which formed in different magmatic phases: an early magmatic phase dated at 1507-1515 Ma (anorthosite emplacement), a main phase between 1496 – 1515 Ma (rapakivi type granites), and a late stage between 1475 – 1489 Ma (granitic aplites, pegmatites, and microgranites; Wiszniewska and Krzemińska, 2021). The Kabeliai granites, located east of the Mazury Complex in southern Lithuania, could belong to the main phase of the Mazury AMCG complex.

3.1 The Kabeliai granites

The Kabeliai intrusion and other Cu-Mo mineralised granite plutons are part of an igneous complex known as the Marcinkonys Batholith (Fig. 2; Marfin et al., 1982). The Marcinkonys batholith granitoids are intermixed with amphibolites, paragneisses, and granitic pegmatites (Marfin et al., 1982). It is located in the south of Lithuania, near the Lithuania-Belarus border (Fig. 1).

The Kabeliai granites are K-feldspar-bearing granitoids composed of quartz, plagioclase, K-feldspar, and biotite. Their composition borders on peraluminous to metaluminous granite-adamellite areas (Sundblad et al., 1994). Two main types of Kabeliai granites can be identified: equigranular, fine-to-medium-grained (0.5–3 mm), and porphyritic, medium-to-coarse-grained (1–5 mm), featuring microcline phenocrysts up to 20 mm in diameter (Sundblad et al., 1994). The unaltered Kabeliai granites have been dated to 1505 ± 11 Ma (Sundblad et al., 1994). Cu-Mo mineralisation was encountered in only one borehole - M7 (Fig. 2). The mineralisation occurs as disseminated vein formations within a quartz-plagioclase host rock (Sundblad et al., 1994). The ore grades show up to 1-3% Cu and 1% Mo (Sundblad et al., 1994). However, the concentrations of other metals, such as Pb, Zn, Sn, W, Bi, and Be, are low (<100 ppm) (Sundblad et al., 1994). The mineralisation age in M7 borehole is dated to 1486 ± 5 Ma (Stein et al., 1998). The mineralisation has been interpreted as a metasomatic alteration (Stein et al., 1998).



2 Figure. Geological map of Precambrian crystalline basement in southern Lithuania and northwestern Belorussia. M7 Borehole position (sources Sundblad K. et al, 1994)

4. MATERIALS AND METHODS

4.1 Sample description

Four thin sections for petrographic studies were selected from the M7 borehole: M7F (277.5 m), M7K (332.5 m), M7M (353 m), and M7S (372 m). The M7F sample is the most altered granite, whereas the alteration intensity in other samples is only local (M7K, M7M, and M7S).

Sample M7F (depth 277.5 m) is a dark grey, fine-grained porphyritic altered granite. The major minerals include quartz (40%), plagioclase (35%), amphibole (10%), biotite (8%), K-feldspar (2%), and accessory minerals (5%). In hand specimen, the quartz appears as glassy, translucent grains, with some phenocrysts reaching up to 1 cm in size, surrounded by a fine-grained groundmass. The plagioclase crystals vary from dark grey to light greenish grey, suggesting possible alteration, while the K-feldspar is not visibly distinguishable. The texture of the rock is characterised by the presence of mafic minerals and accessory phases, which form distinct black and pale-yellow aggregates, creating a spotted pattern.

Sample M7K (depth 332.5 m) is a bright red, fine to coarse-grained equigranular granite containing mafic enclaves/xenoliths. The hosting granite is composed of K-feldspar (50%), plagioclase (30%), quartz (17%), biotite (2%), and accessory minerals (1%). In hand specimen, plagioclase is light grey, with some colour variation, possibly indicating albite alteration of the initial plagioclase. The K-feldspar is a reddish-pink colour, and the quartz appears translucent. Biotite consists of dark, sparsely distributed flakes. The mafic enclave/xenolith is dark grey and coarse-grained, with major minerals including amphibole (50%), biotite (30%), plagioclase (20%), quartz (5%), and accessory minerals (5%). The contact between the mafic enclave and the main part of the rock is gradual. The amphiboles are 0.2-0.5 cm phenocrysts surrounded by the accessory minerals. The dark flakes of biotite are distributed between plagioclase and amphibole. The plagioclases exhibit light grey shades. The accessory minerals are primarily concentrated in or near the micro-mafic enclave, and their abundance decreases towards its centre.

Sample M7M (depth 353 m) is a light grey, coarse-grained porphyritic granite. The major minerals are quartz (50%), plagioclase (30%), K-feldspar (14%), biotite (5%), and accessory minerals (1%). The rock specimen features glassy, translucent quartz phenocrysts (0.5-1 cm). The plagioclases appear white to light grey, and the K-feldspar exhibits a light pink colour. Biotite is present in black flakes concentrated in clusters with accessory minerals, forming dark mineral aggregates between plagioclase grains.

Sample M7S (depth 373 m) is a bright red, coarse-grained porphyritic granite. The major minerals are quartz (30%), K-feldspar (35%), plagioclase (27%), biotite (7%), and accessory minerals (1%). The rock specimen contains large phenocrysts of reddish to pinkish K-feldspar measuring 1-2 cm and 0.5-1 cm glassy, translucent quartz. The plagioclases display lighter colour variations, possibly indicating partial alteration. Biotite appears in black flakes, forming clusters with accessory minerals. Around the mafic minerals, light-coloured aureoles suggest metasomatic processes.

4.2 Whole rock chemistry

In this research, bulk rock chemistry published by Sundblad et al. (1994) and provided by Motuza G. were used. One bulk rock chemistry analysis (M7/293.351) was provided by Demina O. (unpublished data). The bulk rock chemistry is presented in Appendix 1. The samples from different boreholes in Kabeliai intrusion were picked up to represent the lithological variety of the intrusion.

From the available data, analyses of the altered rocks (analysis from M7/293.351 and M7/305.4) were collected closest to the interval of the investigated thin sections.

4.3 Microscope studies

4.3.1 SEM (Scanning electron microscope)

The four polished thin sections were carbon-coated and studied using a Scanning Electron Microscope (SEM) Quanta 250 at the Nature Research Centre, Vilnius, Lithuania. A backscattered electron (BSE) detector was used for the images. The images were further used to investigate microstructures, porosity, microfractures, and mineral zonation.

The chemical compositions of the minerals were acquired using SEM with the EDS (energy diffraction spectrometer) detector X-Max, the INCA x-stream digital pulse processor and the INCA Energy EDS software. The beam current of 1.0 nA and the accelerating voltage of 20 kV were used during the analyses.

The Cathodoluminescence (CL) detector was used for examination of apatites to check their zonation patterns. The beam current was 1.0 nA and the accelerating voltage was 15 kV. The images were analysed to select points for the Electron Probe Micro-Analyser (EPMA) investigation.

4.3.2 EPMA (Electron probe micro-analyser)

An Electron Probe Microanalyser (EPMA, Camexa SX100) at the Institute of Geochemistry, Mineralogy and Petrology, Warsaw University, Poland, was used to determine the chemical composition of the selected apatite and magnetite minerals. The mineral analyses are presented in Appendix 2 (I, K, L).

The beam currents of 4 nA, 10 nA, and 30 nA, along with a voltage of 15 kV, were used for apatite analyses. The condition of 4 nA at 15 kV was used for F, Ca, P; 10 nA at 15 kV was used for Na, Si, Cl, S, Fe, Al; and 30 nA at 15 kV was used for Mn, Sr, Y, As, La, Ce, Pr, Nd, Mg, Sm. For the elements F, Ca, P, Na, Si, Cl, S, Fe, Al, Mn, and Mg, the Ka line was used. The Sr, Y, As, La, Ce, Pr, Nd, and Sm were analysed using the La line. The average detection limits were 0.338 wt.% for F, 0.081 wt.% for Ca, 0.044 wt.% for P, 0.041 wt.% for Na, 0.024 wt.% for Si, 0.026 wt.% for Cl, 0.02 wt.% for S, 0.075 wt.% for Fe, 0.023 wt.% for Al, 0.04 wt.% for Mn, and 0.017 wt.% for Mg. The average detection limits for three trace elements and five rare earth elements (REEs) were 375 ppm for Sr, 434 ppm for Y, 479 ppm for As, 439 ppm for La, 400 ppm for Ce, 218 ppm for Pr, 428 ppm for Nd, and 1077 ppm for Sm.

For the magnetites and hematites, a beam current of 15 nA and an accelerating voltage of 15 kV were used. For the elements Mg, Al, Si, Fe, Mn, V, K, Ca, S, P, Cr, Ti, Ni, Na, Co, Cu, Zn, the Ka line was used. The Nb and Zr were analysed using the La line. The average detection limits were 0.034 wt.% for Mg, 0.023 wt.% for Al, 0.027 wt.% for Si, 0.122 wt.% for Fe, 0.098 wt.% for Mn, 0.083 wt.% for V, 0.026 wt.% for K, 0.026 wt.% for Ca, 0.027 wt.% for S, 0.026 wt.% for P, 0.022 wt.% for Cr, 0.11 wt.% for Ti, 0.111 wt.% for Ni, 0.057 wt.% for Na, 0.13 wt.% for Co, 0.139 wt.% for Cu, 0.216 wt.% for Zn, 0.059 wt.% for Nb, and 0.082 wt.% for Zr.

4.4 Physicochemical conditions

4.4.1 Temperature and pressure

Temperature (T) and pressure (P) calculations were carried out with the purpose of understanding rock formation conditions. Five different geothermometers were used: Ti in biotite thermometry, amphibole thermobametry, apatite and zircon saturation thermometry and apatite – biotite geothermometer.

The Ti in biotite geothermometry by Henry et al. (2005) was used for the investigated biotites. This geothermometry can be applied to igneous and metamorphic rocks where silica and titanium are buffered by quartz and Ti-phase (ilmenite or rutile), respectively. This thermometry was chosen because of the strong influence of temperature on the incorporation of the element Ti. The geothermometric expression by Henry et al. (2005):

$$T = \{[\ln(Ti) - a - c(X_{Mg})] / b\} \cdot 0.333 \quad (1)$$

T is the temperature in degrees Celsius, Ti is the number of atoms per formula unit (apfu) normalized on the basis of 22 O atoms, X_{Mg} is $Mg/(Mg + Fe)$, $a = -2.3594$, $b = 4.6482 \times 10^{-9}$ and $c = -1.7283$. The calibration range for this expression is $X_{Mg} = 0.275-1.000$, $Ti = 0.04-0.60$ apfu, and $T = 480-800$ °C with a precision of $\pm 12-24$ °C, at the higher and lower temperature spectra, respectively (Henry et al., 2005).

For pressure calculations in M7 biotites Uchida et al. (2007) empirical equation was used. In granitic rocks, the TAl content of biotite can be a useful tool for distinguishing between mineralised and non-mineralised granitic rocks (Uchida et al., 2007). In the study by Uchida et al. (2007), a strong correlation was recognised between the TAl content of biotite and the solidification pressure of granitic rocks. The empirical equation:

$$P (kb) = 3.03 \times {}^TAl - 6.53 (\pm 0.33) \quad (2)$$

TAl designates the total Al content in biotite on the basis O = 22.

Amphibole thermobarometry was applied following Ridolfi (2021) and for the pressure estimations, calibration of Ridolfi and Renzulli, (2012) was used. The updated supplementary Amp-TB2 thermobarometry Excel sheet by Ridolfi (2021) was used for the studied amphiboles from M7. This thermobarometry was chosen for its wide applicability to both igneous and metamorphic amphiboles, as well as its improved calibration, providing more accurate pressure and temperature estimations.

Watson and Harrison (1983) and Boehnke et al. (2013) equations were used to calculate the zircon saturation thermometry. The estimation is crucial for understanding the evaluation of the timing and amount of zircon precipitation from cooling magma, as well as the tendency for zircon to remain in the residue or be consumed during anatexis (Watson and Harrison, 1984). The principle of calculating is using bulk rock chemistry to determine the zirconium content in the silicate melts. The parameter M [= (Na+K+2Ca)/(Al*Si)] is a good compositional proxy for the mechanism of zircon solution (Boehnke et al., 2013).

The calculations were performed using the GCDkit version 6.2 R package “Saturnin” by Janousek et al. (2006). The expression by Watson and Harrison (1983):

$$D_{Zr} = 497644/Zr \quad (3)$$

$$T_{Zr\text{sat.}} = 12900/\ln(D_{Zr}) + 3.8 + 0.85(M-1) - 273.15 \quad (4)$$

Zr – observed Zr concentrations; M - cationic ratios; T Zr.sat. zircon saturation temperatures in °C.

The expression by Boehnke et al. (2013):

$$\ln D_{Zr} = (10108 \pm 32)/T - (1.16 \pm 0.15)(M-1) - (1.48 \pm 0.09) \quad (5)$$

where D_{Zr} is the distribution coefficient of Zr between zircon and melt and the errors are at one sigma; T temperature in Kelvins.

The apatite saturation thermometry was used by Harrison and Watson (1984). The calculations were performed using the GCDkit R version 6.2 package “Saturnin” by Janousek et al. (2006). It uses bulk rock major element composition: SiO₂ and P₂O. The melt composition and temperature control apatite solubility. The P diffuses slowly in the felsic magmas, while in water-rich magmas, phosphorus diffusion is more intense. This thermometry is important due to the applicability of igneous apatite in concentrating rare earth elements (REEs) and tracking the cooling history of magmatic systems. The expression by Harrison and Watson (1984):

$$\ln(D_P) = 8400 + 26400(SiO_2 - 0.5)/T - 3.1 - 12.4(SiO_2 - 0.5) \quad (6)$$

$$P_2O_5.HW = 42/D_P \quad (7)$$

T = absolute temperature (K), 'D_P' = distribution coefficient for phosphorus between apatite and melt and 'SiO₂' is the weight fraction of silica in the melt, SiO₂ wt. %/100.

The apatite-biotite geothermometer is based on the exchange of F and OH between these two minerals. The apatite–biotite geothermometer was used by Zhu and Sverjensky (1992):

$$T (\text{°C}) = (8852 - 0.024P(\text{bars}) + 5000X_{Fe}/1.987\ln K_D^{Ap/Bt_F} + 3.3666) - 273.15 \quad (8)$$

X_{Fe} is the Fe fraction in biotite and K_D^{Ap/Bt_F} is the partition coefficient for F between apatite and biotite (Zhu and Sverjensky 1991, 1992).

4.4.2 Oxygen fugacity and H₂O contents of magma

The Oxygen fugacity $f(O_2)$ is an important control of multivalent elements (like Cu, Fe, Au, Ti, V, etc.) precipitation and behaviour in magmatic–hydrothermal processes (Burnham et al., 2021). Changes in oxygen fugacity can control the precipitation of ore-forming minerals from the hydrothermal solution or nucleation in crystallising magma. In this study, log(f_{O_2}) was calculated using biotite and amphibole compositions.

Oxygen fugacity ($f(O_2)$) estimations based on biotite composition were performed using an expression by Wones and Eugster (1965). The formula for Oxygen fugacity (log(f_{O_2})) by Wones and Eugster (1965):

$$\log(f_{O_2}) = -24912/T + 14.41 + 0.019(P-1)/T \quad (9)$$

T is the temperature (K), P is the pressure in bars. The numbers: 24912, 14.41, and 0.019 are A, B, C values of the chosen calculation buffer (Wones and Eugster, 1965). In this study, Fe₂O₃-Fe₃O₄ buffer was picked.

The oxygen fugacity and the H₂O content in the melt for the amphiboles were estimated using expressions by Ridolfi, (2021). The formulas for calculations by Ridolfi, (2021):

$$\Delta\text{NNO} = -10.321*\text{Al}^{\text{IV}} + 4.470*\text{Al}^{\text{IV}} + 7.551*\text{Ti} + 5.463*\text{Fe}^{3+} - 4.739*\text{Mg} - 7.203*\text{Fe}^{2+} - 17.561*\text{Mn} + 13.762*\text{Ca} + 13.756*\text{Na}^{\text{A}} + 27.594*\text{K} \quad (R^2=0.951) \quad (10)$$

$$\ln(\text{H}_2\text{O}_{\text{melt}}) = -1.375*\text{Al}^{\text{IV}} + 1.710*\text{Al}^{\text{IV}} + 0.859*\text{Ti} + 1.189*\text{Fe}^{3+} - 0.676*\text{Mg} - 0.390*\text{Fe}^{2+} - 6.402*\text{Mn} + 2.549*\text{Ca} + 1.371*\text{Na}^{\text{A}} + 1.257*\text{K} \quad (R^2=0.988) \quad (11)$$

Al^{IV} to K were the atoms per formula unit as calculated using the 13-cations method (Ridolfi, 2021).

4.4.3 Halogen fugacity

The F and Cl enter the biotite structure, replacing the OH⁻ anion. Measured halogen content in biotite can be related to fluid/melt halogen fugacity ratios at the given temperature (Munoz J. L., 1984; 1992). By using halogen fugacity ratios, it is possible to estimate the volatiles change in a magmatic-hydrothermal system. The volatile component amounts can be related to mineralisation.

The equations for calculation log(f_{H2O}/f_{HF}), log(f_{H2O}/f_{HCl}), and log(f_{HF}/f_{HCl}) (Munoz, 1984, 1992; Zhu and Sverjensky, 1992; Coulson et al., 2001; Rasmussen and Mortensen, 2013) are:

$$\log(f_{\text{H}_2\text{O}}/f_{\text{HF}})_{\text{fluid}} = 1000/T(2.37 + 1.1X_{\text{Mg}}) + 0.43 - \log(X_{\text{F}}/X_{\text{OH}}) \quad (12)$$

$$\log(f_{\text{H}_2\text{O}}/f_{\text{HCl}})_{\text{fluid}} = 1000/T(1.15 - 0.55X_{\text{Mg}}) + 0.68 - \log(X_{\text{Cl}}/X_{\text{OH}}) \quad (13)$$

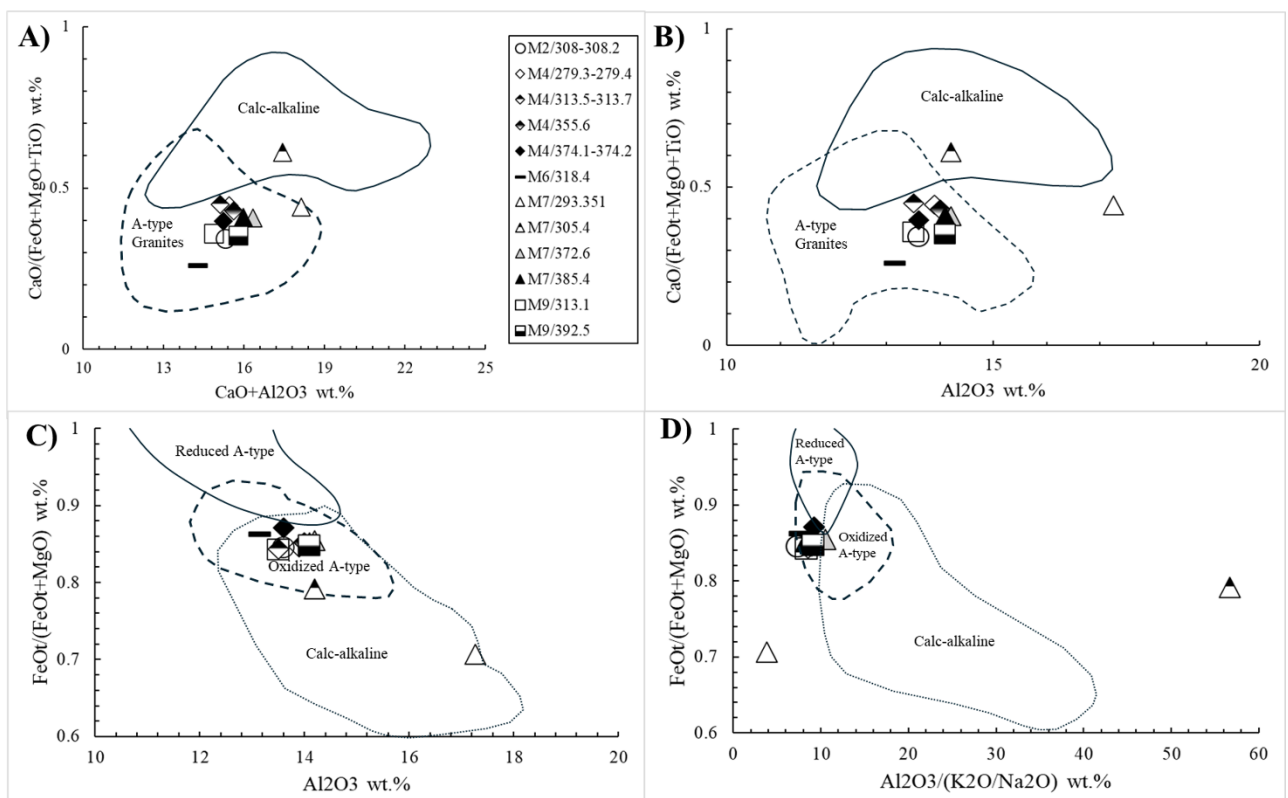
$$\log(f_{\text{HF}}/f_{\text{HCl}})_{\text{fluid}} = 1000/T(1.22 + 1.65X_{\text{Mg}}) + 0.25 + \log(X_{\text{F}}/X_{\text{Cl}}) \quad (14)$$

T is the temperature (Kelvin); X_{Mg} is Mg/sum of octahedral cations, X_F, X_{Cl}, and X_{OH} are mole fractions of F, Cl, and OH in the hydroxyl site of biotite.

5. RESULTS

5.1 Whole rock chemistry

The bulk chemistry of granites from the Kabeliai intrusion (See Appendix 1; Sundblad et al., 1994; Motuza G.; Demina O., unpublished data) was plotted in an A-type granite discrimination plot (Dall'Agnol and Oliveira, 2007) that allows distinguishing calc-alkaline and oxidized or reduced A-type granite (Fig. 3). The Kabeliai intrusions rocks plots in the A-type granites field (Fig. 3A-B) and oxidized A-type (Fig. 3C-D). Most analyses plot closely together without scattering (Fig. 3), except for sample M6/318.4, which is plotted slightly apart from the group (Fig. 3A-B). The analyses from altered rocks (M7/293.351 and M7/305.4) plot separately from the group, often outside the granite fields (Fig 3.A-D).



3 Figure. A) - Whole-rock $\text{CaO}/(\text{FeOt}+\text{MgO}+\text{TiO}_2)$ vs. $\text{CaO} + \text{Al}_2\text{O}_3$, B) - $\text{CaO}/(\text{FeOt}+\text{MgO}+\text{TiO}_2)$ vs. Al_2O_3 , C) - $\text{FeOt}/(\text{FeOt}+\text{MgO})$ vs. Al_2O_3 , and D) - $\text{FeOt}/(\text{FeOt}+\text{MgO})$ vs. $\text{Al}_2\text{O}_3/(\text{K}_2\text{O}/\text{Na}_2\text{O})$ diagrams (Dall'Agnol and Oliveira, 2007) of the Kabeliu granites (whole rock chemistry by Sundblad et al, 1994; Motuza; Demina, unpublished data). A) and B) distinguish A-type granites from calc-alkaline granites; C) and D) differentiate between oxidised and reduced A-type granites and calc-alkaline granites. The legend in A) is the same for B), C), and D).

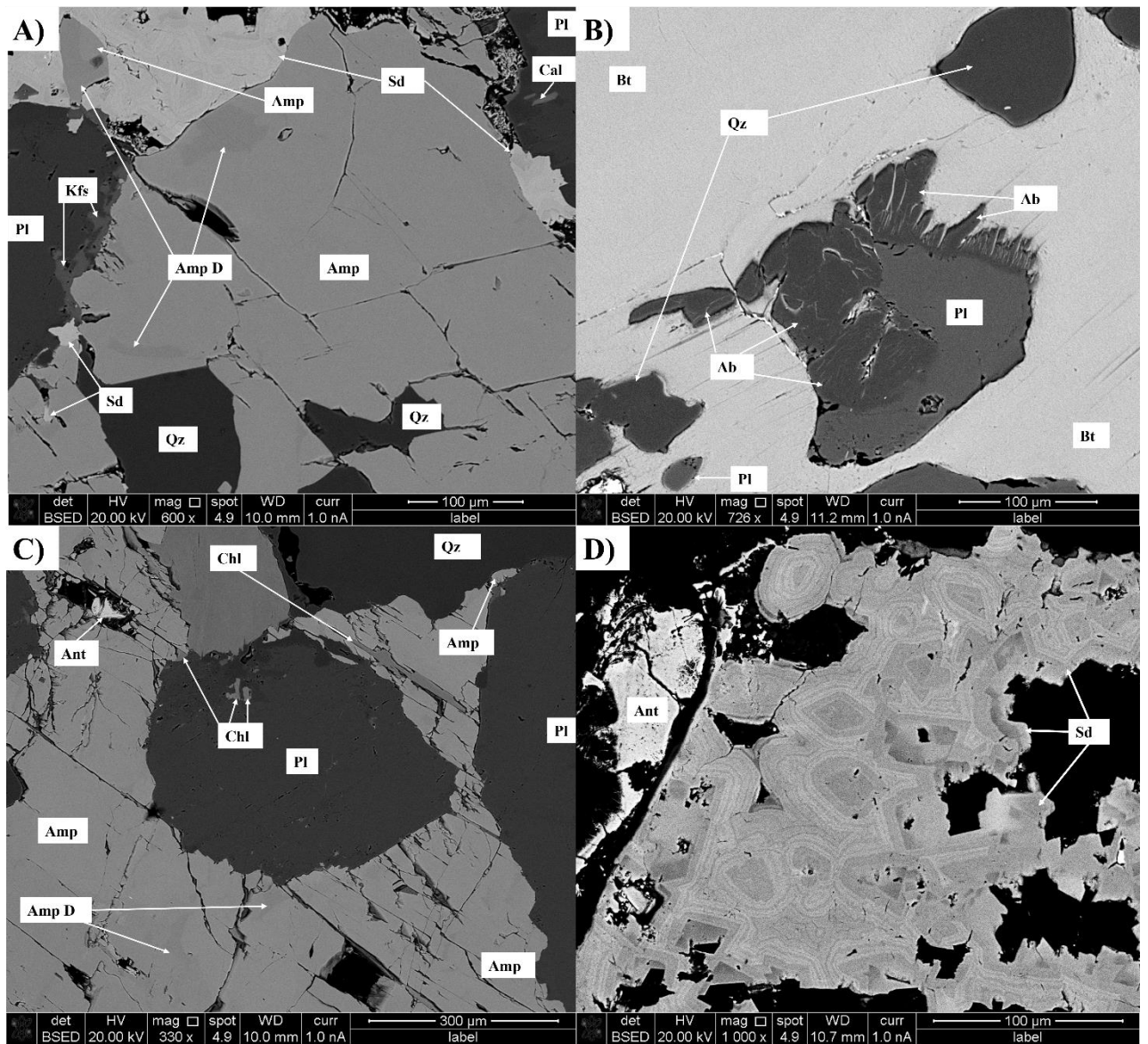
5.2 Microstructural description

The petrographic investigation was conducted using SEM with BSE, EDS and CL detectors. The granites are composed of the following minerals: plagioclase, biotite, quartz, amphibole, titanite, ilmenite, anatase, pyrite, muscovite, chlorite, apatite, magnetite, hematite, calcite, siderite, epidote.

M7F – 277.5

The sample M7F – 277.5 is dark – grey, fine-grained porphyritic granite. Major minerals are quartz (40%), plagioclase (35%), amphibole (10%), biotite (8%), K-feldspar (2%) and accessory minerals (5%). The accessory minerals are titanite, ilmenite, anatase, calcite, epidote, siderite, pyrite, sphalerite and zircon. They are mostly found in the interstitial spaces between plagioclase, amphibole, biotite and quartz. The secondary minerals (chlorite, calcite, siderite and epidote) were identified as forming in the amphiboles and biotites. The matrix is composed of biotite, K-feldspar, plagioclase, quartz, secondary and accessory minerals while bigger phenocrysts (3-5mm) are quartz, amphibole and plagioclase.

Plagioclases are subhedral-to-anhedral with irregular boundaries. The grain sizes vary from 0.2 to 3 mm. Albitionization strongly affects the plagioclases, as seen in the BSE image (Fig. 4B). The inclusions in plagioclases are biotite, chlorite, K-feldspar and titanite. The K-feldspar in M7F is



4 Figure. Representative SEM BSE images of the investigated thin section M7F-277.5. A) – Subhedral amphibole with dark patches surrounded by plagioclase and siderite. K-feldspar forming in the plagioclase rims and siderite forming in the amphibole; B) - Plagioclase and quartz inclusions in the biotite. Plagioclase rims are changing into albite; C) – Plagioclase grain surrounded by anhedral amphibole. Some of the amphiboles cleavage planes are filled with chlorite; D) Oscillatory siderite and close to it anhedral anatase grain. The abbreviations are explained in the abbreviation list. Amp D – amphibole dark

anhedral with irregular boundaries. The grains are small with 0.1 mm and are interstitial between amphibole, plagioclase, and biotite, or forming at the rims of the plagioclase. The quartz is subhedral and anhedral with grain sizes varying from 0.1 to 5 mm. The biotites are subhedral and tabular with grain sizes from 0.5 mm and smaller. In the cleavage planes are forming calcite and siderite. Biotite often hosts inclusions of plagioclases, quartz and apatite. Some of the biotite grains are changed to calcite, siderite and epidote. The amphiboles are subhedral-to-anhedral with grain sizes 0.1-3 mm. The grains are changing to chlorite, siderite, calcite and epidote. Chlorite, calcite and siderite are forming along the amphibole cleavage planes. Amphibole hosts inclusions of quartz, biotite and apatite. In the BSE image, the otherwise homogeneous amphibole grains show irregular light (L) and dark (D) patches of grayscale intensity (Fig. 4 A, C). Patches are of variable sizes and distributed with no obvious consistency. The titanite grains are euhedral with sizes of 0.3 mm and smaller. They are partly replaced by ilmenite and anatase. The apatites are euhedral and subhedral with sizes of 0.02-0.5 mm. In the CL images apatite has patchy zonation. The siderite is filling 0.01 – 0.2 mm pores, is anhedral and exhibits oscillatory zoning (Fig. 4D). The grain sizes vary from 0.3 mm and smaller. The pyrite and sphalerite are anhedral with sizes of 0.01 mm.

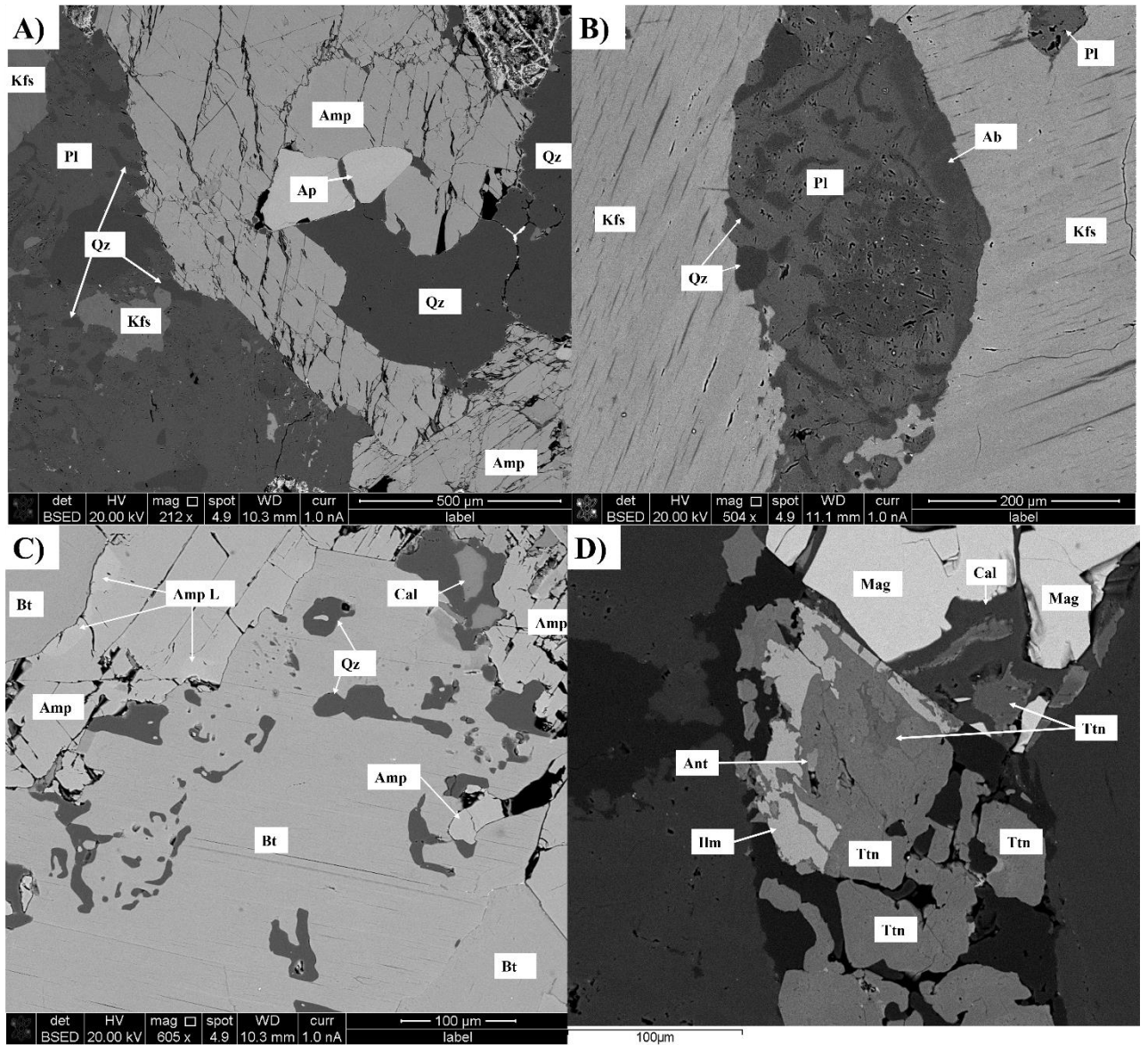
M7K – 332.5

Sample M7K (depth 332.5 m) features bright red, fine to coarse-grained equigranular granite with small mafic enclaves/xenoliths. The primary mineral composition of the rock includes K-feldspar (50%), plagioclase (30%), quartz (17%), biotite (2%), and accessory minerals (1%). The accessory minerals consist of apatite and titanite. The chlorite and calcite are forming after biotite. The matrix is composed of plagioclase, quartz, biotite, chlorite, apatite and titanite, while phenocrysts are K-feldspar, plagioclase, and quartz.

Plagioclases are subhedral and anhedral, exhibiting irregular boundaries. The grain sizes range from 2 to 5 mm, with most grains characterised by fluid trails and often hosting inclusions of biotite, quartz, K-feldspar, and calcite. Plagioclase shows signs of albitisation, and some grains display myrmekite texture (Fig. 5B). The K-feldspar is subhedral, with grain sizes ranging from 2 to 5 mm, and exhibiting a perthite texture with plagioclase lamellae (Fig. 5B). These grains contain minor inclusions of plagioclase, biotite, and quartz. The quartz is anhedral, measuring between 0.1 and 5 mm. The biotites are subhedral and tabular, with grain sizes varying from 0.5 mm and smaller. Titanite is anhedral, with size of 0.05 and 0.1 mm. The apatite is anhedral, ~0.05 mm, and exhibits a patchy cathodoluminescence pattern.

The mafic enclave/xenolith is dark grey and coarse-grained, comprised of major minerals: amphibole (50%), biotite (30%), plagioclase (20%), quartz (5%), and accessory minerals (5%). The accessory minerals include apatite, magnetite, titanite, anatase, ilmenite, and calcite. The chlorite and calcite develop within the amphibole and biotite. The matrix is composed of biotite, plagioclase, K-feldspar, chlorite, calcite, ilmenite, anatase, magnetite, while phenocrysts are amphiboles, apatite, and titanite.

Plagioclases are anhedral, exhibiting irregular boundaries. The grain sizes range from 0.1 to 0.5 mm, with most grains often hosting inclusions of biotite, quartz and calcite. Plagioclase some grains display myrmekite texture (Fig. 5A). The quartz is anhedral, measuring between 0.01 to 0.2 mm. The biotites are subhedral and tabular, with grain sizes varying from 0.5 mm and smaller. The biotite rims exhibit a simplectite texture featuring quartz vermicular intergrowths (Fig. 5C). The amphibole forms subhedral grains with sizes ranging from 2 to 5 mm, hosting various inclusions of biotite, apatite, titanite, ilmenite, and calcite. These grains are homogeneous and display distinct patches of darker



5 Figure. Representative SEM BSE images of the investigated thin section M7K – 332.5. A) - Subhedral amphibole and plagioclase with vermicular quartz intergrowths myrmekite; B) Anhedral plagioclase with vermicular quartz intergrowths myrmekite and surrounded by K-feldspar phenocryst with thin strips of plagioclase forming perthite; C) Anhedral biotite with simplectite texture forming in the rims and surrounded by amphibole. Subhedral amphibole have lighter colour patches; D) – Titanite grain being replaced by ilmenite, anatase, magnetite, and calcite. The abbreviations are explained in the abbreviation list. Amp L – amphibole light.

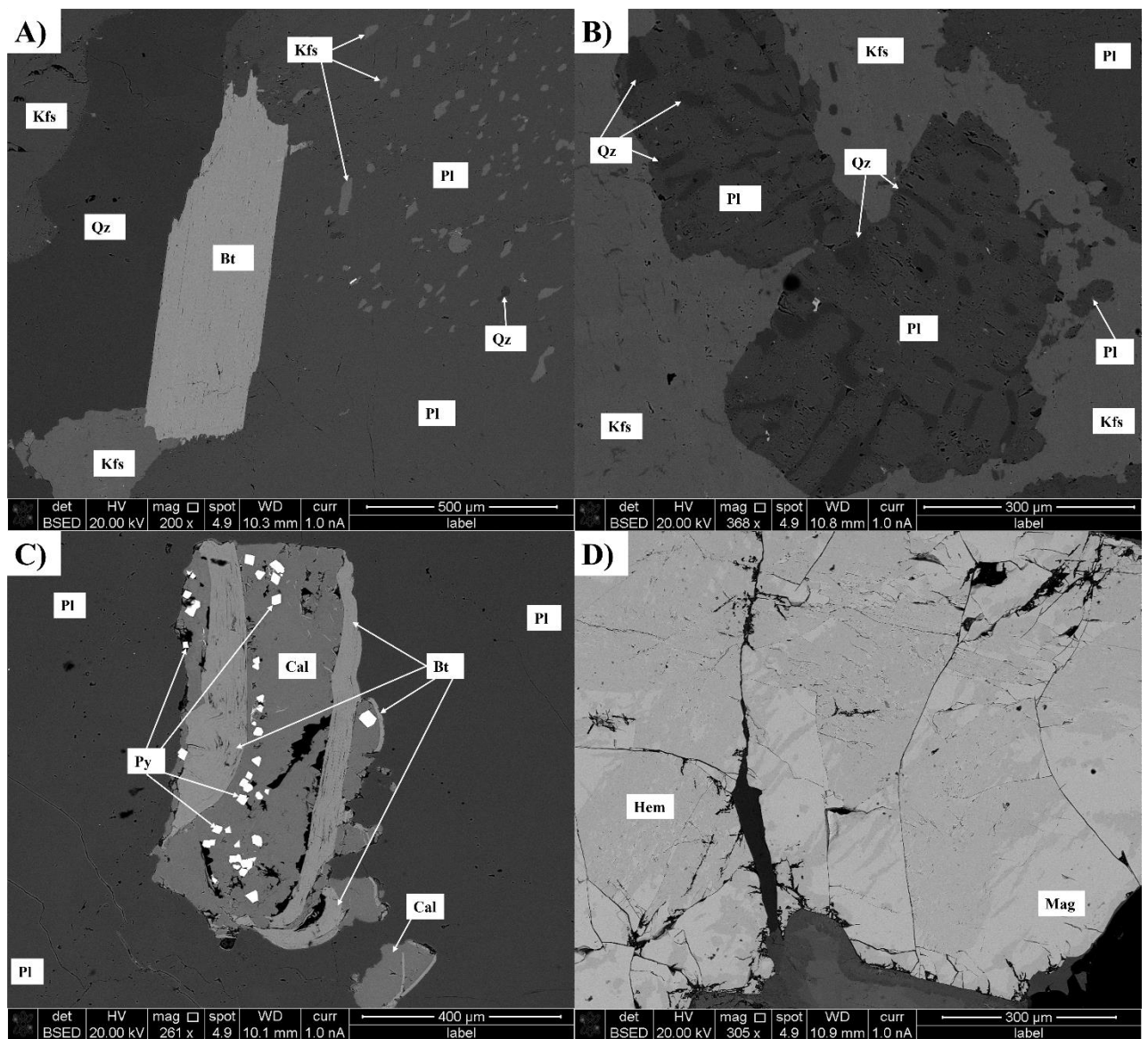
and lighter areas (Fig. 5C). The titanite appears euhedral and subhedral, measuring between 0.1 and 1 mm. Some grains transform into ilmenite (0.05 mm and smaller) and anatase (0.01 mm) (Fig. 5D). Magnetite is anhedral, with a size of 0.1 mm, while calcite is also anhedral, measuring 0.1 mm. Apatite can be subhedral or anhedral, ranging from 0.2 to 0.5 mm, and appears patchy in CL images.

M7M – 353

M7M (depth 353 m) is light grey, coarse-grained porphyritic granite. The major minerals include quartz (50%), plagioclase (30%), K-feldspar (14%), biotite (5%), and accessory minerals

(1%). The accessory minerals consist of pyrite, magnetite, hematite, titanite, anatase, and apatite. The secondary minerals present are pyrite, calcite and chlorite. The matrix is composed of quartz, biotite, K-feldspar, secondary and accessory minerals, while phenocrysts are K-feldspar, quartz, and plagioclase.

The plagioclase is subhedral with sizes ranging from 2 to 5 mm. The grains appear homogeneous in the BSE images. Some grains exhibit myrmekite and antiperthite textures (Fig. 6A, B). The K-feldspar is anhedral, measuring between 0.1 to 3 mm. It displays perthite texture and contains inclusions of quartz and plagioclase. The quartz occurs as subhedral and anhedral grains with sizes up to 0.1-5 mm. The biotite grains are euhedral and subhedral, ranging in size from 0.5 to 1 mm (Fig. 6A). In the BSE images, the alteration of biotite to chlorite is visible. The titanite grains are subhedral and measure between 0.1 and 0.5 mm. These grains are being replaced by anatase,

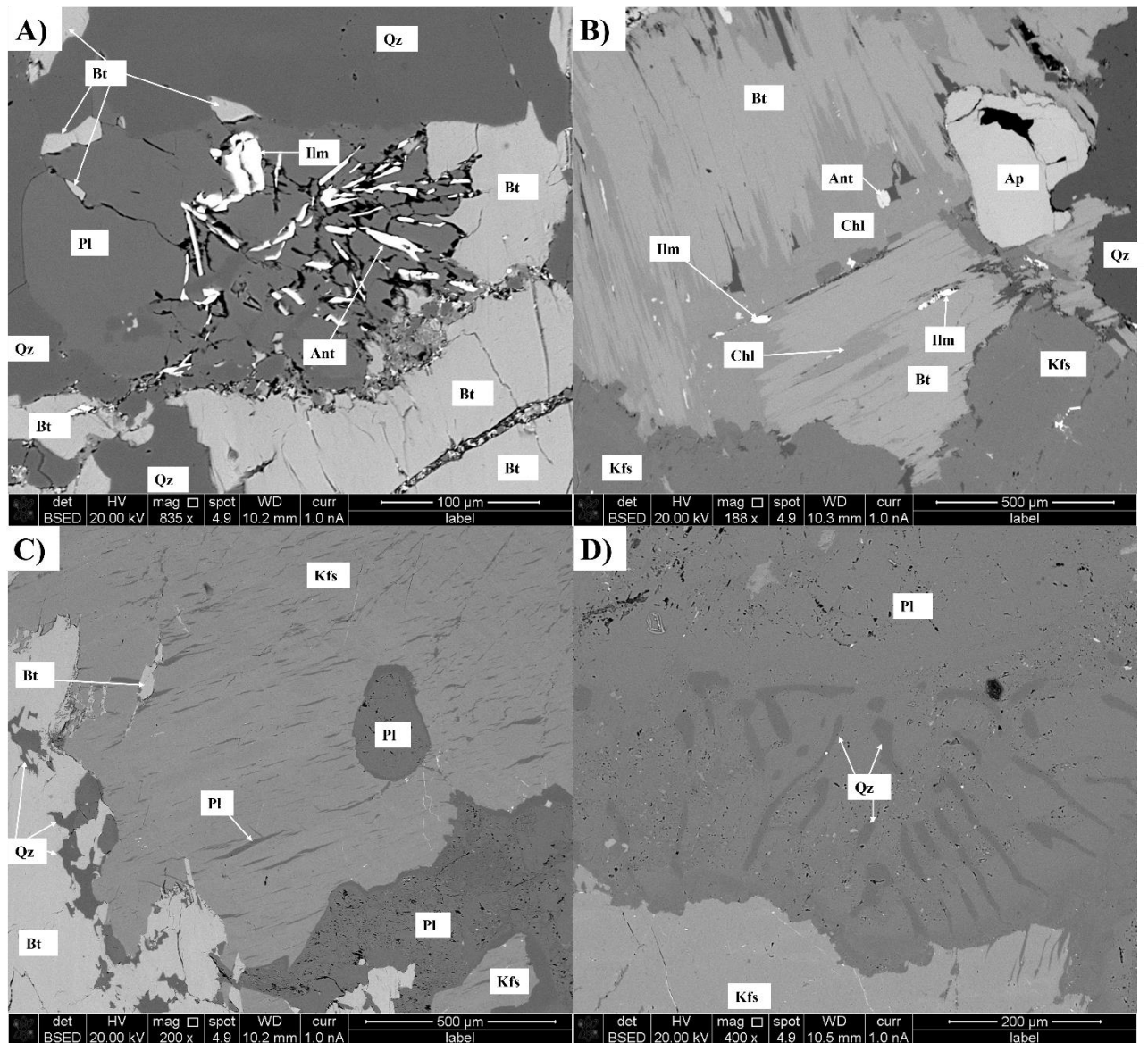


6 Figure. Representative SEM BSE images of the investigated thin section M7M – 353. A) – Tabular biotite surrounded by quartz, K-feldspar and plagioclase. In the plagioclase are forming K-feldspar antiperthites; B) – Plagioclase grain with vermicular quartz intergrowths. Plagioclase is surrounded by K-feldspar phenocryst; C) – Biotite being replaced by secondary calcite and pyrite. Biotite surrounded by plagioclase phenocryst; D) – Magnetite grain being replaced by lamella-like hematite. The abbreviations are explained in the abbreviation list.

ilmenite, and calcite. The calcite matrix hosts euhedral to subhedral pyrite grains approximately 0.01 mm in size (Fig. 6C). The larger iron oxide grains, measuring between 0.5 and 1 mm, in the BSE images display complex intergrowths of subhedral magnetite, with hematite forming lamella-like microstructures within the magnetite, suggesting the former replaces the latter (Fig. 6D). The apatites, sized between 0.03 and 0.04 mm, form subhedral grains with a patchy cathodoluminescence (CL) pattern and dark CL domains along the fractures and rims.

M7S – 372

M7S (depth 372 m) is a bright red, coarse-grained porphyritic granite. The major minerals include quartz (30%), K-feldspar (35%), plagioclase (27%), biotite (7%), and accessory minerals



7 Figure. Representative SEM BSE images of the investigated thin section M7S – 372. A) – Anhedral plagioclase grain with ilmenite and anatase intergrowth. Plagioclase is surrounded by quartz, biotite; B) – Subhedral biotite grain being replaced by secondary chlorite along rims and cleavage planes while minor ilmenite forms between the biotite sheets; C) – Phenocryst of K-feldspar with thin strips of plagioclase forming perthite; D) – Phenocryst of plagioclase with myrmekite forming in the rims. The abbreviations are explained in the abbreviation list.

(1%). The accessory minerals are titanite, anatase, ilmenite, pyrite, calcite and apatite. Secondary chlorite and calcite replace biotite grains along the rim and cleavages, with minor ilmenite forming between biotite sheets (Fig. 7B). The intergrowth of ilmenite and anatase can be seen in plagioclase (Fig. 7A). The matrix is composed of biotite, K-feldspar, plagioclase, quartz, secondary and accessory minerals while phenocrysts are plagioclase, K-feldspar, quartz.

Plagioclase forms subhedral grains measuring 1 to 5 mm. As in the previous samples, plagioclase exhibits albitionisation along its rims (Fig. 7C, D). Plagioclase grains at the interstices display a myrmekite texture (Fig. 7D). The K-feldspars are anhedral, ranging in size from 0.2 to 5 mm, and show a perthite texture. Inclusions within K-feldspar primarily consist of plagioclase, biotite, and quartz. The quartz is subhedral, with sizes ranging from 0.5 to 5 mm. The biotites are subhedral and anhedral, with sizes varying from 0.5 to 2 mm. Inclusions of plagioclase and K-feldspar are found within the biotite. There is a range of grey colour intensity in the biotite grains, some of which have transformed into chlorite or muscovite (Fig. 7B). Titanite and ilmenite are anhedral, with sizes between 0.05 and 0.1 mm. The apatite is anhedral, ~0.5 mm, and exhibits a patchy cathodoluminescence pattern. The pyrite is subhedral, with a size of 0.05 mm.

5.3 Mineral Chemistry

The obtained chemical composition of the main and accessory minerals is presented in Appendix 2A-L.

5.3.1 Major Minerals

Feldspars

The feldspar formula was calculated based on 8 oxygens (see Appendix 2A) and plotted in the classification diagram by Deer et al. (1963). In the feldspar ternary plot, the investigated thin section feldspar plots in the orthoclase, albite, and oligoclase fields (Fig. 8A, B), with the myrmekite texture plagioclase being more albitic in composition (Fig. 8B).

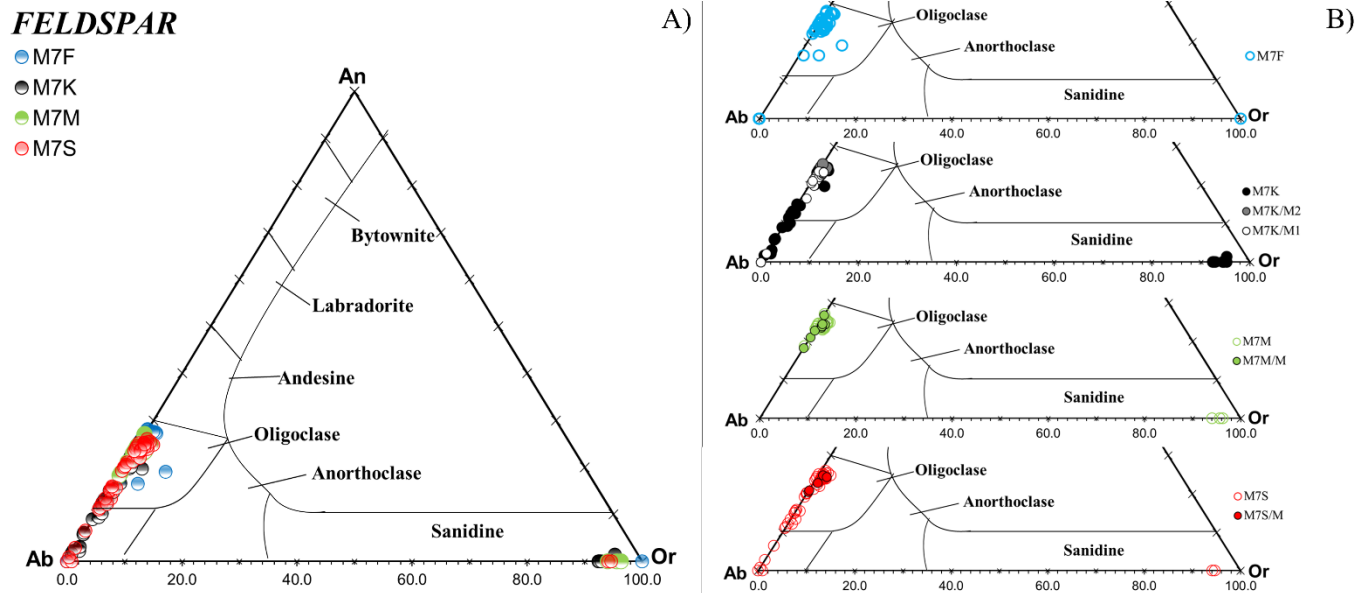
The calculated end-members in the investigated M7F plagioclases correspond to oligoclase (An_{16-28}) and albite (An_0) (Fig. 8B). The K-feldspars have Or_{100} content (Fig. 8B).

M7K investigated plagioclases plot in oligoclase (An_{11-25}) and albite (An_{1-10}) areas (Fig. 8B). The myrmekite-textured plagioclases plot in the oligoclase (An_{16-23}) to albite (An_{1-2}) fields (Fig. 8B). Myrmekite plagioclases in the mafic enclave part are oligoclase (An_{22-25}) (Fig. 8B). The K-feldspars have an average composition of $Or_{94}Ab_6An_{0.1}$.

The M7M thin section investigated plagioclase is the oligoclase (An_{18-27}) (Fig. 8B). The myrmekite-textured plagioclases are oligoclase (An_{18-26}). K-feldspars have an average composition of $Or_{95}Ab_5$.

The M7S thin section plagioclases plot in the oligoclase (An_{11-25}) and albite (An_{0-6}) fields (Fig. 8B). The myrmekite-textured plagioclases are oligoclase (An_{20-24}). The K-feldspars have an average composition of $Or_{94}Ab_6$.

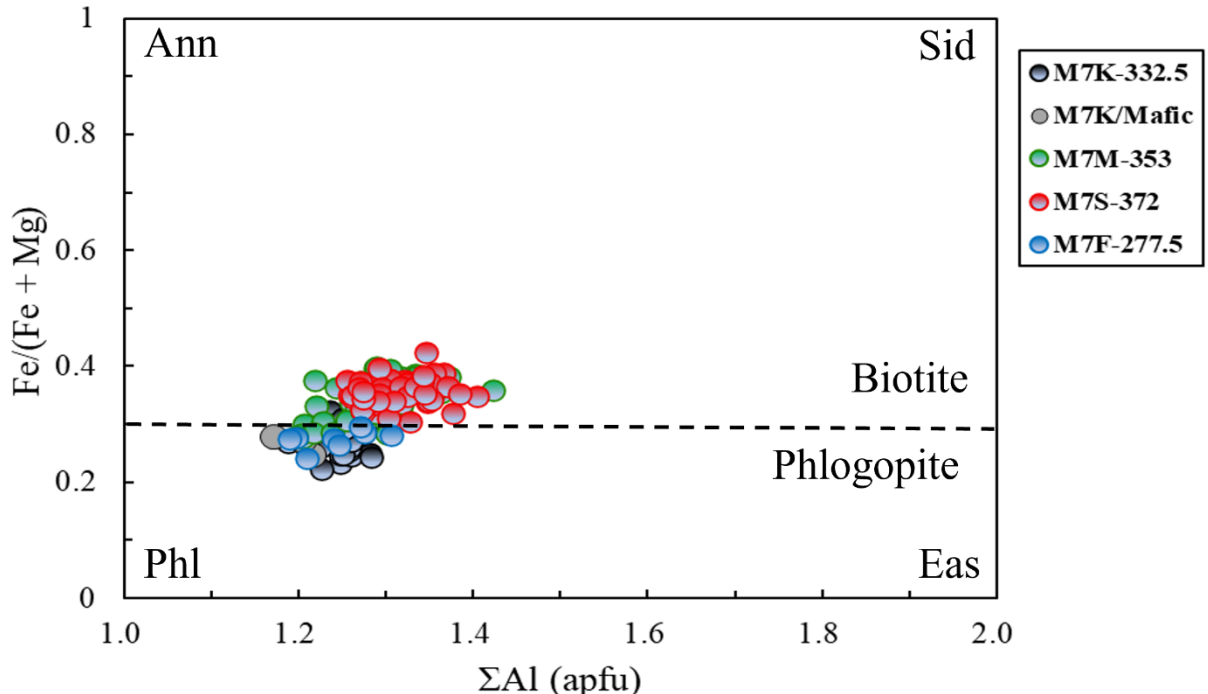
The ternary plot shows a gradual transition of albitized plagioclases in M7K and M7S (Fig. 8B), whereas a compositional gap is present in the M7F sample (Fig. 8B). The M7M plagioclases plot in the oligoclase field (Fig. 8B).



8 Figure. The ternary Ab-An-Or feldspar classification diagram by Deer et al. (1963). A) – all investigated plagioclases; B) – separated plagioclases from different thin sections. The legend is the same as in A). The M7K/M1 – myrmekite texture in plagioclase; M7K/M2 – myrmekite texture plagioclases in the mafic enclave part. M7M/M – myrmekite texture plagioclases; M7S/M – myrmekite texture plagioclases.

Biotites

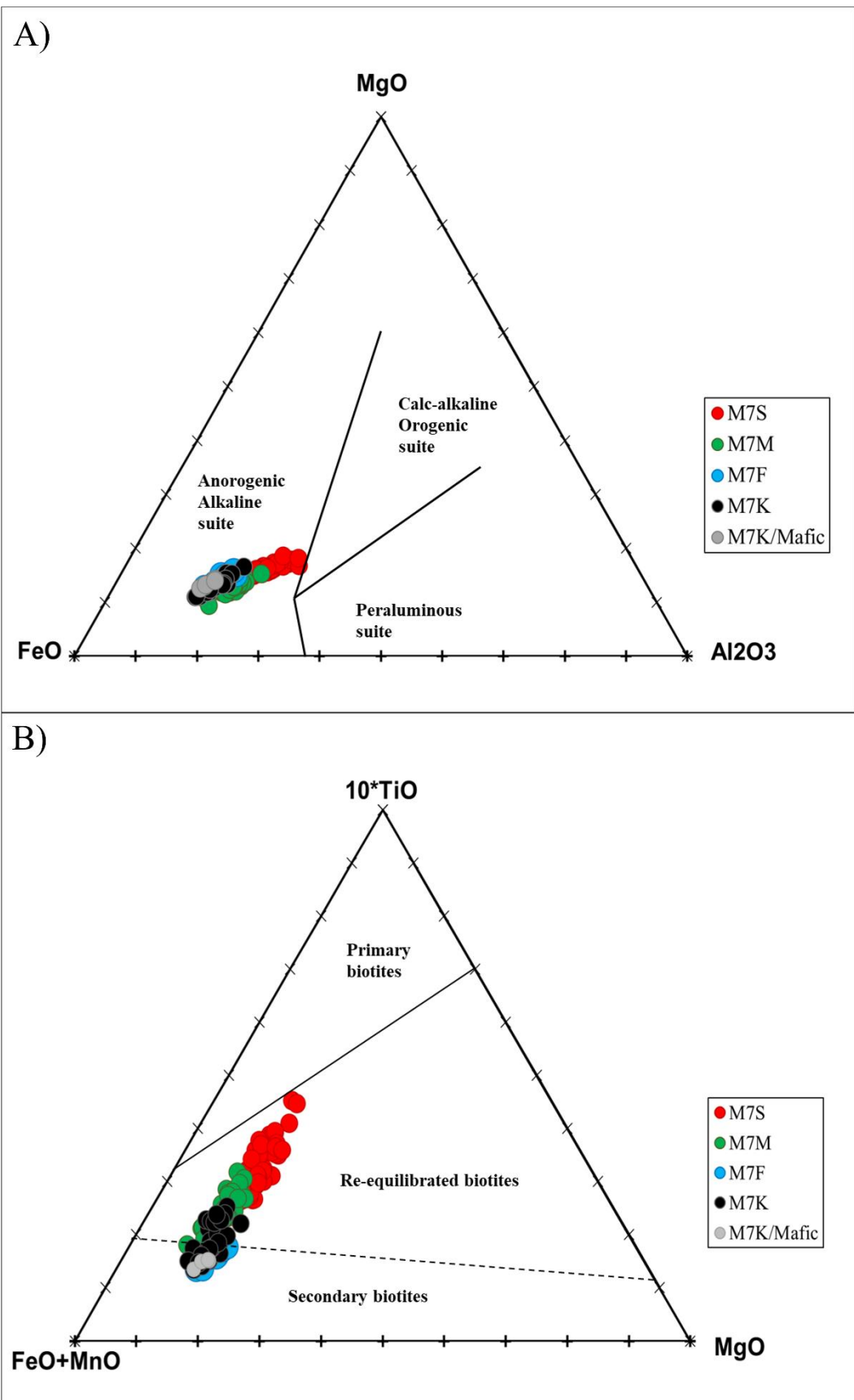
The biotite formula was calculated based on 11 oxygen atoms per formula unit, using the Excel sheet by Li et al. (2020), which allows estimation of Fe^{3+} in biotite (See Appendix 2B).



9 Figure. Biotite classification for the investigated M7 biotites (after Rieder et al., 1998).

In the biotite classification diagram by Rieder et al. (1998), biotites straddle between phlogopite and biotite (annite side) boundary (Fig. 9). Most of the M7K (including mafic part) and M7F biotites are slightly richer in Mg and classified as phlogopite, while the more Fe-rich M7S and M7M biotites are plot in the annite side. The #Fe average ratio of M7F is 0.27 (from 0.24 to 0.30), M7K is 0.27 (0.22 – 0.36), M7M is 0.34 (0.28 – 0.4), and M7S is 0.36 (0.31 – 0.43). The M7K mafic part is 0.26 (0.24 – 0.30). The average of amount F (apfu) in biotites is 0.44 (range from 0.0 to 0.58) in sample M7F, 0.45 (0.0-0.62) in M7K and 0.54 (0.51–0.57) in mafic part, 0.39 (0.0-0.58) in M7M, and 0.47 (0.37-0.57) in M7S. The average amount of Cl (apfu) is 0.06 in M7F (range from 0.04 to 0.06), 0.07 in M7K (0.04-0.1) and 0.06 in mafic part (0.06-0.07), 0.06 in M7M (0.04-0.08), and M7S is 0.05 (0.03-0.06).

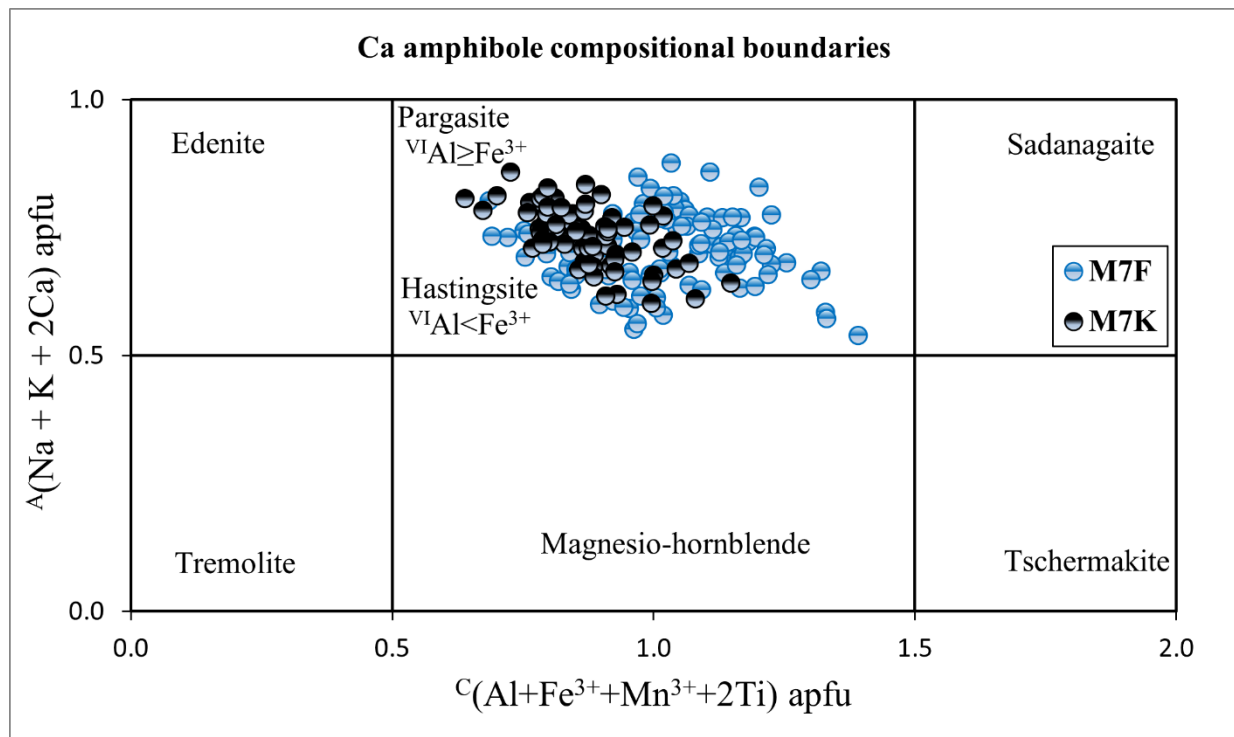
In the ternary diagram by Abdel-Rahman (1994) $\text{FeO}-\text{MgO}-\text{Al}_2\text{O}_3$, biotites fall in the anorogenic alkaline suite field (Fig. 10A). In the $10^*\text{TiO}_2-(\text{FeO}+\text{MnO})-\text{MgO}$ ternary diagram by Nachit et al. (2005), the investigated biotites form a trend just below the primary biotite field, with the most biotites falling into the re-equilibrated and secondary biotite fields (Fig. 10B). Most of the biotites from samples M7F, M7K and M7K mafic part fall in the secondary biotite field (Fig. 10B).



10 Figure. Biotite ternary discrimination diagrams for the investigated M7 biotites: A) FeO-MgO-Al₂O₃ (wt.%) (after Abdel-Rahman, 1994); B) 10^{*}TiO₂-(FeO+MnO)-MgO (wt.%) (after Nachit et al., 2005).

Amphiboles

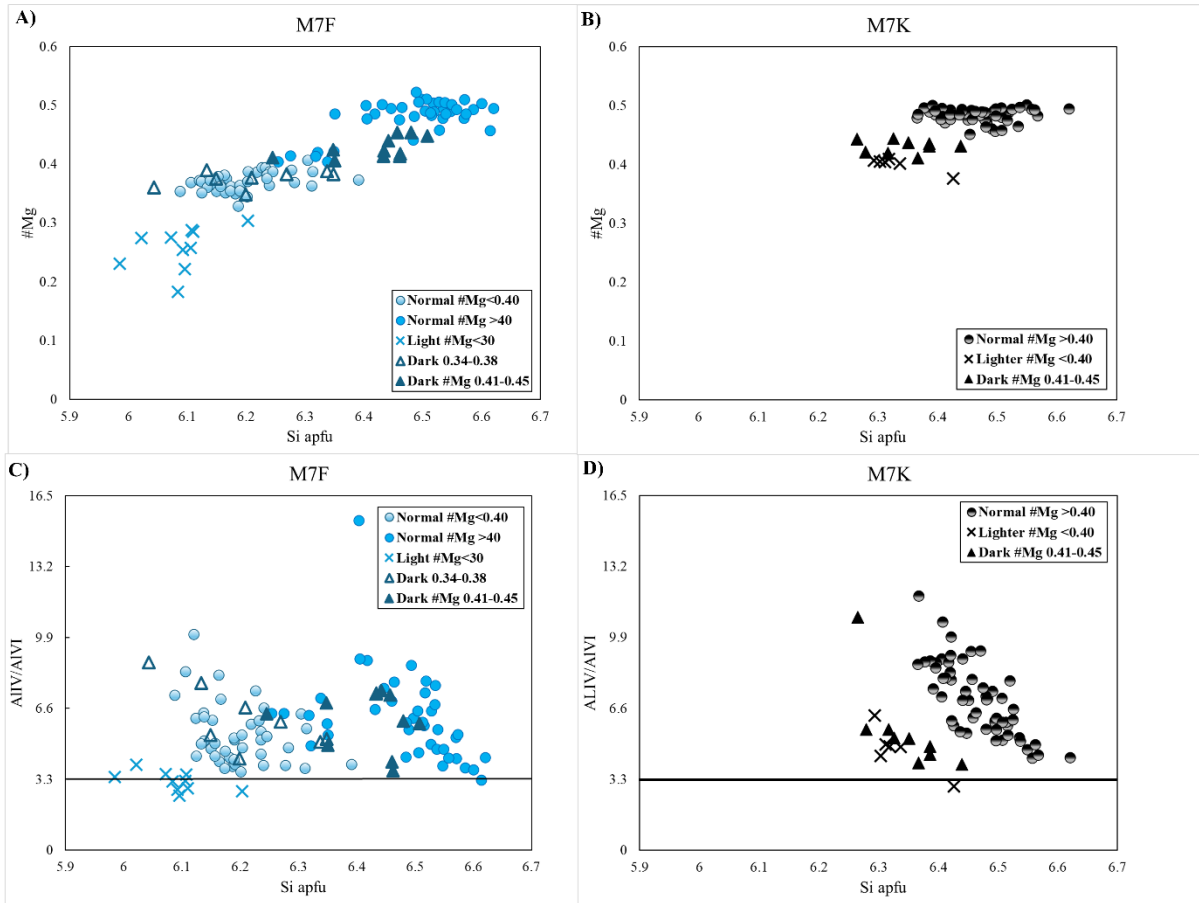
The amphibole formulas were calculated based on 23 oxygen atoms per formula unit (see Appendix 2C) and classified according to Hawthorne et al. (2012; Fig. 11). The investigated amphiboles were identified as pargasitic calcic amphiboles due to their high Ca content in the M4 site. The $V^{VI}Al/Fe^{3+}$ ratio further classifies the calcic amphiboles into ferro-pargasite, potassic-ferro-pargasite, and pargasite ($V^{VI}Al \geq Fe^{3+}$), as well as hastingsite, magnesio-hastingsite, and potassio-hastingsite ($V^{VI}Al < Fe^{3+}$; Appendix 2C). The $Fe^{3+}/V^{VI}Al$ ratio is a key criterion for differentiating pargasite from hastingsite. Most of the analysed amphiboles show values near the classification boundary (Fig. 11).



11 Figure. Amphibole compositions in the M7F and M7K samples are presented in a nomenclature diagram for calcic amphiboles, plotting $A(Na + K + 2Ca)$ apfu vs $C(Al + Fe^{3+} + Mn^{3+} + 2Ti)$ apfu (Hawthorne et al., 2012).

The amphiboles in M7F and M7K can be distinguished based on their #Mg values and variations in colour intensity (light, dark, or homogeneous/normal zones). The M7F amphiboles are classified into five groups: normal $\#Mg < 0.40$, normal $\#Mg > 0.40$, dark $\#Mg$ in a range of 0.34–0.38, dark $\#Mg$ range of 0.41–0.45 and light $\#Mg < 0.30$ (Fig. 12A). The M7K amphiboles are sorted into three groups: normal with $\#Mg > 0.40$, dark $\#Mg$ in a range of 0.41–0.45 and light $\#Mg < 0.40$ (Fig. 12B). For further investigation, amphiboles are grouped based on #Mg values.

Using a ratio of Al^{IV}/Al^{VI} above 3.3 (Fleet and Barnett, 1978) and Si (apfu) values not exceeding 7.50 apfu (by Leake, 1971), amphiboles can be classified as primary igneous (Fig. 12C-D). The M7F amphiboles with Mg # < 0.30 have Al^{IV}/Al^{VI} ratio values below the boundary, and some of the M7K amphiboles (#Mg > 0.40 and light #Mg < 0.40) are closely straddling the margin. (Fig. 12C-D).



12 Figure. M7 amphiboles binary diagrams: A)-B) Si (apfu) vs #Mg (Mg/(Mg+Fe)); C)-D) Si (apfu) vs Al^{IV}/Al^{VI}. A) and C) plotted M7F investigated amphiboles; B) and D) plotted M7K amphiboles.

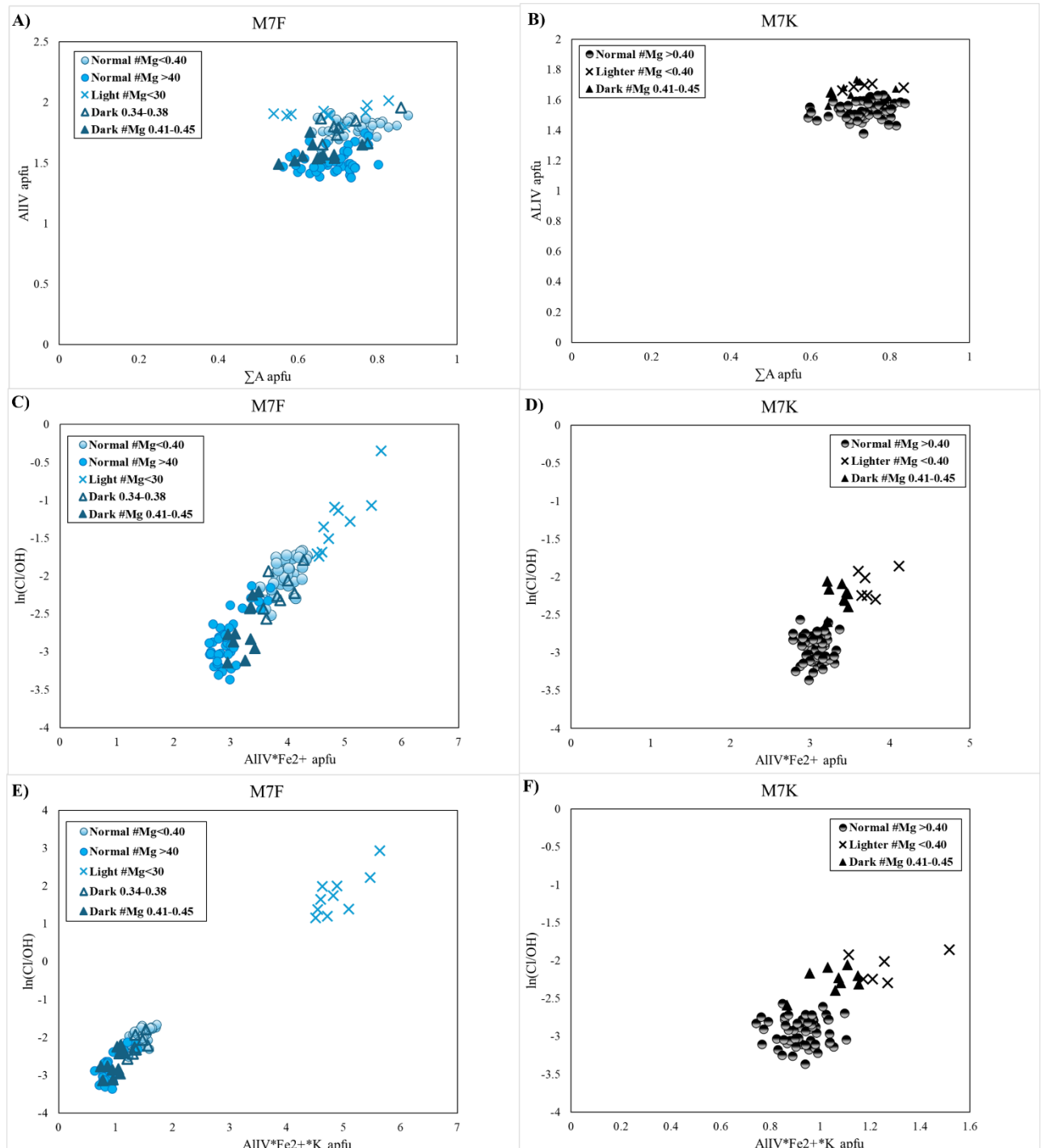
The positive correlation between $\sum A$ (apfu) and ^{IV}Al influences Cl incorporation, as described by Ito and Anderson (1983), Vanko (1986), Suwa et al. (1987), Morrison (1991), and Enami et al. (1992). The substitution of K in the A-site enhances Cl incorporation (Suwa et al., 1987; Morrison, 1991), whereas Fe²⁺ in the octahedral sites has a minimal influence on Cl content (Vanko, 1986).

The positive correlation between $\sum A$ (apfu) and ^{IV}Al (Fig. 13 A-B) reflects the Si-Al exchange in tetrahedral sites, where higher ^{IV}Al values are associated with increased A-site occupancy by K and Na. Additionally, the $^{IV}Al \times Fe^{2+}$ (apfu) vs. ln(Cl/OH) and $^{IV}Al \times Fe^{2+} \times K$ (apfu) vs. ln(Cl/OH) plots show a strong positive linear correlation (Fig. 13C-F).

In Fig. 13C, the M7F amphiboles form a trendline with a slight overlap of the distinct groups, whereas in Fig. 13D, the M7K amphiboles form two distinct clusters: lighter #Mg < 0.40 and dark #Mg 0.41–0.45 form one group and the normal #Mg > 0.40 form another group. By incorporating K substitution as an additional variable, the M7F amphiboles separate into two distinct groups: light #Mg < 30 forms one cluster and the rest of the amphiboles form another (Fig. 13E). Similarly, in Fig. 13F, the compositional gap in the M7K amphibole groups widens, compared to that observed in $^{IV}Al \times Fe^{2+}$ (apfu) vs. ln(Cl/OH) (Fig. 13D). This illustrates that K substitution in the A-site strongly influences Cl incorporation, while Fe²⁺ has a much smaller effect.

Overall, the amphiboles investigated in both M7F and M7K are mostly hastingsite with a few grains of ferro-pargasite, magnesio-hastingsite, potassio-hastingsite, potassio-ferro-pargasite, and

pargasite. Amphibole in both thin sections shows the ratio of $Mg/(Mg+Fe^{2+})$ of 0.18–0.52 (average 0.43), varying Al (total) amount of 1.67 – 2.66 apfu (average 1.94), and low Ti concentrations in the range of 0 – 0.2 apfu (average 0.08). The average Cl content is 0.2 apfu (from 0.067 to 0.83 apfu) and fluorine is below the detection limit. Amphiboles with Si values not exceeding 7.50 apfu (Leake, 1971) and an Al^{IV}/Al^{VI} ratio above 3.3 (Fleet and Barnett, 1978) are classified as primary igneous amphiboles. In the M7F samples, light #Mg < 30 amphiboles plot below this boundary, while in the M7K samples, some #Mg > 0.40 and light #Mg < 0.40 amphiboles are positioned close to the boundary (Fig. 12C-D).



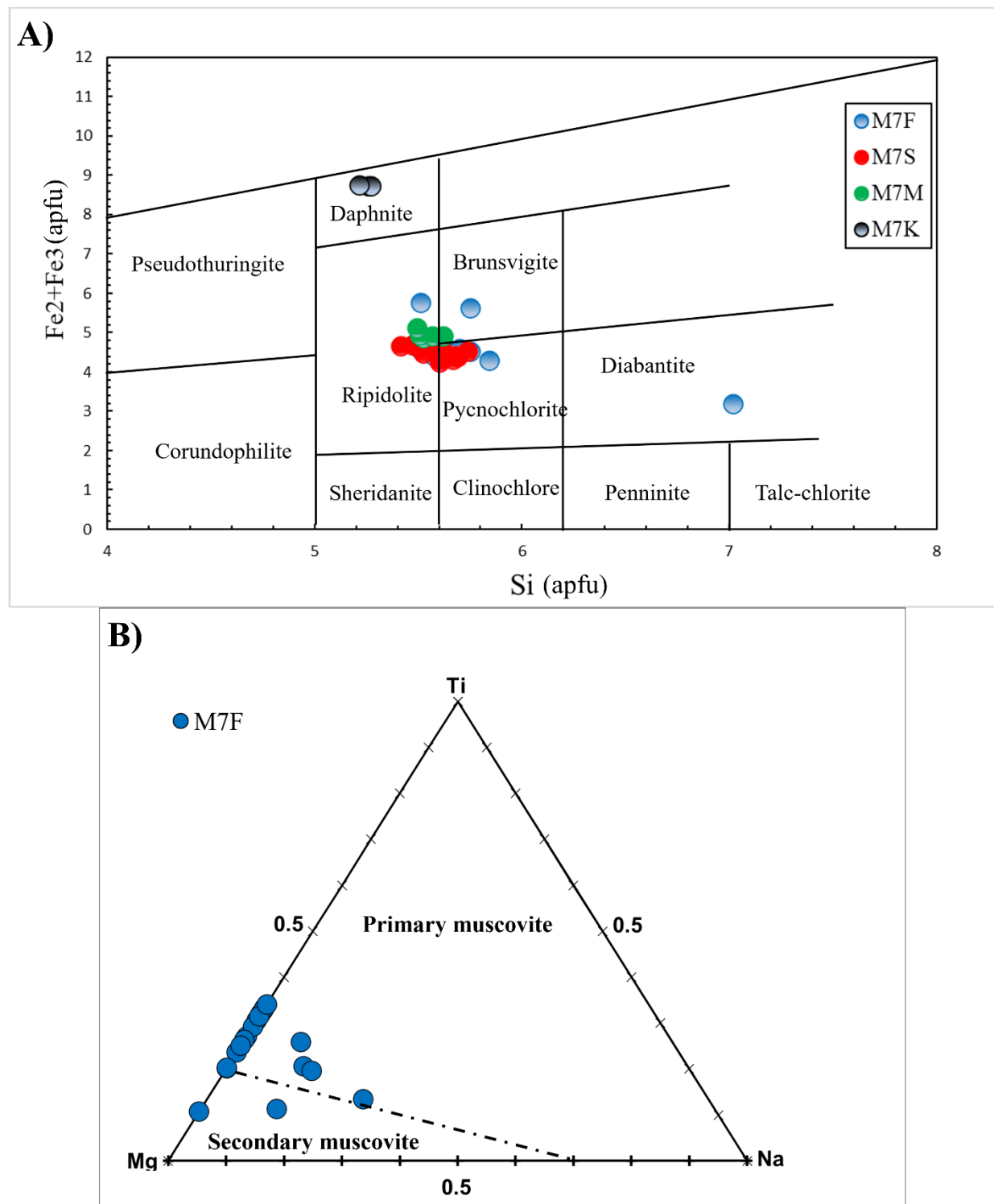
13 Figure. Compositional plots of M7 amphibole: A)-B) ΣA vs. Al^{IV} ; C)-D) $Al^{IV} \times Fe^{2+}$ (apfu) vs. $ln(Cl/OH)$; E)-F) $Al^{IV} \times Fe^{2+} \times K$ (apfu) vs. $ln(Cl/OH)$ (Sato et al., 1997). A), C) and E) plotted M7F investigated amphiboles; B), D) and F) plotted M7K amphiboles.

5.3.2 Secondary minerals

Chlorite

The chlorites were calculated based on 36 oxygens (see Appendix 2D) and classified according to Hey (1954) (Fig. 14A). The chlorites fall within the boundaries of ripidolite, pycnochlorite and brunsvigite (Fig. 14A), with one sample from M7F plotting in the diabantite field (Fig. 14A). The M7K chlorites are classified as daphnites (Fig. 14A).

Compositionally, the chlorites from M7 exhibit a wide range of FeO (16.5 – 43.6 wt.%), Al₂O₃ (12.22 – 22.0 wt.%), MgO (0 – 21.2 wt.%) and Fe₂O₃ (0.2 – 3.6 wt.%) contents. More frequently chlorites are enriched in MnO (0.27 – 3.46 wt.%) and only three analyses showing enrichment in TiO₂ (0.25 - 3.8 wt.%). The #Fe ratios range from 0.31 to 1 and are higher than those in the biotites.



14 Figure. A) Classification diagram for the investigated M7 chlorites (apfu) (after Hey, 1954); B) Ternary Mg–Ti–Na (apfu) diagram for the M7S investigated muscovite, discriminating between primary and secondary muscovite (after Miller et al., 1981; Tartèse and Boulvais, 2011)

Muscovite

The muscovite was only found in the M7S thin section. It was calculated based on the 11 oxygen (see Appendix 2E) and classified according to Miller et al. (1981) and Tartèse and Boulvais (2011) (Fig. 14B). The muscovite plots in the primary muscovite area, with only a few points straddling the

boundary to the secondary area (Fig. 14B). It has a high TiO_2 content, ranging from 0.42 to 1.7 wt.%, with TiO_2 in secondary muscovite being in a range of 0.42–0.47 wt.%. Some analyses show minor content of Na_2O (0.22 – 0.63 wt.%) and CaO (0.26 - 0.41 wt.%). The average #Fe number is 0.57 (ranging from 0.54 to 0.6).

5.3.3 Accessory minerals

Carbonates

The carbonates were calculated based on 6 oxygens (see Appendix 2F). Two different carbonates were identified: siderite and calcite. Siderite is abundant in the M7F thin section with an average composition of 3.15 wt.% CaO , 2.2 wt.% MgO , 1.3 wt.% MnO and 52.2 wt.% FeO . Calcite was found in all thin sections, with only a few analyses showing notable amounts of Fe (0.57 and 0.75 wt.%) and Mn (0.52 and 1.27 wt.%).

Epidote

Epidote was found in the M7F thin section and calculated based on 25 oxygen atoms per formula unit (see Appendix 2G). It contains an average of 37.5 wt.% SiO_2 , 24 wt.% Al_2O_3 , 12 wt.% Fe_2O_3 and 23 wt.% CaO . Some grains contain trace amounts of Mn, ranging from 0.34 to 0.47 wt.%.

Ilmenite and hematite

The ilmenite and hematite were calculated based on 6 oxygens per formula unit (see Appendix 2H, I).

Ilmenite is abundant in all thin sections. It contains an average of 48 wt.% TiO_2 , 32 wt.% FeO , 11 wt% MnO and 5 wt.% Fe_2O_3 . A few analyses showed trace amounts of 0.34 – 5.05 wt.% SiO_2 , 2.34 wt.% Al_2O_3 , 2.64 wt.% MgO , and 0.19 – 0.44 wt.% CaO .

The hematite was investigated in sample M7M. In the analysis of the hematite, the FeO recalculated to Fe_2O_3 range between 98 and 99 wt.%. The minor elements show low concentrations of Cr_2O_3 (0.06–0.09 wt.%), V_2O_3 (0.16–0.25 wt.%), and Al_2O_3 (0.08–0.17 wt.%). The TiO_2 content is below the detection limit of the microprobe, with an average detection limit of 0.11 wt.%. Magnesium was detected more frequently, ranging from 0.006 to 0.06 wt.%. Mn and Zn were only detected in one spot (0.014 wt.% and 0.26 wt.%, respectively). SiO_2 was detected at one point with 0.02 wt.%, while CaO remained below the detection limit of the microprobe (average detection limit 0.026 wt.%).

Sulfides

The sulfides were investigated in the M7F, M7M and M7S thin sections. Their composition was calculated based on 13 sulfur atoms per formula unit (see Appendix 2J). Two types of sulfides were identified: sphalerite and pyrite. Sphalerite was found in the M7F thin section, containing 56 wt.% Zn and 31 wt.% S. Pyrite was more abundant, with an average composition of 47 wt.% Fe and 51 wt.% S.

Apatite

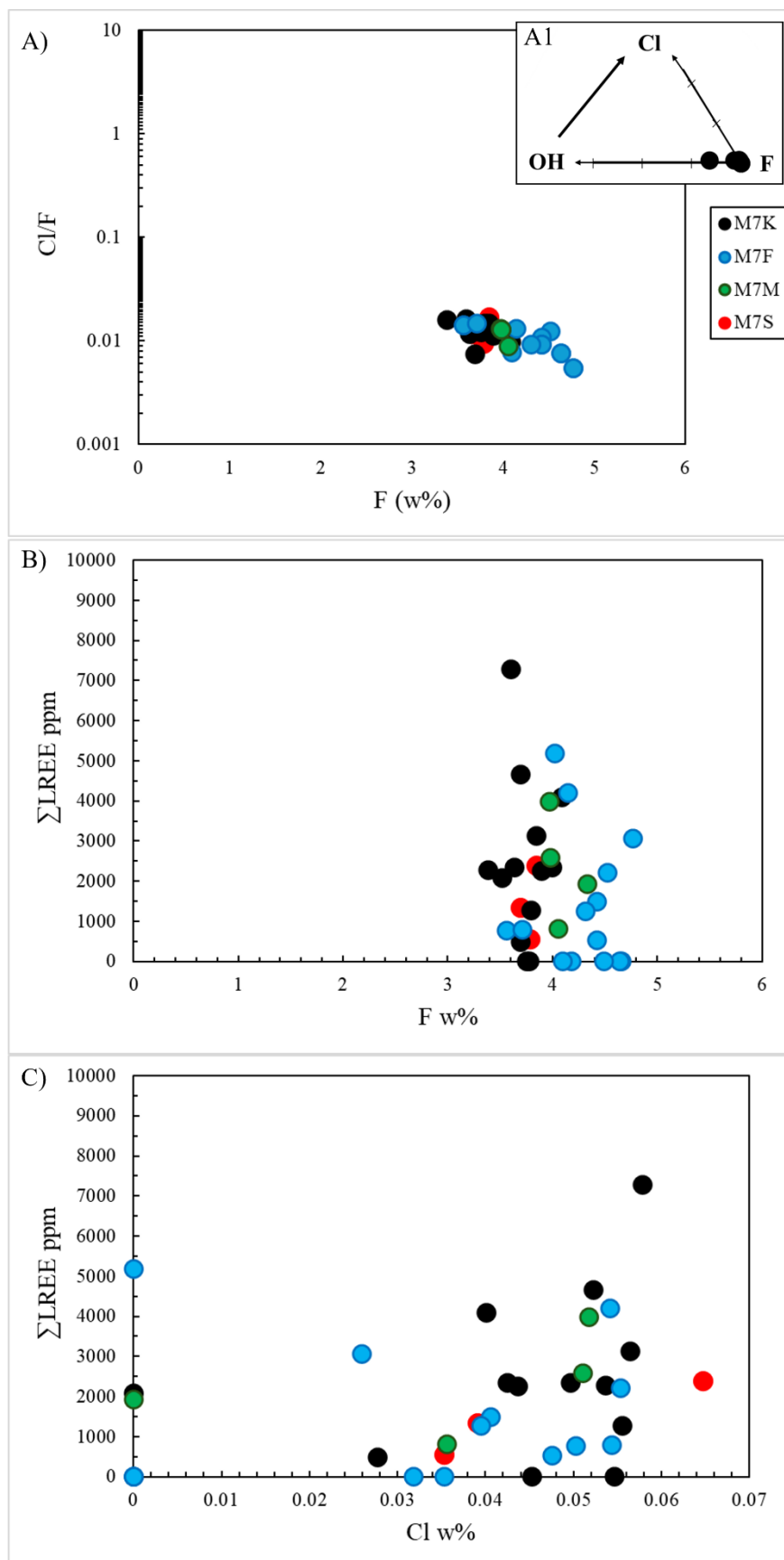
The apatites were investigated in all thin sections (see Appendix 2K). Their composition was recalculated based on 13 oxygens per formula unit (see Appendix 2K). There is very little variation

in the major apatite components, CaO and P₂O₅, with average values ranging between 50–55 wt.% and 40–43 wt.%, respectively. Some analyses detected traces of SiO₂, Na₂O, and FeO, with values varying between 0.05–0.5 wt.%, 0.05–0.12 wt.%, and 0.1–0.4 wt.%, respectively. Most apatites had Mn below the detection limit (average detected value 0.04 wt.%), with only a few samples showing higher values. Magnesium concentrations were below the detection limit of the microprobe with an average detection limit of 0.017 wt.%, and Al was not detected (detection limit 0.023 wt.%). All analysed apatites in this study are fluorapatites (Fig. 15A1), with F contents averaging between 3.4–4.8 wt.%.

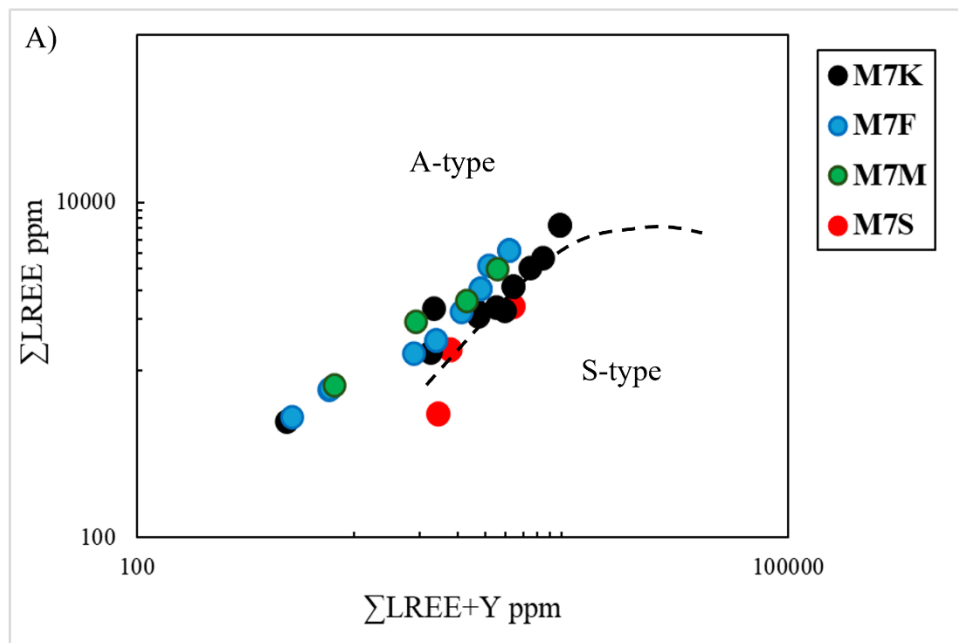
Three trace elements and five rare earth elements (REEs) were measured in this study. Most analysed elements were below the detection limit and were, therefore, excluded from the REE assessment. Arsenic was not detected (detection limit 479 ppm). Yttrium and strontium had low detection limits, with several analyses showing higher values: Y ranging from 597 to 2998 ppm and Sr from 490 to 2258 ppm. Light rare earth elements (LREEs) also had low detection limits, though some exhibited elevated concentrations of La (289–1715 ppm), Ce (492–3368 ppm), Pr (87–506 ppm), and Nd (551–2182 ppm). Samarium was below the detection limit in all analyses, with an average detection limit of 1077 ppm.

In the binary diagram (Fig. 15A), Cl/F vs. F, the apatites form a well-defined group without significant scattering, indicating fluorine-rich conditions. In Fig. 15B (Σ LREE ppm vs. F wt.%), F shows very poor correlation with the LREE concentrations. Conversely, in Fig. 15C (Σ LREE ppm vs. Cl wt.%), a positive correlation is apparent, where higher Cl values are associated with increased LREE concentrations.

The discrimination diagram proposed by Kiefer et al. (2024) distinguishes apatite from A- and S-types. The investigated apatite in this study plots in the A-type and only a few straddling the boundary to S-type (M7S and M7K) (Fig. 16).



15 Figure. Binary diagrams comparing volatile contents: A) Cl/F vs. F (w%) and in the corner A1 - F-Cl-OH diagram showing that the apatite measured by EPMA in this study falls within the fluorapatite field (atoms per formula unit).; B) ΣLREE (ppm) vs. F (w%); C) ΣLREE (ppm) vs. Cl (w%).



16 Figure. Discrimination diagram distinguishing the investigated apatite from S- and A-type granites, based on Σ LREE vs. Σ REE + Y in apatite (after Kieffer et al., 2024).

Magnetite

The magnetite was investigated in the samples M7M (see Appendix 2L). The formula for magnetite was calculated based on 32 oxygen atoms per formula unit (see Appendix 2L).

In the examined magnetite grains, there is little variation in the major mineral components, FeO and Fe_2O_3 , with the calculated values ranging between 30–31 wt.% and 68–69 wt.%, respectively. The minor elements exhibited low concentrations, most remaining below the detection limit. The magnetite is poor in Cr_2O_3 (0.08–0.09 wt.%), V_2O_3 (0.15–0.3 wt.%), Al_2O_3 (0.07–0.1 wt.%), and TiO_2 , with the latter detected at only one individual point with 0.6 wt.%. Mg and Mn concentrations were below the detection limit of the microprobe, with average detection limits of 0.03 wt.% and 0.1 wt.%, respectively, and Zn was not detected (average detection limit 0.2 wt.%). SiO_2 was identified at two points with 0.02 wt.% and 0.09 wt.%, while CaO was detected at one point with 0.02 wt.% (average detection limits are 0.03 and 0.03 wt.%, respectively).

5.4 Physicochemical conditions

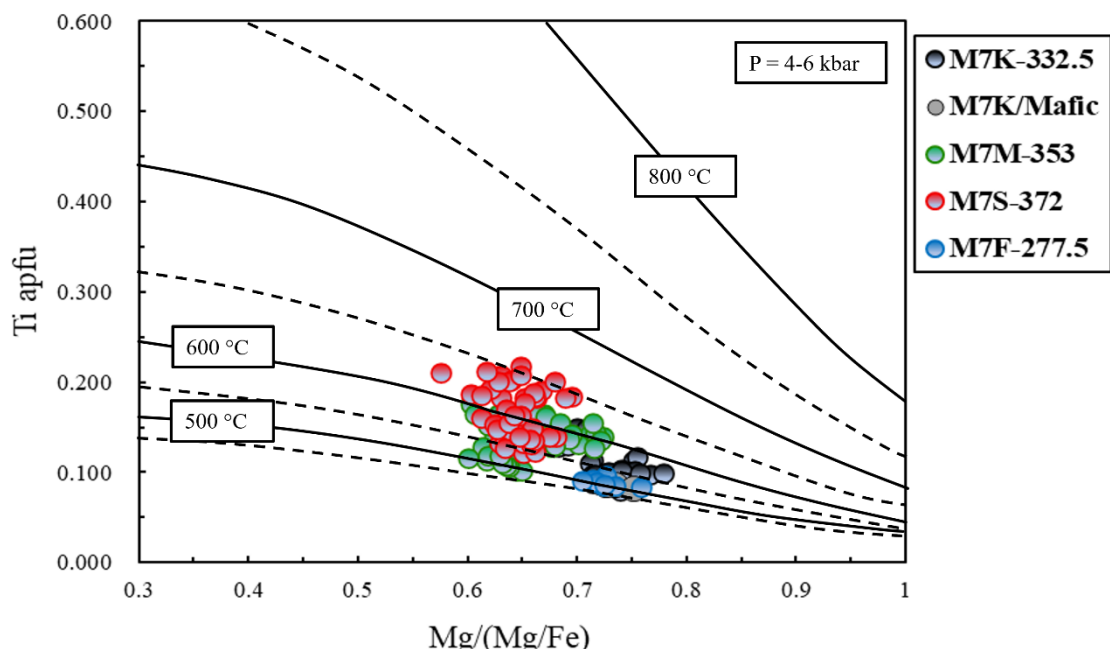
5.4.1 Temperature and Pressure

Ti in Biotite Thermometry

In order to obtain the Ti-in biotite temperature estimates (Henry et al., 2005), biotite Mg# was calculated in the studied samples (Appendix 2B). The #Mg values in sample M7F ranges from 0.70 to 0.76 (average 0.73), M7S from 0.58 to 0.69 (average 0.64), M7K from 0.64 to 0.78 (average 0.72) and M7K mafic part from 0.72 to 0.75 (average 0.73), and M7M from 0.60 to 0.72 (average 0.66) (Fig. 17). Results for Ti-in-biotite thermometry (see Appendix 2B) are in the range of 483–651 °C (average 567 °C; Fig. 17). Figure 17 shows two distinct groups of biotite temperatures: one comprising M7F and M7K, and the other including M7M and M7S. Secondary biotites (M7F, M7K;

Fig. 10B) exhibit lower temperatures, ranging from 483 to 608 °C (average 525 °C). The mafic enclave part in M7K calculated temperatures range from 495 to 502 °C (average 498°C). In contrast, re-equilibrated biotites (M7M, M7S) show higher temperatures, ranging from 485 to 651 °C (average 579 °C) (Fig. 17).

The pressure (P) calculated using Equation 2 from Uchida et al. (2007) for biotite ranges from 57 to 209 MPa, with an average of 123 MPa (see Appendix 2B). Secondary biotites exhibit lower pressures, ranging from 57 to 138 MPa (average 97 MPa), including and mafic enclave part (range from 57 to 84 MPa, average 74 MPa). In contrast, re-equilibrated biotites show higher pressure values, ranging from 66 to 209 MPa (average 130 MPa).



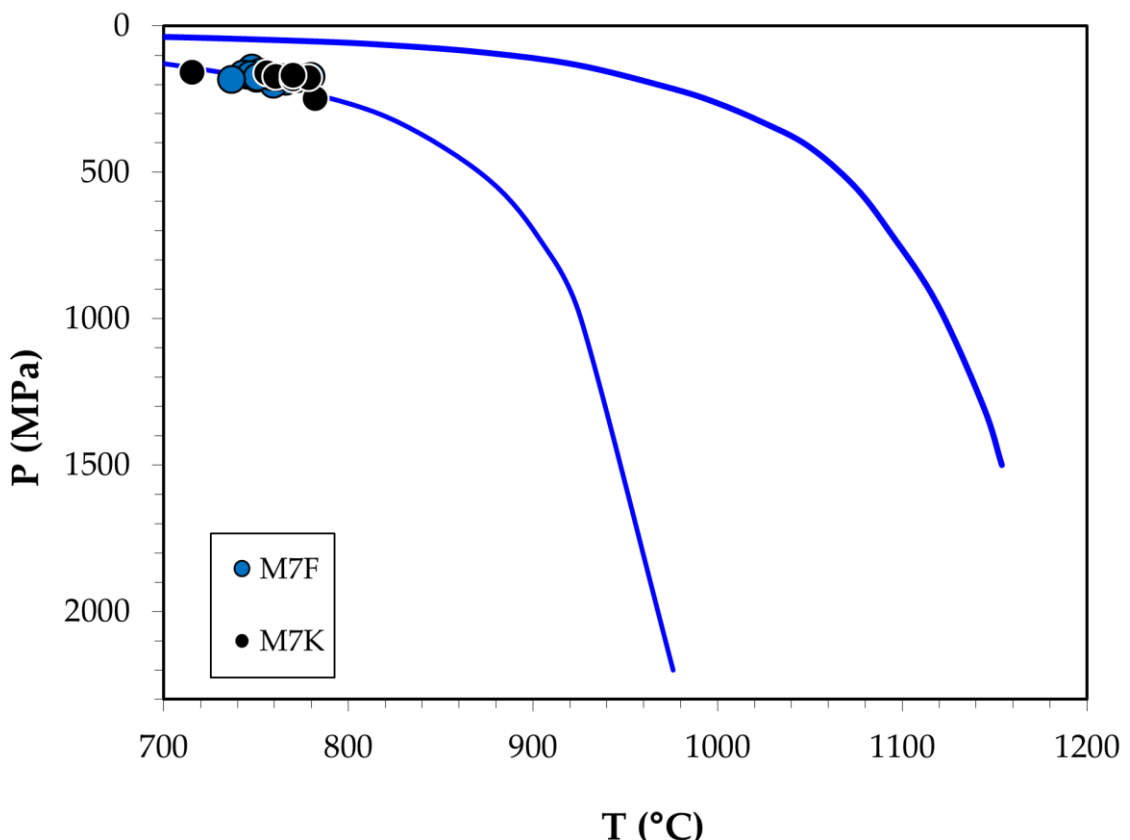
17 Figure. Temperature isotherms (°C) calculated from the surface-fit equation on a Ti vs. Mg/(Mg + Fe) diagram for the investigated biotites. Dashed curves represent intermediate 50°C interval isotherms (after Henry et al., 2005).

Amphibole thermobarometer

The results for the amphibole thermometry (Ridolfi, 2021) yielded values ranging from 712 to 824 °C (average 763 °C) (see Appendix 2C). The M7F amphiboles calculated average temperatures are: 767 °C in the group normal #Mg<0.40, 759 °C normal #Mg>0.40, 755 °C dark #Mg 0.34-0.38, 755 °C dark #Mg 0.41-0.45 and 755 °C light #Mg<0.30 (see Appendix 2C). The M7K amphiboles calculated average temperatures are: 767 °C in the group normal #Mg>0.40, 756 °C dark #Mg 0.41-0.45 and 774 °C light #Mg<0.40 (see Appendix 2C).

The amphiboles that fit the calibration by Ridolfi (2021) are illustrated in Fig 18. The lighter and darker domains found in the amphiboles are outside the calibration of Ridolfi (2021) and were not used in temperature estimations. The amphiboles that fit the conditions are homogeneous with #Mg>0.40, and temperatures vary between 716 and 782°C (average 759°C) (Fig. 18). The M7F amphiboles range from 737 to 780 °C (average 757 °C), and in the M7K, the range is from 716 to 782 °C (average 764 °C) (Fig. 18).

The calculated pressures for the crystallisation of the amphiboles range from 145 to 530 MPa (average 228 MPa) (see Appendix 2C). The M7F amphiboles calculated average pressures are: 291 MPa in the group normal #Mg<0.40, 182 MPa normal #Mg>0.40, 195 MPa dark #Mg 0.34-0.38, 248 MPa dark #Mg 0.41-0.45 and 467 MPa light #Mg<0.30. The M7K amphiboles calculated average pressure are: 185 MPa in the group normal #Mg>0.40, 195 MPa dark #Mg 0.41-0.45 and 186 MPa light #Mg<0.40 (see Appendix 2C). The amphiboles that fit the calibration by Ridolfi (2021) are homogeneous with #Mg>0.40. The calculated pressure values there range from 145 to 249 MPa (average 176 MPa) (Fig. 18). In the M7F amphiboles, the range is from 145 to 199 MPa (average 174 MPa), while the M7K ranges from 159 to 249 MPa (average 181 MPa) (Fig. 18).



18 Figure. P (MPa) vs. T (°C) diagram for the investigated amphiboles in the M7F and M7K thin sections. The selected points are certain. The blue line, drawn from experimental amphiboles, indicates the certainty of the P and T values (Ridolfi, 2021)

The Zircon saturation temperature

The calculated zircon saturation temperature based on Watson and Harrison (1983) ranges from 830.1-895.6 °C (average 870 °C) (see Appendix 1). According to Boehnke et al. (2013), the temperature ranges from 803-876 °C (average 847 °C) (see Appendix 1). Both estimates produced similar results and represent the melt crystallisation temperatures.

The Apatite saturation temperature

The calculated apatite saturation temperature was determined using equations (6) and (7) based on Harrison and Watson (1984). It ranges from 851-990.2 °C (average 922.1 °C). The lowest temperature (773.3 °C) was calculated in sample M7/293.351 (see Appendix 1).

The Apatite-biotite geothermometer

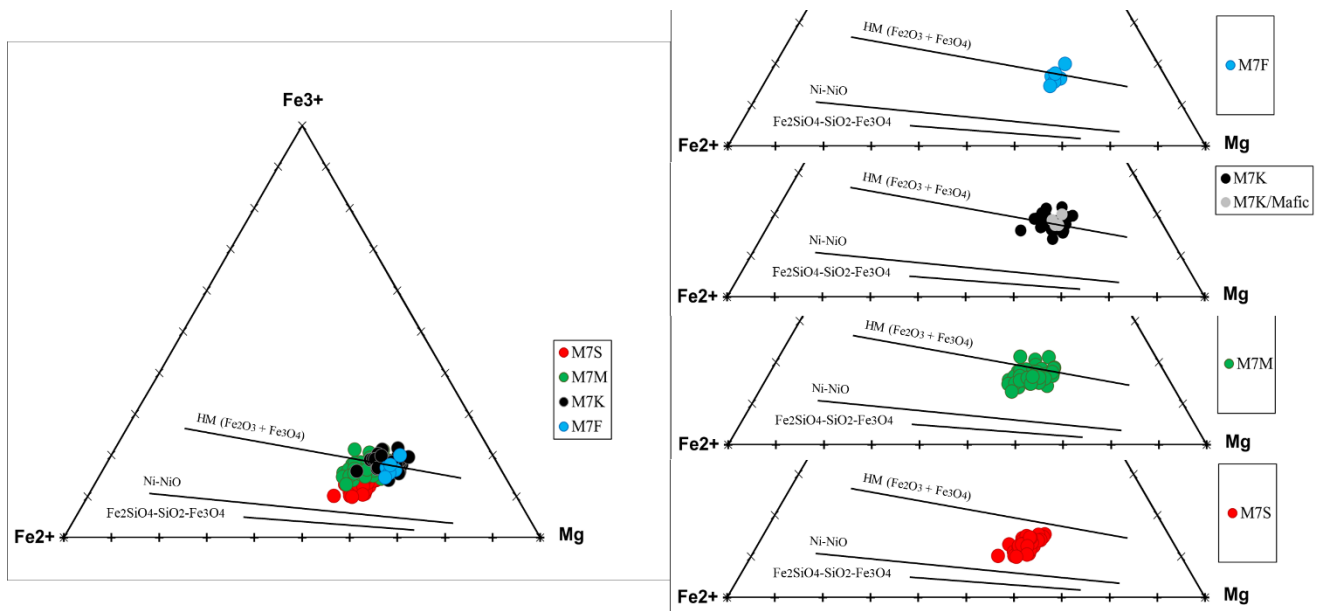
The Apatite-biotite geothermometer was determined using equation (8) (Zhu and Sverjensky, 1992). It was calculated in the M7K micro mafic enclave. The pressure for this calculation was taken from M7K biotite, as calculated based on Uchida et al. (2007) with an average value of 100 MPa. The biotite-apatite pairs ($n = 3$) calculated F partition coefficient values are 40-50. The average equilibrium temperature is estimated to be in the range of 639-675 °C (average 652 °C) (see Appendix 2K).

5.4.2 Oxygen fugacity and H₂O content of magma

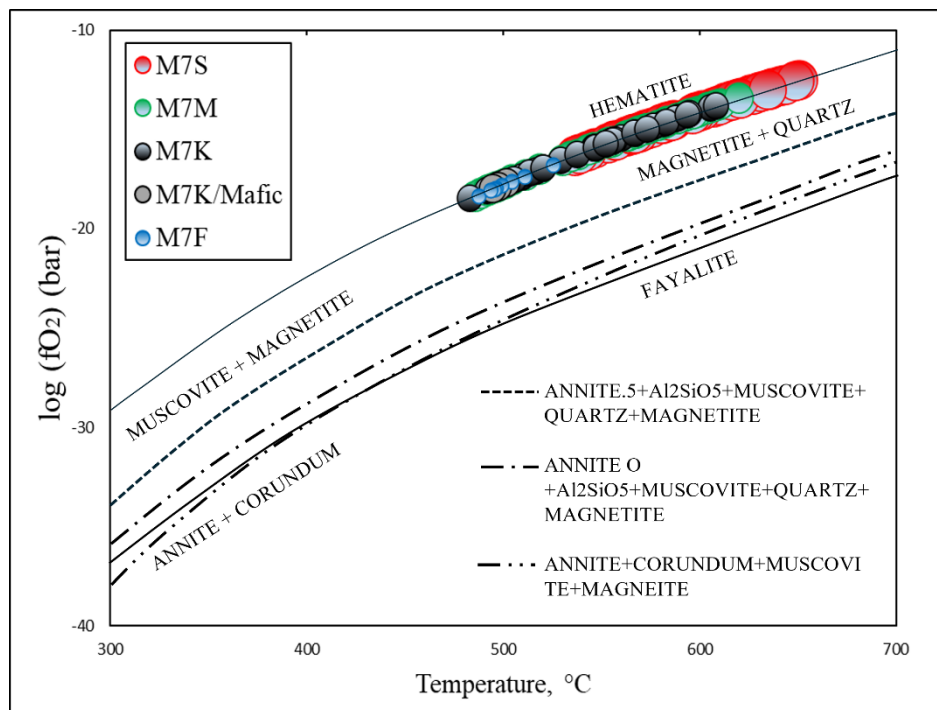
The estimation of $\log f_{\text{O}_2}$ using the Fe²⁺-Fe³⁺-Mg (apfu) ternary diagram (Wones and Eugster, 1965) indicates that the investigated biotites formed in oxidizing conditions, above the HM (hematite-magnetite) buffer, with only M7S plotting between the HM-NNO (nickel-nickel oxide) buffers (Fig. 19). The calculated $\log f_{\text{O}_2}$ contents using the method proposed by Wones and Eugster (1965) for biotite crystallization range from -18.5 to -12.5 (average -15) and plot on the Hematite buffer (Fig. 20, see Appendix 2B). The M7F biotites plot within the range from -18 to -17 (average -18), M7S from -16 to -12.5 (average -14), M7K from -18.5 to -13.8 (average -16) and mafic part -18 to -17.7 (average -17.8), and M7M from -18 to -13 (average -15; Fig. 20). The re-equilibrated biotites range from -18 to -12.5 (average -15), while in the secondary biotites range from -19 to -14 (average -17).

For the amphibole crystallisation, the calculated $\log f_{\text{O}_2}$ conditions were estimated using the Eq. (10) method proposed by Ridolfi et al. (2010). The M7F amphiboles calculated average $\log f_{\text{O}_2}$ are: -11 in the group normal #Mg<0.40, -11 normal #Mg>0.40, -12 dark #Mg 0.34-0.38, -11 dark #Mg 0.41-0.45 and -12 light #Mg<0.30 (see Appendix 2C). The M7K amphiboles calculated $\log f_{\text{O}_2}$ are: -11 in the group normal #Mg>0.40, -11 dark #Mg 0.41-0.45 and -11 light #Mg<0.40 (see Appendix 2C). The amphiboles that fit the calibration by Ridolfi (2021) $\log f_{\text{O}_2}$ in M7F range from -12.2 to -10.3 and M7K -11.9 to -10.8 (Fig. 21). It plots between the NNO and HM buffers (Fig. 21).

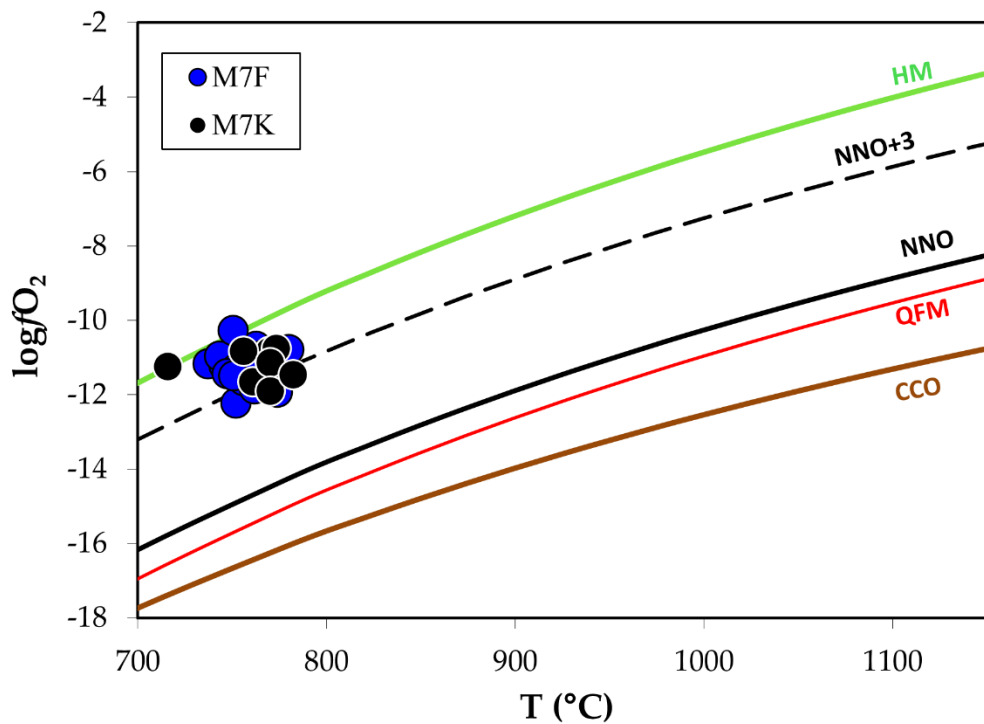
The calculated H₂O contents using Eq. (11) that fit the calibration by Ridolfi (2021) for amphibole crystallization in M7F range from 5.3 to 7.7 wt.% and M7K 5.7 to 8.3 wt.% (average 6.7 wt.%) (Fig. 22). For the other amphibole groups that do not fit the calibration conditions, the M7F amphiboles calculated average H₂O (wt.%) content are: 8 wt.% in the group normal #Mg<0.40, 7 wt.% normal #Mg>0.40, 7 wt.% dark #Mg 0.34-0.38, 8 wt.% dark #Mg 0.41-0.45 and 13 wt.% light #Mg<0.30 (see Appendix 2C). The M7K amphiboles calculated H₂O (wt.%) content are: 7 wt.% in the group normal #Mg>0.40, 6 wt.% dark #Mg 0.41-0.45 and 7 wt.% light #Mg<0.40 (see Appendix 2C).



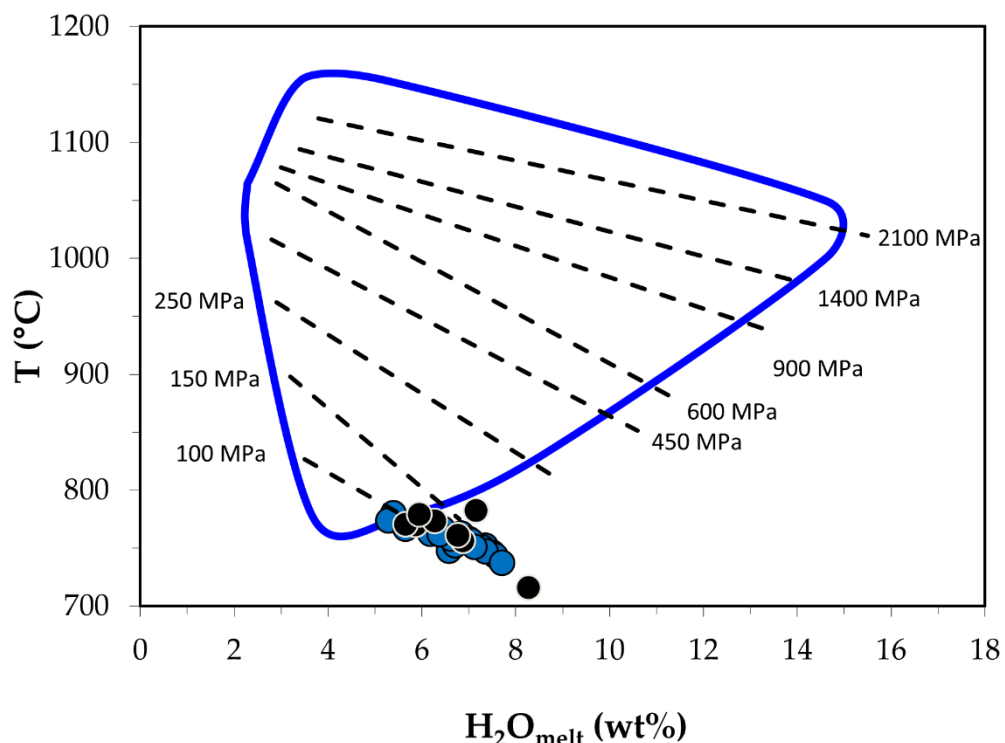
19 Figure. Estimates of oxygen fugacity from biotite Fe^{2+} - Fe^{3+} -Mg (apfu) ternary diagram (after Wones and Eugster, 1965).



20 Figure. Biotite+corundum \rightleftharpoons magnetite+muscovite and biotite+ Al_2SiO_5 \rightleftharpoons magnetite+muscovite+quartz oxidation reactions plotted as functions of f_{O_2} and temperature (Wones and Eugster, 1965) for the investigated M7 biotites.



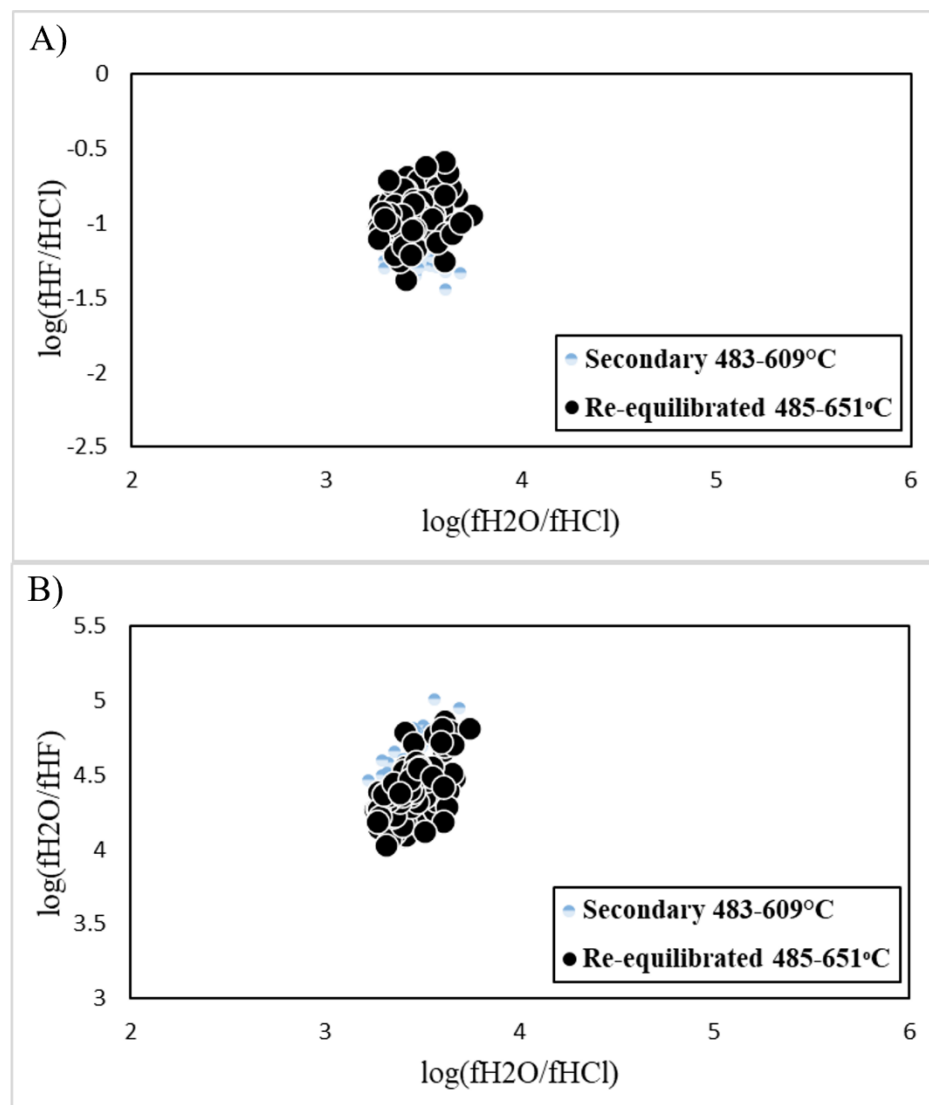
21 Figure. Log f_{O_2} vs T (°C) diagram for the investigated calibration fitted M7 amphiboles (calculations based on Ridolfi, 2021).



22 Figure. T (°C) vs. H_2O melt (wt.%) for the investigated M7 calibration fitted amphiboles. The blue line, drawn from experimental amphiboles shows the certainty of the T (°C) and H_2O melt (wt%) values (based on Ridolfi, 2021).

5.4.3 Halogen fugacity

The calculated $\log(f_{\text{H}_2\text{O}}/f_{\text{HF}})$, $\log(f_{\text{H}_2\text{O}}/f_{\text{HCl}})$, and $\log(f_{\text{HF}}/f_{\text{HCl}})$ ratios of the fluids in equilibrium with biotites, based on equations (12, 13, 14; by Munoz, 1984, 1992; Zhu and Sverjensky, 1992; Coulson et al., 2001; Rasmussen and Mortensen, 2013), are detailed in Appendix 2B. The $\log(f_{\text{H}_2\text{O}}/f_{\text{HCl}})$ ratio varies from 3.2 to 3.7 (average 3.5; Fig. 23). In the re-equilibrated biotites, the $\log(f_{\text{H}_2\text{O}}/f_{\text{HCl}})$ ratio ranges from 3.3 to 3.7 (average 3.5), while in the secondary it ranges from 3.2 to 3.7 (average 3.4) and mafic part 3.4–3.5 (average 3.4). The $\log(f_{\text{HF}}/f_{\text{HCl}})$ ratio spans from -1.4 to -0.6 (average -1.0) (Fig. 23A). In the re-equilibrated biotites, the $\log(f_{\text{HF}}/f_{\text{HCl}})$ ratio ranges from -1.4 to -0.6 (average -0.9), and in the secondary, it spans from -1.4 to -1.2 (average -1.3), mafic part ranges from -1.4 to -1.3 (-1.3) (Fig. 23A). The $\log(f_{\text{H}_2\text{O}}/f_{\text{HF}})$ ratio ranges from 4.0 to 5.0 (average 4.5) (Fig. 23B). In the re-equilibrated biotites, it ranges from 4.0 to 4.9 (average 4.4), while in the secondary it spans from 4.5 to 5.0 (average 4.7) and in the mafic part from 4.7 to 4.8 (average 4.7) (Fig. 23B).



23 Figure. A) $\log(f_{\text{HF}}/f_{\text{HCl}})$ vs. $\log(f_{\text{H}_2\text{O}}/f_{\text{HCl}})$; B) $\log(f_{\text{H}_2\text{O}}/f_{\text{HF}})$ vs. $\log(f_{\text{H}_2\text{O}}/f_{\text{HCl}})$ for the investigated biotites from M7 (calculations based by Munoz, 1984, 1992; Zhu and Sverjensky, 1992; Coulson et al., 2001; Rasmussen and Mortensen, 2013).

6. DISCUSSION

The detailed study of the textures and mineral composition of the M7 borehole provides new insights into the strongly and weakly altered granite and mafic xenoliths of the Kabeliai intrusion. The investigation of mineral compositions, alongside the application of geothermobarometry, facilitates the reconstruction of the intrusion development, type, physical parameters, and volatile content during its emplacement and subsequent alteration period. Understanding these parameters aids in clarifying the evolution of the intrusion and the conditions that led to Cu-Mo mineralisation.

6.1 Magma emplacement conditions

The intrusion started to crystallise from 850 °C to 990 °C (apatite), while from the zircon obtained temperatures, using the models of Boehnke et al. (2013) and Watson and Harrison (1983), yield values of 847 °C and 870 °C, respectively. The elevated temperatures (990 °C) from the apatite may reflect inheritance from micro-mafic enclaves, where apatite accumulation is commonly observed (Fig. 5A). Similarly, the amphiboles also point to an origin from a more mafic composition source. The temperature calculation based on amphibole chemistry (Ridolfi, 2021) yields an average crystallisation of ~759 °C (homogeneous #Mg > 0.40). The pressure derived from amphiboles points to upper crust conditions with an average value of 176 MPa, interpreted as intrusion emplacement depths of approximately 6 km.

Despite the albition effect observed in plagioclase, the weakly altered samples (M7K, M7M, and M7S) preserve magmatic textures including myrmekite, perthite, and antiperthite, indicating relatively slow cooling of the granitic intrusion (Fig. 5B; 6A–B; 7C–D).

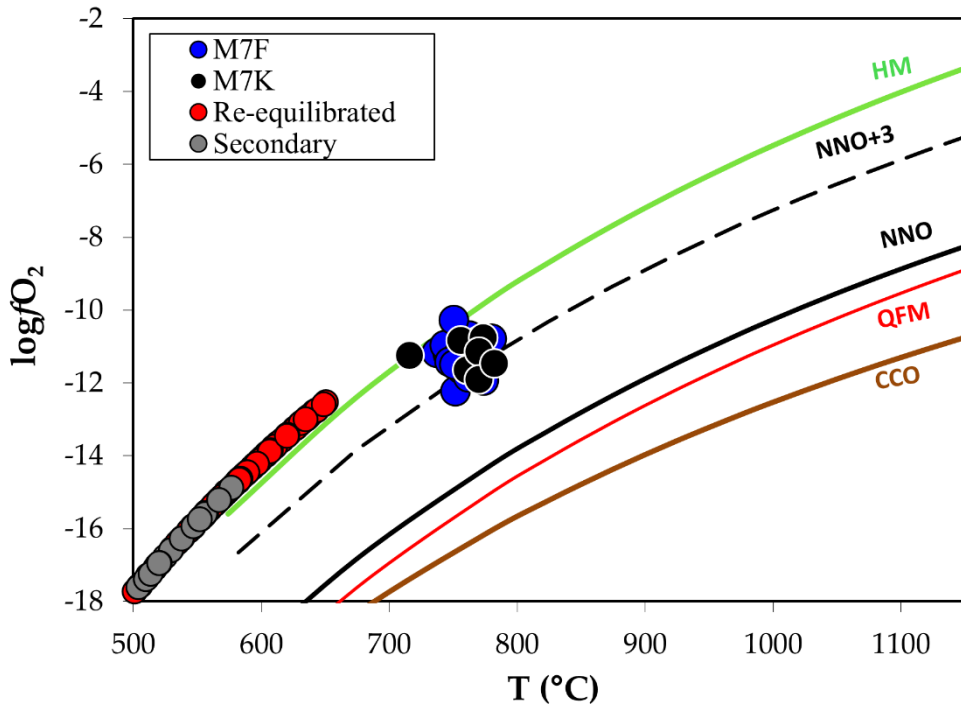
6.2 Late-stage melt crystallisation and post-magmatic alterations

The final stage of solidification is derived from re-equilibrated (compositionally close to annite) biotite with a temperature of an average of 579 °C and a pressure of 130 MPa. The other group of biotites, identified as secondary (more phlogopitic in composition), formed at lower temperatures (~525 °C) and lower pressures (~97 MPa) and indicates crystallisation under shallower post-magmatic conditions. The secondary biotite composition also differs, with higher #Mg values and elevated Cl content. Additionally, one group of amphiboles (light #Mg<30) has significantly modified chemistry, with a $\ln(\text{Cl}/\text{OH})$ ratio of -1.3, an ${}^{\text{IV}}\text{Al} \times \text{Fe}^{2+}$ (apfu) of 4.9, and an ${}^{\text{IV}}\text{Al} \times \text{Fe}^{2+} \times \text{K}$ (apfu) of 1.76. Both secondary biotites and amphibole (light #Mg<30) were influenced by Cl-rich (saline) hydrothermal fluid and could have formed in these lower-pressure and temperature conditions.

This interpretation is supported by the apatite-rim-biotite geothermometry, which indicates temperatures of 652 °C in the mafic enclave. Relatively low apatite saturation temperatures here (773.3 °C), confirming a significant hydrothermal reworking. This suggests that sample M7/293.351 has been strongly affected by alteration, whereas the M7K mafic enclave was likely incorporated into the intrusion as a xenolith and experienced cooling and re-equilibration during fluid overprint.

6.3 The oxygen fugacity, water content and volatiles

The Oxygen fugacity f_{O_2} estimations for re-equilibrated biotites and amphiboles plot above the NNO buffer (Fig. 24; Wones and Eugster, 1965; Ridolfi et al., 2010). The samples from the upper parts, particularly those containing secondary biotites and some of the M7F homogeneous #Mg>0.40 amphiboles, were affected by more oxidising conditions, exceeding the hematite-magnetite (HM) buffer (Fig. 19; 24). Additionally, magnetite grains exposed to these more oxidised conditions are transforming into hematite, further confirming the oxidising nature of the post-magmatic environment (Fig. 6D). Thus, as the system was cooling, the oxygen fugacity was increasing.



24 Figure. Log f_{O_2} vs T (°C) diagram for the investigated calibration fitted M7 amphiboles and re-equilibrated and secondary biotites (Ridolfi, 2021; Wones and Eugster, 1965)

The volatile component ratios of re-equilibrated and secondary biotites, $\log(f_{\text{H}_2\text{O}}/f_{\text{HCl}})$ and $\log(f_{\text{HF}}/f_{\text{HCl}})$, are higher in the former (3.3 to 3.7; -1.4 to -0.6) than in the latter (3.2 to 3.7; -1.4 to -1.2). It indicates that re-equilibrated biotites formed in water-rich and fluorine-dominated conditions. In contrast, secondary biotites show elevated $\log(f_{\text{H}_2\text{O}}/f_{\text{HF}})$ values (4.5 to 5.0) and relatively higher Cl enrichment, suggesting a more chlorine-rich environment. The plagioclases changing to albite (albite rim; Fig. 4B; 5B), light and dark amphibole zones (Fig. 4A,C; Fig. 5C) are evidence of a hydrothermal alteration-albitization. This alteration type is related to saline fluids that can cause element exchange in a subsolidus state (Baker J.H., 1985, Hammerli, 2018). The saline fluid brought sodium and silica to plagioclases, and leached Ca and Al from it. In this instance, the Fe-rich amphiboles act as a sink for Ca and Al. The more phlogopitic biotite formed from the reequilibrated more annitic biotite at this stage provided the Fe needed for these amphiboles. This alteration is most prominent next to the mafic enclaves, where Fe-rich amphibole is the main Al sink. Samples that do not contain mafic enclaves are less altered. However, local albitization is observed, followed by the formation of secondary biotites (depleted in Fe, enriched in Mg and Cl) and an Al-rich phase such as chlorite, epidote and muscovite, and often contains calcite and siderite.

Amphiboles that fit the calibration criteria of Ridolfi (2021) exhibit water contents ranging from 5.3 to 7.7 wt.% in sample M7F, and from 5.7 to 8.3 wt.% in M7K, indicating a generally hydrous magmatic environment. The most fluid-rich conditions are recorded in the M7F amphiboles ($\text{#Mg} < 0.30$), which show significantly elevated water contents, ranging from 10 to 17 wt.% and are more indicative of a hydrothermal than igneous environment.

The estimated oxygen fugacity $f(\text{O}_2)$ conditions (NNO + 1 to HM) could be a key factor for Cu-Mo precipitation. Porphyry-type copper deposits are associated with relatively oxidised magmas (Richards 2003, 2005). High oxygen fugacity ($f(\text{O}_2)$) controls the migration and speciation of sulfur and the subsequent stability of sulfides in magma (Pan et al., 2022). In silicate melts, sulfur dissolves as SO_4^{2-} sulfate and SO_2 sulfur dioxide under high oxygen fugacity conditions. This facilitates the transport of copper as chlorine complexes (Bi et al., 2009; Li et al., 2008; Tang et al., 2019). High oxygen fugacity ($f(\text{O}_2)$) in magma prevents the early crystallisation of sulfide phases, thereby inhibiting the removal of chalcophile elements and enriching the fluid phase in metals during post-magmatic processes (Carroll and Rutherford, 1985; Richards, 2003). According to the $f(\text{O}_2)$ estimates from biotite and amphibole, the M7 borehole indicates elevated oxidation states that increased progressively during the evolution of the magma and subsequent hydrothermal activity. This geochemical evolution likely promoted the formation of a sulfur-rich fluid phase capable of concentrating and transporting Cu and Mo, leading to their precipitation during the post-magmatic stage.

6.4 Regional context

A-type granites are divided into two categories: ilmenite-bearing reduced granites and oxidised magnetite-bearing granites (Anderson and Morrison, 2005). In the southeast EEC, the A-type oxidised magnetite-bearing granites are predominant, for example, in Northern Poland. This type of granite also fits the Kabeliai intrusion very well. It is characterised by high $\text{CaO} + \text{Al}_2\text{O}_3$ (15.4 wt%), a moderate $\text{Al}_2\text{O}_3/(\text{K}_2\text{O} + \text{Na}_2\text{O})$ ratio of 8.7. The high whole-rock $\text{FeOt}/(\text{FeOt} + \text{MgO})$ ratio, averaging 0.83, and the presence of magnetite in the studied mineral assemblages correspond with an A-type granite (Anderson and Morrison, 2005).

From a regional perspective, the Kabeliai intrusion can be compared to those in the Mazury complex of the AMCG suite, specifically the rapakivi-like A-type granites (Northern Poland): HBG (hornblende-biotite granite suite) (Duschene et al., 2010) and the Krasnopol intrusion (Domańska-Siuda et al., 2024). The 1.5 Ga Krasnopol granitoid intrusion is ferroan and metaluminous, exhibiting characteristics of A-type granites, and it hosts mafic rocks referred to as microgranular enclaves (Domańska-Siuda et al., 2024). The 1.5 Ga HBG suite consists of A-type, oxidised, metaluminous granitoids (Duschene et al., 2010).

The emplacement conditions in these intrusions are comparable. Zircon crystallisation temperatures in Kabeliai (870°C, Watson and Harrison, 1983; 847°C, Boehnke et al., 2013) align closely with those in Krasnopol (790–850°C, Domańska-Siuda et al., 2024). Amphibole thermobarometry for Krasnopol granitoids indicates temperatures between 747–783°C and pressures ranging from 420 to 460 MPa (Domańska-Siuda et al., 2024), whereas the HBG suite records pressures of 200–300 MPa for Klewno and 400–500 MPa for other massifs (Duchesne et al., 2010). From Kabeliai intrusion-derived mafic xenoliths, amphibole temperature and pressure measurements (716–782°C; 145–249 MPa) indicate lower temperatures and shallower crystallisation depths. Estimates of water content further differentiate the intrusions: Krasnopol shows approximately 5% (Domańska-Siuda et al., 2024), while Kabeliai displays higher values (5.3–8.3%), suggesting a more

hydrous magmatic system. These results indicate that intrusions are similar in terms of age and geochemical affinity but show minor differences in emplacement, temperature, and water content of magma. This could be interpreted as the continuous lineament of west-east AMCG A-type intrusions becoming gradually younger and emplaced in shallower depths.

One of the key questions in understanding the formation of the Kabeliai intrusion is its tectonic setting. Many porphyry Cu-Mo deposits are associated with calc-alkaline magmatic arc environments related to the subduction of oceanic slabs (Richards, 2003; 2005; Cooke et al., 2005). However, porphyry-style mineralisation can also develop in collisional and intracontinental settings (Hou et al., 2011). From the regional perspective, crust aggregation in the southeast of the EEC stopped approximately around 1.75 Ga followed by late extensional Mesoproterozoic magmatism, suggesting the Kabeliai granites formation to take place in a similar extensional and anorogenic tectonic setting.

7. CONCLUSIONS

1. The M7 borehole granites intermixed with mafic enclaves and xenoliths, exhibiting varying degrees of post-magmatic alteration. Feldspars preserve primary magmatic textures (e.g., myrmekite, perthite, antiperthite), indicating slow magma cooling. The plagioclase changes to albite provide evidence of albitization during late-stage alteration. Biotites, typical of anorogenic-alkaline suites, are categorised into Fe-rich re-equilibrated types (annite) and Mg-rich secondary types (phlogopite). Amphiboles consist of primary igneous pargasites, while apatites are fluorapatites with patchy zoning.
2. Temperature and pressure estimations indicate that crystallisation of the main igneous rock-forming minerals occurred at high temperatures, with average estimates of ~870–847 °C (zircon), ~850 °C (apatite) and ~759 °C (amphibole). The final igneous solidification stage is marked by re-equilibrated biotites forming at ~579 °C. The mafic enclaves/xenoliths record higher pressures ~176 MPa (amphibole), while re-equilibrated biotites in the granite suggest slightly lower pressures ~130 MPa, both stating emplacement conditions within the upper crust.
3. The post magmatic activity is distinguished by re-equilibrated lower temperatures of 773.3 °C (apatite), 652 °C (apatite-biotite) and crystallisation of secondary biotite at an average of 525 °C. A lower pressure of an average of 97 MPa (secondary biotite) suggests shallower depths.
4. The intrusion is characterised by elevated oxygen fugacity in magma, with f_{O_2} values plotting above the NNO buffer. Amphibole-based estimations indicate high water contents ranging from 5.3 to 8.3 wt.%, supporting a hydrous magmatic origin. During post-magmatic stages, the system was exposed to even more oxidising conditions, with f_{O_2} levels exceeding the hematite–magnetite (HM) buffer.
5. The volatile component ratios obtained from re-equilibrated biotite suggest that magma was water-rich ($\log(f_{\text{H}_2\text{O}}/f_{\text{HF}})$ from 4.0 to 4.9) and fluorine-dominated ($\log(f_{\text{HF}}/f_{\text{HCl}})$ from -1.4 to -0.6) during crystallisation. In contrast, the post-magmatic environment was characterised by enrichment in Cl ($\log(f_{\text{HF}}/f_{\text{HCl}})$ from -1.4 to -1.2), confirming the saline-rich fluid presence.
6. The elevated oxygen fugacity prevented early sulfide crystallisation and kept Cu and Mo in the melt. These metals precipitated from the fluid phase with decompression (lower pressure) and rising oxygen fugacity (to HM).

8. ACKNOWLEDGEMENTS

I would like to thank Gražina Skridlaitė and Olga Demina for their support and for providing the samples, as well as Gediminas Motuza and Olga Demina for supplying the whole rock chemistry.

I am very grateful to Gražina Skridlaitė and Laurynas Šiliauskas for providing the opportunity to investigate thin sections using Scanning Electron Microscopy at the Nature Research Centre in Vilnius, Lithuania, and an Electron Probe Microanalyser (EPMA) at the Institute of Geochemistry, Mineralogy, and Petrology at Warsaw University in Poland. I want to thank Petras Jokubauskas for his guidance and assistance during the EPMA analysis session.

Most of all, I would like to express my appreciation to my supervisor, Laurynas Šiliauskas, for all the support during the SEM sessions, for the valuable discussions, and for his guidance throughout the entire research process.

Lastly, I would like to thank my friends and family for their support and understanding.

REFERENCES

- Abdel-Rahman, A.F.M. (1994). Nature of Biotites from Alkaline, Calc-alkaline, and Peraluminous Magmas. *Journal of Petrology*, 35, pp.525–541. doi:<https://doi.org/10.1093/petrology/35.2.525>.
- Anderson, J. and Morrison, J. (2005). Ilmenite, magnetite, and Peraluminous Mesoproterozoic Anorogenic Granites of Laurentia and Baltica. *Lithos*, 80(1-4), pp.45–60. doi:<https://doi.org/10.1016/j.lithos.2004.05.008>.
- Baker, J.H. (1985). Rare Earth and Other Trace Element Mobility Accompanying Albitionization in a Proterozoic granite, W. Bergslagen, Sweden. *Mineralogical Magazine*, 49(350), pp.107–115. doi:<https://doi.org/10.1180/minmag.1985.049.350.17>.
- Bi, X., Hu, R. and Hanley, J.J. (2009). Crystallisation Conditions (T, P, fO₂) from Mineral Chemistry of Cu- and Au-mineralised Alkaline Intrusions in the Red River–Jinshajiang Alkaline Igneous belt, Western Yunnan Province, China. *Mineralogy and Petrology*, 96, pp.43–58. doi:<https://doi.org/10.1007/s00710-009-0047-4>.
- Boehnke, P., Watson, E.B., Trail, D., Harrison, T.M. and Schmitt, A.K. (2013). Zircon Saturation re-revisited. *Chemical Geology*, 351, pp.324–334. doi:<https://doi.org/10.1016/j.chemgeo.2013.05.028>.
- Bogdanova, S., Gorbatschev, R., Skridlaite, G., Soesoo, A., Taran, L. and Kurlovich, D. (2015). Trans-Baltic Palaeoproterozoic Correlations Towards the Reconstruction of Supercontinent Columbia/Nuna. *Precambrian Research*, 259, pp.5–33. doi:<https://doi.org/10.1016/j.precamres.2014.11.023>.
- Bogdanova, S.V., Gorbatschev, R. and Garetsky, R.G. (2016). EUROPE|East European Craton. *Reference Module in Earth Systems and Environmental Sciences*, pp.1–18. doi:<https://doi.org/10.1016/B978-0-12-409548-9.10020-X>.
- Burnham, A.D., Mallmann, G. and Fonseca, R.O.C. (2021). Mineral-Melt Partitioning of Redox-Sensitive Elements. *Magma Redox Geochemistry*, pp.345–367. doi:<https://doi.org/10.1002/essoar.10503118.1>.
- Carroll, M.R. and Rutherford, M.J. (1985). Sulfide and Sulfate Saturation in Hydrous Silicate Melts. *Journal of Geophysical Research*, 90(S02), pp.C601–C612. doi:<https://doi.org/10.1029/jb090is02p0c601>.
- Cecys, A. and Benn, K. (2007). Emplacement and Deformation of the ca. 1.45 Ga Karlshamn Granitoid pluton, Southeastern Sweden, during ENE-WSW Danopolonian Shortening. *International Journal of Earth Sciences*, 96, pp.397–414. doi:<https://doi.org/10.1007/s00531-006-0114-6>.
- Cooke, D.R., Hollings, P. and Walshe, J.L. (2005). Giant Porphyry Deposits: Characteristics, Distribution, and Tectonic Controls. *Economic Geology*, 100, pp.801–818. doi:<https://doi.org/10.2113/gsecongeo.100.5.801>.

Coulson, I., Dipple, G. and Raudsepp, M. (2001). Evolution of HF and HCl Activity in Magmatic Volatiles of the gold-mineralized Emerald Lake pluton, Yukon Territory, Canada. *Mineralium Deposita*, 36, pp.594–606. doi:<https://doi.org/10.1007/s001260100191>.

Dall’Agnol, R. and de Oliveira, D.C. (2007). Oxidized, magnetite-series, rapakivi-type granites of Carajás, Brazil: Implications for classification and petrogenesis of A-type granites. *Lithos*, 93(3-4), pp.215–233. doi:<https://doi.org/10.1016/j.lithos.2006.03.065>.

Deer, W.A., Howie, R.A. and Zussman, J. (1963). *Rock-forming Minerals*.

Domańska-Siuda, J., Grabarczyk-Gurba, A. and Nejbert, K. (2024). Petrogenesis of Microgranular Enclaves in the A-type Granitoid Krasnopol Intrusion (Mazury Complex, Northeastern Poland): Evidence of Magma Mixing. *Mineralogy and Petrology*, 118, pp.401–426. doi:<https://doi.org/10.1007/s00710-024-00866-1>.

Duchesne, J.C., Martin, H., Baginski, B., Wiszniewska, J. and Vander Auwera, J. (2010). The Origin of ferroan-potassic A-type granitoids: the Case of the Hornblende–biotite Granite Suite of the Mesoproterozoic Mazury complex, Northeastern Poland. *The Canadian Mineralogist*, 48, pp.947–968. doi:<https://doi.org/10.3749/canmin.48.4.947>.

Enami, M., Liou, J. and Bird, D.K. (1992). Cl-bearing Amphibole in the Salton Sea Geothermal system, California. *Canadian Mineralogist*, 30, pp.1077–1092.

Fleet, M.E. and Barnett, R.L. (1978). Al iv /Al vi partitioning in calciferous amphiboles from the Frood Mine, Sudbury, Ontario. *The Canadian Mineralogist*, 16(4), pp.527–532.

Hammerli, J. and Rubenach, M. (2018). The Role of Halogens During Regional and Contact Metamorphism. *Springer Geochemistry*, pp.649–712. doi:https://doi.org/10.1007/978-3-319-61667-4_10.

Harrison, T.M. and Watson, E.B. (1984a). The Behavior of Apatite during Crustal Anatexis Equilibrium and Kinetic Considerations. *Geochimica Et Cosmochimica Acta*, 48, pp.1467–1477. doi:[http://dx.doi.org/10.1016/0016-7037\(84\)90403-4](http://dx.doi.org/10.1016/0016-7037(84)90403-4).

Harrison, T.M. and Watson, E.B. (1984b). The behavior of apatite during crustal anatexis: Equilibrium and kinetic considerations. *Geochimica et Cosmochimica Acta*, 48(7), pp.1467–1477. doi:[https://doi.org/10.1016/0016-7037\(84\)90403-4](https://doi.org/10.1016/0016-7037(84)90403-4).

Hawthorne, F.C., Oberti, R., Harlow, G.E., Maresch, W.V., Martin, R.F., Schumacher, J.C. and Welch, M.D. (2012). Nomenclature of the Amphibole Supergroup. *American Mineralogist*, 97(11-12), pp.2031–2048. doi:<https://doi.org/10.2138/am.2012.4276>.

Henry, D.J., Guidotti, C.V. and Thomson, J.A. (2005). The Ti-saturation surface for low-to-medium pressure metapelitic biotites: Implications for geothermometry and Ti-substitution mechanisms. *American Mineralogist*, 90, pp.316–328. doi:<https://doi.org/10.2138/am.2005.1498>.

Hey, M.H. (1954). A new review of the chlorites. *Mineralogical Magazine and Journal of the Mineralogical Society*, 30(224), pp.277–292. doi:<https://doi.org/10.1180/minmag.1954.030.224.01>.

Hou, Z., Zhang, H., Pan, X. and Yang, Z. (2011). Porphyry Cu (–Mo–Au) Deposits Related to Melting of Thickened Mafic Lower crust: Examples from the Eastern Tethyan Metallogenic Domain. *Ore Geology Reviews*, 39(1-2), pp.21–45. doi:<https://doi.org/10.1016/j.oregeorev.2010.09.002>.

Ito, E. and Anderson, A.T. (1983). Submarine Metamorphism of Gabbros from the Mid-Cayman Rise: Petrographic and Mineralogic Constraints on Hydrothermal Processes at slow-spreading Ridges. *Contributions to Mineralogy and Petrology*, 82, pp.371–388. doi:<https://doi.org/10.1007/bf00399714>.

Janoušek, V. (2006). Saturnin, R Language Script for Application of accessory-mineral Saturation Models in Igneous Geochemistry. *Geologica Carpathica*, 57, pp.131–142.

Johansson, A., Bogdanova, S. and Cecys, A. (2006). A Revised Geochronology for the Blekinge Province, Southern Sweden. *GFF*, 128(4), pp.287–302. doi:<https://doi.org/10.1080/11035890601284287>.

Johansson, Å., Waight, T.E., Andersen, T. and Simonsen, S.L. (2016). Geochemistry and Petrogenesis of Mesoproterozoic A-type Granitoids from the Danish Island of Bornholm, Southern Fennoscandia. *Lithos*, 244(1), pp.94–108. doi:<https://doi.org/10.1016/j.lithos.2015.11.031>.

Kieffer, M.A., Dare, S.A.S., Namur, O. and Mansur, E.T. (2024). Apatite Chemistry as a Petrogenetic Indicator for Mafic Layered Intrusions. *Journal of Petrology*, 65(4). doi:<https://doi.org/10.1093/petrology/egae022>.

Krzemińska, E., Johansson, Å.E., Leszek Krzemiński, Wiszniewska, J., Williams, Ian.S., Petecki, Zdzisław. and Salwa, Sylwester. (2021). Basement Correlation across the Southernmost Baltic Sea: Geochemical and Geochronological Evidence from Onshore and Offshore Deep Drill cores, Northern Poland. *Precambrian Research*, 362, p.106300. doi:<https://doi.org/10.1016/j.precamres.2021.106300>.

Leake, B.E. (1971). On Aluminous and Edenitic Hornblendes. *Mineralogical Magazine*, 38, pp.389–407. doi:<https://doi.org/10.1180/minmag.1971.038.296.01>.

Li, J.W., Zhao, X.-F. and Zhou, M.-F. (2008). Origin of the Tongshankou Porphyry-skarn Cu–Mo deposit, Eastern Yangtze craton, Eastern China: geochronological, geochemical, and Sr–Nd–Hf Isotopic Constraints. *Mineralium Deposita*, 43, pp.315–336. doi:<https://doi.org/10.1007/s00126-007-0161-3>.

Li, X., Zhang, C., Behrens, H. and Holtz, F. (2020). Calculating Biotite Formula from Electron Microprobe Analysis Data Using a Machine Learning Method Based on Principal Components Regression. *Lithos*, 356-357, p.105371. doi:<https://doi.org/10.1016/j.lithos.2020.105371>.

Mansfeld, J. (2001). Age and ϵ Nd constraints on the Palaeoproterozoic tectonic evolution in the Baltic-Sea region. *Tectonophysics*, 339(1-2), pp.135–151. doi:[https://doi.org/10.1016/s0040-1951\(01\)00036-1](https://doi.org/10.1016/s0040-1951(01)00036-1).

Marfin, S., Miksys, R.B., Motuza, G. and Skripkina, T. (1982). The Structure of the Marcinkony Granitic Massif and Properties of Rocks. *Geologija (Lithuania)*, 3, pp.3–16. (in

Russian).

Martèse, R., Ruffet, G., Poujol, M., Boulvais, P. and Ireland, T.R. (2011). Simultaneous Resetting of the Muscovite K-Ar and Monazite U-Pb geochronometers: a Story of Fluids. *Terra Nova*, 23(6), pp.390–398. doi:<https://doi.org/10.1111/j.1365-3121.2011.01024.x>.

Miller, C.F., Stoddard, E.F., Bradfish, L.J. and Dollase, W.A. (1981). Composition of Plutonic Muscovite Genetic Implications. *Canadian Mineralogist*, 19, pp.25–34.

Morrison, J. (1991). Compositional Constraints on the Incorporation of Cl into Amphiboles. *American Mineralogist*, 76(11-12), pp.1920–1930.

Munoz, J.L. (1984). F-OH and Cl-OH EXCHANGE in MICAS with APPLICATIONS to HYDROTHERMAL ORE DEPOSITS. *Rev Mineral Geochemistry*, 13, pp.469–494. doi:<https://doi.org/10.1515/9781501508820-015>.

Munoz, J.L. (1992). *Calculation of HF and HCl Fugacities from Biotite compositions: Revised Equations*. Geological Society of America, Abstracts with Programs., 26 p A221.

Nachit, H., Ibhi, A., Abia, E.H. and Ohoud, M.E. (2005). Discrimination between Primary Magmatic biotites, Reequilibrated Biotites and Neoformed Biotites. *Comptes Rendus Geoscience*, 337(16), pp.1415–1420. doi:<https://doi.org/10.1016/j.crte.2005.09.002>.

Pan, Y., Dong, G., Tsunogae, T., Wang, P., Li, X. and Dong, P. (2022). Geochemical Characteristics of Biotite and Apatite from the Zhongdian Porphyry Cu Deposit Belt in Northwest Yunnan, China: an Indicator of Halogen Fugacity and Mineralization. doi:<https://doi.org/10.21203/rs.3.rs-1981660/v1>.

Rämö, O.T., Huhma, H. and Kirs, J. (1996). Radiogenic Isotopes of the Estonian and Latvian Rapakivi Granite suites: New Data from the Concealed Precambrian of the East European Craton. *Precambrian Research*, 79(3-4), pp.209–226. doi:[https://doi.org/10.1016/s0301-9268\(95\)00083-6](https://doi.org/10.1016/s0301-9268(95)00083-6).

Rasmussen, K.L. and Mortensen, J.K. (2013). Magmatic Petrogenesis and the Evolution of (F:Cl:OH) Fluid Composition in Barren and Tungsten skarn-associated Plutons Using Apatite and Biotite compositions: Case Studies from the Northern Canadian Cordillera. *Ore Geology Reviews*, 50, pp.118–142. doi:<https://doi.org/10.1016/j.oregeorev.2012.09.006>.

Richards, J.P. (2003). Tectono-Magmatic Precursors for Porphyry Cu-(Mo-Au) Deposit Formation. *Economic Geology*, 98(8), pp.1515–1533. doi:<https://doi.org/10.2113/gsecongeo.98.8.1515>.

Richards, J.P. (2005). Cumulative Factors in the Generation of Giant Calc-Alkaline Porphyry Cu Deposits. In: Porter, T.M. (Ed.), *Super-Porphyry Copper & Gold Deposits: a Global Perspective*. PGC Publishing, Adelaide, pp.7–25.

Ridolfi, F. (2021). Amp-TB2: an Updated Model for Calcic Amphibole Thermobarometry. *Minerals*, 11(3), p.324. doi:<https://doi.org/10.3390/min11030324>.

Ridolfi, F. and Renzulli, A. (2012). Calcic Amphiboles in calc-alkaline and Alkaline magmas:

Thermobarometric and Chemometric Empirical Equations Valid up to 1,130°C and 2.2 GPa. *Contributions to Mineralogy and Petrology*, 163, pp.877–895. doi:<https://doi.org/10.1007/s00410-011-0704-6>.

Ridolfi, F., Renzulli, A. and Puerini, M. (2010). Stability and chemical equilibrium of amphibole in calc-alkaline magmas: an overview, new thermobarometric formulations and application to subduction-related volcanoes. *Contributions to Mineralogy and Petrology*, 160, pp.45–66. doi:<https://doi.org/10.1007/s00410-009-0465-7>.

Rieder, M., Cavazzini, G., D'yakonov, Yu.S., Frank-Kamenetskii, V.A., Gottardi, G., Guggenheim, S., Koval', P.V., Müller, G., Neiva, A.M.R., Radoslovich, E.W., Robert, J.L. Sassi, F.P., Takeda, H., Weiss, Z. and Wones, D.R. (1998). Nomenclature of the Micas. *Mineralogical Magazine*, 63(2), pp.267–279. doi:<https://doi.org/10.1180/minmag.1999.063.2.13>.

Salin, E., Sundblad, K. and Lahaye, Y. (2021a). A 1.85 Ga Volcanic Arc Offshore the proto-continent Fennoscandia in Southern Sweden. *Precambrian Research*, 356, p.106134. doi:<https://doi.org/10.1016/j.precamres.2021.106134>.

Salin, E., Sundblad, K., Woodard, J. and O'Brien, H. (2019). The Extension of the Transscandinavian Igneous Belt into the Baltic Sea Region. *Precambrian Research*, 328, pp.287–308. doi:<https://doi.org/10.1016/j.precamres.2019.04.016>.

Salin, E., Woodard, J. and Sundblad, K. (2021b). Tracing the SW border of the Svecfennian Domain in the Baltic Sea region: evidence from petrology and geochronology from a granodioritic migmatite. *International Journal of Earth Sciences*, 110, pp.1027–1047. doi:<https://doi.org/10.1007/s00531-021-02005-z>.

Sato, H., Yamaguchi, Y. and Makino, K. (1997). Cl Incorporation into Successively Zoned Amphiboles from the Ramnes cauldron, Norway. *American Mineralogist*, 82, pp.316–324. doi:<https://doi.org/10.2138/am-1997-3-410>.

Siliauskas, L., Skridlaite, G., Whitehouse, M. and Soesoo , A. (2018). A ca.1.89 Ga Magmatic Complex in Eastern Lithuania: a Link Connecting with the Domains in Estonia and the Bergslagen Terrane in Sweden. In: *Geophys. Res. Abstr. Vol. 20, EGU2018-3050, EGU General Assembly*.

Skridlaite G., Baginski, B. and Whitehouse, M. (2008). Significance of ~ 1.5 Ga Zircon and Monazite Ages from Charnockites in Southern Lithuania and NE Poland. *Gondwana Research*, 14(4), pp.663–674. doi:<https://doi.org/10.1016/j.gr.2008.01.009>.

Skridlaite, G., Siliauskas, L., Whitehouse, M.J., Johansson, Å. and Rimsa, A. (2021). On the Origin and Evolution of the 1.86–1.76 Ga Mid-Baltic Belt in the Western East European Craton. *Precambrian Research*, 367, p.106403. doi:<https://doi.org/10.1016/j.precamres.2021.106403>.

Skridlaite, G., Whitehouse, M., Bogdanova, S. and Taran, L. (2011). The 1.86-1.84 Ga Magmatism in the Western East European Craton (Lithuania): Implications for a Convergent Continental Margin. Int. Goldshmidt Conference, Prague Goldshmidt Conference Abstract 75(3), 1890.

Skridlaite, G., Wiszniewska, J. and Duchesne, J.C. (2003b). Ferro-potassic A-type Granites and Related Rocks in NE Poland and S Lithuania: West of the East European Craton. *Precambrian Research*, 124(2-4), pp.305–326. doi:[https://doi.org/10.1016/s0301-9268\(03\)00090-1](https://doi.org/10.1016/s0301-9268(03)00090-1).

Stein, H., Sundblad, K., Markey, R.J., Morgan, E.R. and Motuza, G. (1998). Re-Os Ages for Archean Molybdenite and pyrite, Kuittila-Kivisuo, Finland and Proterozoic molybdenite, Kabeliai, Lithuania: Testing the Chronometer in a Metamorphic and Metasomatic Setting. *Mineral. Deposita*, 33, pp.329–345. doi:<https://doi.org/10.1007/s001260050153>.

Sundblad, K.J., Mansfeld, J., Motuza, G., Ahl, M. and Claesson, S. (1994). Geology, Geochemistry and Age of a Cu-Mo-bearing Granite at Kabeliai, Southern Lithuania. *Mineralogy and Petrology*, 50, pp.43–57. doi:<https://doi.org/10.1007/BF01160138>.

Suwa, K., Enami, M. and Horiuchi, T. (1987). Chlorine-rich Potassium Hastingsite from West Ongul Island, Liitzow-Holm Bay, East Antarctica. *Mineralogical Magazine*, 51, pp.709–714.

Tang, P., Tang, J., Lin, B., Wang, L., Zheng, W., Leng, Q., Gao, X., Zhang, Z. and Tang, X.-Q. (2019). Mineral Chemistry of Magmatic and Hydrothermal Biotites from the Bangpu Porphyry Mo (Cu) deposit, Tibet. *Ore Geology Reviews*, 115. doi:<https://doi.org/10.1016/j.oregeorev.2019.103122>.

Uchida, E., Endo, S. and Makino, M. (2007). Relationship between Solidification Depth of Granitic Rocks and Formation of Hydrothermal Ore Deposits. *Resource Geology*, 57(1), pp.47–56. doi:<https://doi.org/10.1111/j.1751-3928.2006.00004.x>.

Vanko, D. (1986). High-chlorine Amphiboles from Oceanic rocks: Product of Highly Saline Hydrothermal Fluids. *American Mineralogist*, 71, pp.51–59.

Warr, L.N. (2021). IMA–CNMNC approved mineral symbols. *Mineralogical Magazine*, 85(3), pp.291–320. doi:<https://doi.org/10.1180/mgm.2021.43>.

Watson, E.B. and Harrison, T.J. (1984). Accessory Minerals and the Geochemical Evolution of Crustal Magmatic systems: a Summary and Prospectus of Experimental Approaches. *Physics of the Earth and Planetary Interiors*, 35(1-3), pp.19–30. doi:[https://doi.org/10.1016/0031-9201\(84\)90031-1](https://doi.org/10.1016/0031-9201(84)90031-1).

Watson, E.B. and Harrison, T.M. (1983). Zircon Saturation revisited: Temperature and Composition Effects in a Variety of Crustal Magma Types. *Earth and Planetary Science Letters*, 64(2), pp.295–304. doi:[https://doi.org/10.1016/0012-821X\(83\)90211-X](https://doi.org/10.1016/0012-821X(83)90211-X).

Wiszniewska, J. and Krzemińska, E. (2021). Advances in Geochronology in the Suwałki Anorthosite Massif and Subsequent Granite veins, Northeastern Poland. *Precambrian Research*, 361, p.106265. doi:<https://doi.org/10.1016/j.precamres.2021.106265>.

Wones, R.D. and Eugster, H.P. (1965). Stability of biotite: experiment, theory, and Application. *The American Mineralogist*, 50(9), pp.1228–1272. doi:<https://pubs.geoscienceworld.org/msa/ammin/article-abstract/50/9/1228/540155/Stability-of-biotite-experiment-theory-and>.

Zariņš, K. and Johansson, Å. (2009). U–Pb Geochronology of Gneisses and Granitoids from the Danish Island of Bornholm: New Evidence for 1.47–1.45 Ga Magmatism at the Southwestern Margin of the East European Craton. *International Journal of Earth Sciences*, 98, pp.1561–1580. doi:<https://doi.org/10.1007/s00531-008-0333-0>.

Zhu, C. and Sverjensky, D.A. (1991). Partitioning of F-Cl-OH between Minerals and Hydrothermal Fluids. *Geochimica Et Cosmochimica Acta*, 55(7), pp.1837–1858. doi:[https://doi.org/10.1016/0016-7037\(91\)90028-4](https://doi.org/10.1016/0016-7037(91)90028-4).

Zhu, C. and Sverjensky, D.A. (1992). F-Cl-OH Partitioning between Biotite and Apatite. *Geochimica Et Cosmochimica Acta*, 56(9), pp.3435–3467. doi:[https://doi.org/10.1016/0016-7037\(92\)90390-5](https://doi.org/10.1016/0016-7037(92)90390-5).

SUMMARY

VILNIUS UNIVERSITY FACULTY OF CHEMISTRY AND GEOSCIENCES

AUKSĖ BALTULYTĖ

Microstructural analysis of granites and their alterations in Kabeliai granites: implications from mineral chemical composition

The Mesoproterozoic A-type Kabeliai intrusion, located in southern Lithuania, has attracted attention due to minor differences from the AMCG suite and the A-type Mazury Complex in northern Poland. Of particular interest is the M7 borehole, where disseminated vein-style mineralisation has been identified, containing up to 3% Cu and 1% Mo. The M7 borehole granites are K-feldspar-bearing granitoids intermixed with mafic xenoliths and enclaves, and they exhibit varying degrees of metasomatic alteration, particularly albitization.

This study aimed to investigate the M7 borehole to reconstruct the conditions of intrusion emplacement and subsequent alteration that might be related to Cu-Mo mineralisation. Four thin sections were investigated and analysed using Scanning Electron Microscopy (SEM) with Energy Dispersive Spectrometer (EDS) and Electron Probe Micro-Analyser (EPMA) with Wave-Length Dispersive Spectrometer (WDS). Additionally, multiple geothermometric and geobarometric methods were conducted.

Igneous magma started to crystallise at ~870–847 °C (zircon) and ~850 °C (apatite). The homogenous amphibole average crystallisation temperature was 759 °C, while final solidification was recorded in biotites at an average of 579 °C. The pressure estimates for both amphiboles (avr. 176 MPa) and biotites (avr. 130 MPa) show the upper crust emplacement. The post-magmatic activity and late-stage melt crystallization are marked by the re-equilibration obtained temperatures of apatite, apatite-biotite (773.3 °C and 652 °C) and formation of secondary biotite at 525 °C.

The oxygen fugacity (f_{O_2}) indicates an oxidised magmatic origin, with values around NNO+1. During post-magmatic decompression (average pressure ~97 MPa), f_{O_2} increased to conditions near the hematite–magnetite (HM) buffer, facilitating Cu-Mo mineralisation. This is further supported by the volatile component ratios in secondary biotites, which suggest alteration by a Cl-rich (saline) hydrothermal fluid.

SANTRAUKA

VILNIAUS UNIVERSITETAS CHEMIJOS IR GEOMOKSLŲ FAKULTETAS

AUKSĖ BALTULYTĖ

Granitų ir jų pakitimų Kabelių granituose mikrostruktūrinė analizė: mineralų cheminės sudėties pritaikymas

Pietų Lietuvoje esanti Mezoproterozojaus A-tipo Kabelių intruzija iš šalia esančių šiaurės Lenkijos AMCG (anortozitų – mangeritų – čarnokitų – granitų) ir A-tipo Mozūrų komplekso. Ypač įdomus yra M7 gręžinys, kuriamo nustatyta išsklaidyta gylų tipo mineralizacija, turinti iki 3 % Cu ir 1 % Mo. M7 gręžinio uolienos yra kalio-feldspato turintys granitoidai, su mafiniais ksenolitais. Jie pasižymi įvairaus laipsnio metasomatiniams pakitimais, ypač albitizacija.

Šio tyrimo tikslas buvo ištirti M7 gręžinį, siekiant atkurti intruzijos kristalizacijos istoriją bei vėlesnių pakitimų sąlygas, kurios gali būti susijusios su Cu-Mo mineralizacija. Buvo tiriami keturi šlifai ir atliki skenuojančios elektroninės mikroskopijos (SEM) su energijos dispersijos spektroskopija (EDS) bei elektronų zondavimo mikroanalizės (EPMA) su bangos ilgio dispersijos spektroskopija (WDS) tyrimai. Taip pat buvo pritaikyti keli geotermometriniai ir geobarometriniai metodai.

Nustatyta, kad magminė magma pradėjo kristalizuotis esant ~870–847 °C temperatūrai (pagal cirkoną) ir ~850 °C (pagal apatitą). Homogeninių amfibolų vidutinė kristalizacijos temperatūra siekia 759 °C, o žemiausia kristalizacijos temperatūra nustatyta biotituose - apie 579 °C. Tie amfibolai (vid. 176 MPa), tiek biotitai (vid. 130 MPa) slėgio vertės rodo viršutinės plutos kristalizacijos gylį. Postmagminis aktyvumas ir vėlyvosios stadijos lydalo kristalizacija pasižymi apatito bei apatito-biotito žemesnėmis temperatūromis (773,3 °C ir 652 °C), o antrinis biotitas susiformavo 525 °C temperatūroje.

Deguonies aktyvumas (angl. oxygen fugacity), $f(O_2)$, rodo oksiduotą magminę kilmę, kurios vertės siekia apie NNO+1. Postmagminės dekomprimacijos metu, kai vidutinis slėgis buvo apie 97 MPa, $f(O_2)$ padidėjo iki sąlygų, artimų hematito–magnetito (HM) buferiui. Tokios sąlygos yra palankios Cu-Mo mineralų formavimuisi. Šią išvadą sustiprina lakių komponentų santykiai antriniuose biotituose, kurie rodo Cl praturtinto (druskingo) hidroterminio fluido įtaką.

9. APPENDIX

Appendix list:

1. Whole rock chemistry
2. Mineral Chemistry of the M7 borehole:
 - A) Feldspar
 - B) Biotite
 - C) Amphibole
 - D) Chlorite
 - E) Muscovite
 - F) Carbonates
 - G) Epidote
 - H) Ilmenite
 - I) Hematite
 - J) Sulfide
 - K) Apatite
 - L) Magnetite

1 Appendix
WHOLE ROCK CHEMISTRY

	1*	1*	1*	1*	1*	1*	1*	1*	1*	1*	1*	2*
Borehole	M2	M4	M4	M4	M4	M6	M7	M7	M7	M9	M9	M7
Depth	308-308.2	279.3-279.4	313.5-313.7	355.6	374.1-374.2	318.4	305.4	372.6	385.4	313.1	392.5	293.351
Rock (wt.%)												Granite
SiO ₂	70.1	72.3	73	71.2	71.4	71.77	71.30	69.7	70.1	71.5	70.4	68.06
Al ₂ O ₃	13.6	13.9	13.5	14	13.6	13.15	14.20	14.2	14.1	13.5	14.1	17.26
Fe ₂ O ₃	3.92	2.7	2.76	2.93	3.36	3.51	3.68	4.08	3.57	3.01	3.78	1.18
MgO	0.72	0.49	0.513	0.51	0.499	0.56	0.97	0.694	0.62	0.562	0.68	0.49
CaO	1.74	1.54	1.61	1.61	1.63	1.14	3.23	2.14	1.87	1.38	1.7	0.87
Na ₂ O	2.96	3.31	3.31	3.31	3.28	3.07	4.67	3.48	3.16	3.17	3.33	2.4
K ₂ O	5.48	5.14	5.23	5.23	4.84	5.28	1.17	4.7	5.38	5.09	5.12	10.74
TiO ₂	0.46	0.273	0.307	0.31	0.25	0.31	0.639	0.475	0.38	0.279	0.38	0.3
P ₂ O ₅	0.12	0.08	0.09	0.09	0.09	0.19	0.05	0.16	0.14	0.1	0.12	0.03
MnO	0.06	0.033	0.038	0.04	0.035	0.03	0.044	0.044	0.036	0.034	0.04	0.02
Cr ₂ O ₃						0.001						<0.002
LOI	0.6	0.2	0.4	0.2	0.2	0.1	0.1	0.1	0.1	0.3	0.3	
Sum (ppm)	99.1	99.6	99.2		98.9	99.4	99.9	99.7	99.4	98.6	99.7	99.76
Ba	1143	871	99.6	931	882	600	113	925	1087	1122	1015	1573
Sc	7.1									2.2		1
Co			7.7			4.7				5.6		2.6
Cs						0.7						0.6
Ga						18.2						16.2
Hf						7.1						1.6
Nb	37	6.4	6.3			30.6	30	20	14	9.1		25.1
Rb	220			203		228.6			196		221	301.4
Sn		9.7				3	5.8	5.9	5.9	5.6		<1
Sr	249	158	157	189	157	167.9	233	202	193	392	418	247.7
Ta						4.2						2.2
Th	70			57		73.3			26		41	12.8
Tl						0.7						
U	16			16		3.5			10		16	3.4
V	31	20	21	25	25	25	39	48	42	23	27	9
W	23	21		18	27	<1	22	13	24	16	22	0.8
Zr	385	312	296	266	385	198.2	412	449	327	320	332	56.2
Y	67	28	24	34	13	42	46	43	36	33	51	27.7
La	173	74	83	89	84	147.8	14	116	79	87	120	9.1
Ce	348			167		328.7			154		222	28.9
Pr						27.72						5.09
Nd	150			72		89.7			69		96	22.8
Sm	22			10		14			10		13	4.84
Eu	2.5			1.5		1.08			1.6		1.8	0.73
Gd	17			8		8.17			7.7		9.3	4.63
Tb						1.5						0.75
Dy	15			5.8		9.44			7		8	4.69
Ho	3.2			1.2		1.77			1.6		1.8	0.93
Er	8.9			3.2		5.31			4.3		4.6	2.88
Tm						0.78						0.44
Yb	7.4	3	2.8	2.9	1.7	5.1	5.8	4.8	4.1	3.5	4.6	2.83
Lu	1.1			0.4		0.68			0.6		0.5	0.39
Mo	6	7.7	8.7	6		1	261	12	6	5.6	6	
Cu	46	27	204	19	27	19	489	102	94	28	18	
Pb						6	11	11	11	10		
Zn	28	30	5	22	25	18	24	24	21	177	21	
Ni	6	7.2	6.8			14	20	8.5	5.9	13		<20
As						2						
Cd						0.2						
Sb						0.4						
Bi						0.4						
Be	1.5	1.9	1.5		1.8		3.7	1.9	1.4	1.9		1
Cr	26	13	13		24.1		53	25	20	17		340
CaO/(FeO+MgO+TiO)	0.34	0.44	0.45	0.43	0.40	0.26	0.61	0.41	0.41	0.36	0.35	0.44
CaO+Al ₂ O ₃	15.34	15.44	15.11	15.61	15.23	14.29	17.43	16.34	15.97	14.88	15.80	18.13
FeO/(FeO+MgO)	0.84	0.85	0.84	0.85	0.87	0.86	0.79	0.85	0.85	0.84	0.85	0.71
Al ₂ O ₃ (K ₂ O/Na ₂ O)	7.35	8.95	8.54	8.86	9.22	7.65	56.68	10.51	8.28	8.41	9.17	3.86
T Zr.sat. °C (Watson and Harson, 1983)	888	870	861	852	889	830	867	896	869	875	872	642
T Zr.sat. °C (Boehnke et al., 2013)	870	849	836	827	872	803	833	876	846	856	851	572
T Ap.sat. °C (Harrison and Watson, 1984)	924	905	923	906	908	990	851	951	940	919	927	773

Explanation: Abbreviations: T Zr.Sat. zircon saturation temperature; T Ap.Sat apatite saturation temperature. 1* bulk rock chemistry from Sundblad et al. (1994) and Motuza; 2* bulk rock chemistry from Demina, unpublished data.

2 Appendix
MINERAL CHEMISTRY OF THE M7 BOREHOLE

A) Feldspar

Sample	M7F																																																					
	Microstructures/ wt%		M	M	M	Ph	M	M	M	M	Ph	Ph	M	Ph	M	M	M	M	M	M	Ph	Ph	Ph	Ph	Ph	Ph	Alb	M	M	Alb	M																							
SiO ₂	61.57	62.44	62.42	64.11	62.71	62.15	59.92	60.91	61.42	62.34	62.39	60.70	60.59	65.80	62.47	61.78	62.36	62.30	61.70	62.17	61.75	62.72	62.56	62.05	62.11	61.86	61.87	62.47	62.11	62.09	62.61	62.91	62.16	62.55	62.15	61.60	62.10	61.84	62.46	62.62	62.28	62.65	61.58	68.04	62.30	62.39	68.95	62.54						
Al ₂ O ₃	23.73	23.46	23.51	22.04	22.37	22.67	23.03	23.86	23.68	23.48	22.90	24.15	23.96	17.51	23.51	23.25	23.47	23.27	23.75	22.92	23.59	22.89	23.02	23.21	23.62	23.76	23.14	23.32	23.39	22.96	23.28	23.46	23.27	23.29	23.18	23.61	23.17	23.57	22.89	23.53	23.73	23.69	23.13	24.54	19.46	23.17	23.83	19.18	23.24					
FeO	b.d.l.	b.d.l.	b.d.l.	0.54	1.21	1.44	2.16	0.72	0.31	b.d.l.	b.d.l.	b.d.l.	0.49	0.33	b.d.l.	0.46	0.52	b.d.l.	b.d.l.	b.d.l.																																		
CaO	5.98	5.29	5.68	3.48	3.45	5.05	5.83	6.01	5.16	5.19	5.07	6.01	5.98	b.d.l.	5.24	5.02	5.13	5.26	5.02	5.02	5.21	5.19	4.72	5.25	5.17	5.48	5.22	5.23	5.08	5.00	5.15	5.33	5.07	5.27	5.28	5.44	5.23	4.99	5.13	5.21	5.19	4.91	5.46	3.84	b.d.l.	5.31	5.32	b.d.l.	5.31					
Na ₂ O	8.61	8.70	8.60	9.67	9.21	8.94	8.38	8.52	8.72	8.80	9.27	8.58	8.53	b.d.l.	8.63	8.80	8.91	8.79	8.54	9.04	9.45	9.00	9.21	8.91	8.96	8.74	8.90	8.93	9.02	9.23	8.32	8.61	8.74	8.95	9.03	8.65	8.57	8.95	9.25	8.86	8.83	8.75	9.02	8.16	12.01	9.01	8.87	11.72	9.07					
K ₂ O	0.21	b.d.l.	0.22	0.17	0.73	0.26	0.36	b.d.l.	0.21	0.26	b.d.l.	0.31	b.d.l.	16.80	b.d.l.	0.16	0.20	b.d.l.	0.18	0.36	b.d.l.	0.21	b.d.l.	0.18	0.21	b.d.l.	0.30	0.24	0.30	0.28	0.37	0.21	0.32	0.19	0.39	0.22	0.29	0.23	b.d.l.	0.25	0.28	0.18	b.d.l.	1.30	b.d.l.	0.22	b.d.l.	b.d.l.						
TOTAL	100.1	99.9	100.4	100.0	99.7	100.5	99.7	100.0	99.5	100.1	99.6	99.8	99.6	100.4	99.9	99.0	100.1	99.6	99.5	99.5	100.0	100.3	99.5	99.6	100.1	99.8	99.9	100.2	99.9	99.6	100.1	100.5	99.5	99.4	99.6	99.7	100.5	100.3	100.2	100.3	99.9	100.0	100.4	99.9	100.2									
Atoms per formula unit on the basis of 8 O																																																						
Si	2.74	2.77	2.76	2.84	2.80	2.76	2.71	2.72	2.74	2.76	2.78	2.71	2.71	3.03	2.77	2.77	2.76	2.77	2.75	2.78	2.78	2.77	2.76	2.75	2.76	2.77	2.76	2.77	2.78	2.77	2.77	2.76	2.75	2.75	2.77	2.76	2.78	2.77	2.76	2.77	2.74	2.98	2.77	2.75	3.01	2.77								
Al	1.24	1.23	1.22	1.15	1.18	1.19	1.23	1.25	1.25	1.23	1.20	1.27	1.26	0.95	1.23	1.23	1.23	1.22	1.25	1.21	1.24	1.20	1.21	1.22	1.24	1.24	1.22	1.22	1.23	1.21	1.22	1.22	1.22	1.21	1.24	1.22	1.24	1.20	1.22	1.24	1.23	1.21	1.29	1.01	1.21	1.24	0.99	1.21						
Fe				0.02	0.05	0.05	0.08	0.03	0.01				0.02	0.01					0.01			0.01						0.02			0.01												0.02	0.02										
Ca	0.28	0.25	0.27	0.16	0.17	0.24	0.28	0.29	0.25	0.25	0.24	0.29	0.29	0.00	0.25	0.24	0.24	0.25	0.24	0.24	0.25	0.25	0.23	0.25	0.25	0.26	0.25	0.25	0.24	0.24	0.24	0.25	0.25	0.26	0.25	0.24	0.25	0.25	0.23	0.26	0.18	0.25	0.25	0.25	0.25	0.25								
Na	0.74	0.75	0.74	0.83	0.80	0.77	0.73	0.74	0.76	0.76	0.80	0.74	0.74	0.00	0.74	0.76	0.77	0.76	0.74	0.78	0.81	0.77	0.79	0.77	0.75	0.77	0.77	0.78	0.80	0.72	0.74	0.75	0.77	0.78	0.75	0.74	0.77	0.78	0.80	0.76	0.76	0.75	0.77	0.70	1.02	0.78	0.76	0.99	0.78					
K	0.01		0.01	0.01	0.04	0.01	0.02		0.01		0.02		0.99		0.01	0.01		0.01	0.02		0.01	0.01		0.02	0.01	0.02	0.02	0.01	0.02	0.01	0.02	0.01	0.02	0.01	0.02	0.01	0.07	0.01																
Total	5.0	5.0	5.0	5.0	5.0	5.1	5.0	5.0	5.0	5.0	5.0	5.0	5.0	5.0	5.0	5.0	5.0	5.0	5.0	5.0	5.0	5.0	5.0	5.0	5.0	5.0	5.0	5.0	5.0	5.0	5.0	5.0	5.0	5.0	5.0	5.0	5.0	5.0	5.0	5.0	5.0	5.0	5.0	5.0	5.0	5.0	5.0	5.0	5.0	5.0	5.0	5.0	5.0	5.0
An	27	25	26	16	16	23	27	28	24	24	23	27	28	0	25	24	24	25	24	23	23	24	22	24	24	24	24	23	23	25	24	24	24	25	25	23	23	24	24	23	25	19	0	24	25	0	24							
Ab	71	75	72	83	79	75	71	72	74	74	77	71	72	0	75	75	75	75	77	75	78	75	74	74	75	75	76	73	74	74	75	74	73	74	75	77	74	74	76	75	73	100	75	75	100	76								
Or	1	0	1	1	4	1	2	0	1	1	0	2	0	100	0	1	1	0	1	2	0	1	0	1	1	0	2	1	2	0	1	2	1	2	1	0	8	0	1	0	0	0	0	0	1	0	0	0	0					

Continue

Sample	M7F												M7K																																													
	M	M	Alb	M	M	M	Ph	M	M	Alb	Alb	Alb	Alb	Alb	Alb	Alb	Alb	Alb	Alb																																							
Microstructures/ wt%																																																										
SiO ₂	61.57	62.28	69.14	62.27	63.22	62.18	62.04	65.22	62.46	63.27	65.25	62.68	62.07	62.26	62.55	62.60	63.27	63.01	62.10	62.42	62.52	62.40	62.08	62.37	62.58	62.18	62.12	62.25	62.10	62.29	63.12	62.43	61.93	65.34	67.65	67.73	65.59	65.97	64.41	64.69	70.48	65.05	66.13	67.67	65.62	66.95	68.08											
Al ₂ O ₃	23.74	23.49	19.00	23.75	22.65	23.82	23.46	18.09	23.54	23.05	18.48	23.30	23.75	23.42	23.54	23.37	22.88	23.63	23.51	23.30	23.63	23.78	23.54	23.87	23.55	23.78	23.49	23.84	23.11	23.67	22.87	23.56	23.37	23.47	23.53	21.33	19.64	20.26	21.01	21.30	21.81	21.81	18.31	21.39	20.67	19.48	21.03	20.32	19.29									
FeO	b.d.l.	b.d.l.	b.d.l.	b.d.l.	0.41	b.d.l.																																																				
CaO	5.56	5.60	b.d.l.	5.16	4.84	5.88	5.81	b.d.l.	5.17	4.68	b.d.l.	5.06	4.96	5.10	5.23	4.98	4.14	4.84	5.16	4.97	5.12	5.05	5.26	5.01	5.33	5.14	5.10	5.06	5.27	4.97	4.37	5.14	5.08	5.03	5.08	2.83	0.47	1.22	1.98	2.66	3.21	3.31	2.19	2.73	2.02	0.66	2.23	1.31	0.36									
Na ₂ O	8.53	8.77	11.90	8.79	9.08	8.55	8.32	0.63	8.89	9.39	0.60	8.88	9.02	9.03	8.72	8.89	8.99	8.88	8.96	9.30	8.97	8.98	8.95	8.91	9.09	9.16	8.98	8.91	9.00	9.44	8.68	8.87	8.67	9.17	10.36	11.76	11.04	11.20	10.34	10.23	10.39	9.31	10.34	10.73	11.59	10.85	11.31	11.87										
K ₂ O	0.19	b.d.l.	b.d.l.	0.19	b.d.l.	b.d.l.	0.23	15.85	0.22	0.19	15.58	0.20	b.d.l.	0.22	0.27	0.20	0.58	b.d.l.	b.d.l.	0.18	b.d.l.	0.15	0.23	b.d.l.	0.25	0.00	0.18	0.00	0.22	0.20	0.20	0.24	0.35	b.d.l.	b.d.l.	0.20	b.d.l.	b.d.l.	0.14	b.d.l.	b.d.l.	0.14	0.16	0.14	0.19	b.d.l.	b.d.l.											
TOTAL	99.6	100.1	100.0	100.2	100.4	99.9	99.8	100.3	100.6	100.3	100.1	99.8	100.0	100.3	100.0	100.3	100.4	99.7	100.2	100.4	100.1	100.2	100.0	100.1	99.6	100.1	100.0	100.0	100.2	100.0	99.7	99.9	100.3	99.8	100.2	100.3	99.7	99.7	99.5	99.9	99.9	99.6																

Atoms per formula unit on the basis of 8 O																																																		
Si	2.74	2.76	3.02	2.76	2.80	2.75	2.76	3.01	2.76	2.79	3.00	2.77	2.76	2.76	2.77	2.80	2.78	2.76	2.77	2.76	2.76	2.76	2.76	2.75	2.76	2.76	2.76	2.77	2.76	2.77	2.77	2.76	2.88	2.97	2.96	2.89	2.89	2.85	2.85	3.05	2.88	2.92	2.98	2.89	2.94	2.99				
Al	1.25	1.23	0.98	1.24	1.18	1.24	1.23	1.00	1.23	1.20	1.00	1.22	1.24	1.22	1.23	1.22	1.19	1.23	1.23	1.22	1.23	1.24	1.23	1.24	1.22	1.24	1.23	1.24	1.24	1.21	1.24	1.19	1.23	1.22	1.23	1.23	1.11	1.02	1.04	1.09	1.10	1.14	1.13	0.93	1.11	1.07	1.01	1.09	1.05	1.00
Fe					0.02																																													
Ca	0.27	0.27		0.24	0.23	0.28	0.28		0.25	0.22		0.24	0.24	0.24	0.25	0.24	0.20	0.23	0.25	0.24	0.24	0.25	0.24	0.25	0.24	0.24	0.25	0.24	0.21	0.24	0.24	0.24	0.24	0.24	0.13	0.02	0.06	0.09	0.12	0.15	0.16	0.10	0.13	0.10	0.03	0.11	0.06	0.02		
Na	0.74	0.75	1.01	0.75	0.78	0.73	0.72	0.05	0.76	0.80	0.05	0.76	0.78	0.78	0.75	0.76	0.77	0.76	0.77	0.77	0.76	0.78	0.79	0.77	0.76	0.77	0.77	0.81	0.75	0.76	0.75	0.79	0.89	1.00	0.93	0.96	0.88	0.88	0.89	0.78	0.89	0.92	0.99	0.93	0.96	1.01				
K	0.01			0.01				0.01	0.90	0.01	0.01	0.91	0.01			0.01	0.02	0.01	0.03			0.01	0.01	0.01	0.01	0.01	0.01	0.01	0.01	0.01	0.01	0.01	0.01	0.01	0.01	0.01	0.01	0.01	0.01	0.01	0.01	0.01	0.01	0.01	0.01	0.01	0.01	0.01	0.01	
Total	5.0	5.0	5.0	5.0	5.0	5.0	5.0	5.0	5.0	5.0	5.0	5.0	5.0	5.0	5.0	5.0	5.0	5.0	5.0	5.0	5.0	5.0	5.0	5.0	5.0	5.0	5.0	5.0	5.0	5.0	5.0	5.0	5.0	5.0	5.0	5.0	5.0	5.0	5.0	5.0	5.0	5.0	5.0	5.0						
An	26	26	0	24	23	28	27	0	24	21	0	24	23	23	25	23	20	23	24	23	24	24	24	24	24	24	24	24	24	24	24	24	24	23	13	2	6	9	12	15	15	12	13	9	3	10	6	2		
Ab	73	74	100	75	77	72	71	5	75	78	6	75	77	75	74	76	77	77	76	76	76	75	76	75	76	74	76	79	74	75	74	77	87	97	94	91	88	85	85	88	87	90	96	89	94	98				
Or	1	0	0	1	0	0	1	95	1	1	94	1	0	1	2	1	3	0	0	1	0	1	1	0	1	0	1	1	1	2	0	0	1	0	0	0	1	0	1	1	1	0	0							

Continue

Sample	M7S																																											
	Microstructures/ wt%		Alb	M	Alb	M	Alb	M	Ph	Ph	Alb	Ph	M	M	Ph	Ph	Alb	Ph	My	My	My	My	My	My																				
SiO ₂	62.99	62.09	63.52	62.53	64.74	62.14	64.93	65.14	68.88	61.89	62.44	64.39	64.21	62.63	62.12	68.58	62.05	62.40	61.85	62.59	62.39	62.24	62.40	63.17	62.40	62.00	61.57	62.28	62.61	62.11	62.01	62.44	62.33	61.60	62.20	61.76	62.57	62.27	62.31	62.96	62.44	61.93	62.46	63.29
Al ₂ O ₃	22.56	23.46	23.00	22.88	21.29	23.46	18.41	18.27	19.63	23.41	23.25	22.08	22.64	23.65	23.66	19.34	23.61	23.38	23.91	23.42	23.40	24.06	23.40	23.39	23.57	23.72	23.63	23.49	23.72	23.90	23.24	23.51	23.64	23.33	23.62	23.54	23.26	23.44	22.73	22.92	23.26	23.37	23.55	23.13
FeO	b.d.l.	b.d.l.	b.d.l.	b.d.l.	b.d.l.	b.d.l.	b.d.l.	b.d.l.	b.d.l.	b.d.l.	b.d.l.	b.d.l.	b.d.l.	b.d.l.	b.d.l.	b.d.l.	b.d.l.	b.d.l.	b.d.l.	b.d.l.	b.d.l.	b.d.l.	b.d.l.	b.d.l.	b.d.l.	b.d.l.	b.d.l.	b.d.l.	b.d.l.	b.d.l.	b.d.l.	b.d.l.	b.d.l.	b.d.l.	b.d.l.	b.d.l.	b.d.l.	b.d.l.	b.d.l.	b.d.l.	b.d.l.	b.d.l.		
CaO	4.42	5.08	4.41	4.53	2.66	5.34	b.d.l.	b.d.l.	b.d.l.	4.81	5.02	3.36	3.38	5.19	5.17	0.18	5.06	5.27	5.40	5.11	5.16	5.41	5.53	5.09	4.65	5.18	5.40	5.49	5.14	5.46	5.10	5.38	5.28	5.28	5.09	4.95	5.31	5.04	5.00	4.48	4.93	5.34	5.27	4.48
Na ₂ O	9.79	8.51	9.60	9.17	10.48	9.01	0.65	0.59	12.30	9.07	9.05	9.95	9.91	8.88	8.77	11.87	8.86	8.93	8.74	8.80	8.74	8.85	8.59	9.05	8.90	8.78	8.75	8.77	8.73	9.01	8.72	8.51	8.80	8.74	8.63	8.70	8.75	8.88	9.01	9.55	9.07	8.79	8.74	9.29
K ₂ O	b.d.l.	0.33	b.d.l.	0.15	0.17	0.17	15.86	15.85	0.16	0.19	0.20	0.15	b.d.l.	0.27	b.d.l.	b.d.l.	0.20	0.14	0.32	0.35	0.25	0.18	0.19	0.30	0.26	0.49	0.26	0.27	b.d.l.	0.37	0.31	0.31	0.22	0.24	0.21	0.19	0.18	b.d.l.	b.d.l.	0.15	0.16	0.34	b.d.l.	
TOTAL	99.8	99.5	100.5	99.3	99.3	100.1	99.9	99.9	101.0	99.4	100.0	99.9	100.1	100.4	100.0	100.0	99.6	100.2	100.0	100.2	100.0	100.8	100.1	100.9	100.1	100.3	99.8	100.3	100.5	100.5	99.7	100.2	100.4	99.2	99.8	99.2	100.4	99.8	99.1	99.9	99.9	99.6	100.4	100.2
Atoms per formula unit on the basis of 8 O																																												
Si	2.80	2.77	2.80	2.79	2.87	2.76	3.00	3.01	2.99	2.76	2.77	2.84	2.83	2.76	2.76	3.00	2.76	2.76	2.74	2.77	2.77	2.74	2.77	2.77	2.74	2.77	2.75	2.74	2.76	2.76	2.74	2.76	2.76	2.76	2.76	2.76	2.77	2.79	2.79	2.77	2.76	2.76	2.79	
Al	1.18	1.23	1.19	1.20	1.11	1.23	1.00	0.99	1.00	1.23	1.22	1.15	1.18	1.23	1.24	1.00	1.24	1.22	1.25	1.22	1.22	1.25	1.22	1.21	1.23	1.24	1.24	1.23	1.23	1.24	1.22	1.22	1.23	1.23	1.24	1.21	1.23	1.20	1.22	1.23	1.23	1.20		
Fe																																												
Ca	0.21	0.24	0.21	0.22	0.13	0.25	0.00	0.00	0.00	0.23	0.24	0.16	0.16	0.25	0.25	0.01	0.24	0.25	0.26	0.24	0.25	0.26	0.26	0.24	0.22	0.25	0.26	0.26	0.24	0.24	0.26	0.25	0.25	0.24	0.24	0.25	0.24	0.21	0.23	0.25	0.25	0.21		
Na	0.84	0.74	0.82	0.79	0.90	0.78	0.06	0.05	1.03	0.78	0.78	0.85	0.85	0.76	0.75	1.01	0.76	0.77	0.75	0.76	0.75	0.76	0.74	0.77	0.76	0.75	0.76	0.75	0.77	0.75	0.73	0.75	0.76	0.74	0.75	0.75	0.76	0.78	0.82	0.78	0.76	0.75	0.79	
K		0.02		0.01	0.01	0.01	0.93	0.93	0.01	0.01	0.01	0.01					0.02			0.01	0.01	0.02	0.02	0.01	0.01	0.02	0.01	0.03	0.01	0.02		0.02	0.02	0.02	0.01	0.01	0.01	0.01	0.01	0.01	0.01	0.02		
Total	5.0	5.0	5.0	5.0	5.0	5.0	5.0	5.0	5.0	5.0	5.0	5.0	5.0	5.0	5.0	5.0	5.0	5.0	5.0	5.0	5.0	5.0	5.0	5.0	5.0	5.0	5.0	5.0	5.0	5.0	5.0	5.0	5.0	5.0	5.0	5.0	5.0	5.0	5.0	5.0	5.0	5.0	5.0	5.0
An	20	24	20	21	12	24	0	0	0	22	23	16	16	24	24	1	24	24	25	24	24	25	26	23	22	24	25	25	24	25	24	25	24	24	25	24	25	24	23	21	23	25	25	21
Ab	80	74	80	78	87	75	6	5	99	77	76	84	84	76	74	99	76	75	74	74	74	73	75	76	74	73	73	74	75	74	74	75	75	77	79	76	74	74	79	77	76	74	74	79
Or	0	2	0	1	1	1	94	95	1	1	1	1	0	0	2	0	0	1	1	2	2	1	1	1	2	1	3	1	2	0	2	2	2	1	1	1	1	1	0	0	1	1	2	0

Continue

Sample	M7M																																							
Microstructures/ wt%	Ph	Ph	Alb	Ph	My	My	My	My	My	My																														
SiO ₂	62.16	62.20	63.40	62.16	62.27	61.66	62.46	63.36	62.30	62.65	62.29	62.61	62.44	62.21	62.42	62.01	62.01	62.00	62.63	62.67	61.54	65.57	62.06	62.55	61.86	62.79	62.81	62.39	64.92	62.75	65.28	63.01	61.39	61.73	62.26	62.49	62.17	62.29	64.09	62.32
Al ₂ O ₃	23.53	23.39	22.56	23.67	24.07	23.55	23.70	22.73	23.59	23.58	23.34	23.35	23.62	23.13	23.43	22.82	23.32	23.69	23.30	23.36	23.63	18.10	23.32	23.44	23.62	23.03	23.29	22.99	18.45	23.54	18.47	23.06	24.12	23.68	23.60	23.08	23.44	23.84	22.92	23.63
FeO	b.d.l.																																							
CaO	5.27	5.39	4.09	5.47	5.56	5.30	5.32	5.01	5.31	5.07	5.31	5.00	5.10	4.85	5.06	5.16	5.36	5.20	5.40	4.98	5.42	0.00	5.14	5.33	5.38	5.11	5.28	5.53	b.d.l.	5.15	b.d.l.	4.48	5.75	5.24	5.11	5.14	4.94	5.12	3.82	5.31
Na ₂ O	9.02	8.94	9.77	8.67	8.28	8.96	8.56	8.92	8.83	8.91	8.82	8.91	8.83	8.81	8.98	8.99	8.71	9.23	8.92	9.10	9.20	0.48	8.91	8.89	9.00	9.03	8.68	8.98	0.66	9.14	0.41	9.27	8.65	9.04	8.60	9.05	9.19	8.87	9.44	8.94
K ₂ O	b.d.l.	0.15	b.d.l.	0.22	b.d.l.	b.d.l.	0.31	0.26	0.34	b.d.l.	0.35	0.18	0.25	0.30	0.34	0.31	0.33	0.15	0.22	b.d.l.	b.d.l.	16.09	0.30	0.14	0.17	0.35	0.30	0.41	15.89	b.d.l.	16.30	b.d.l.	b.d.l.	0.15	0.24	0.20	b.d.l.	0.17	b.d.l.	0.15
TOTAL	100.0	100.1	99.8	100.2	100.2	99.5	100.4	100.3	100.4	100.2	100.1	100.1	100.2	99.5	100.2	99.3	100.0	100.3	100.5	100.1	99.8	100.2	99.7	100.4	100.0	100.3	100.4	100.3	99.9	100.6	100.5	99.8	99.9	99.8	99.8	100.2	99.7	100.3	100.4	
Atoms per formula unit on the basis of 8 O																																								
Si	2.76	2.76	2.81	2.75	2.75	2.76	2.80	2.76	2.77	2.76	2.77	2.76	2.77	2.76	2.76	2.75	2.77	2.77	2.74	3.02	2.76	2.77	2.75	2.78	2.78	2.77	3.00	2.77	3.00	2.79	2.73	2.75	2.76	2.77	2.76	2.82	2.76			
Al	1.23	1.22	1.18	1.24	1.25	1.24	1.23	1.18	1.23	1.23	1.22	1.22	1.23	1.22	1.22	1.20	1.22	1.24	1.21	1.22	1.24	0.98	1.22	1.22	1.24	1.20	1.21	1.20	1.00	1.22	1.00	1.20	1.26	1.24	1.23	1.21	1.23	1.24	1.19	1.23
Fe																																								
Ca	0.25	0.26	0.19	0.26	0.26	0.25	0.25	0.24	0.25	0.24	0.25	0.24	0.23	0.24	0.25	0.26	0.25	0.26	0.24	0.26	0.26	0.25	0.25	0.26	0.24	0.25	0.26	0.26	0.24	0.24	0.24	0.24	0.24	0.24	0.24	0.18	0.25			
Na	0.78	0.77	0.84	0.74	0.71	0.78	0.73	0.76	0.76	0.76	0.77	0.76	0.76	0.77	0.78	0.75	0.79	0.76	0.78	0.79	0.04	0.77	0.76	0.78	0.77	0.74	0.77	0.06	0.78	0.04	0.80	0.75	0.78	0.74	0.78	0.79	0.76	0.80	0.77	
K		0.01		0.01		0.02	0.01	0.02		0.02	0.01	0.01	0.02	0.02	0.02	0.01	0.01			0.94	0.02	0.01	0.01	0.02	0.02	0.02	0.94		0.96		0.01	0.01	0.01		0.01	0.01		0.01		
Total	5.0	5.0	5.0	5.0	5.0	5.0	5.0	5.0	5.0	5.0	5.0	5.0	5.0	5.0	5.0	5.0	5.0	5.0	5.0	5.0	5.0	5.0	5.0	5.0	5.0	5.0	5.0	5.0	5.0	5.0	5.0	5.0	5.0	5.0	5.0	5.0				
An	24	25	19	26	27	25	25	23	24	24	23	24	23	23	24	25	24	25	23	25	0	24	25	25	23	25	25	0	24	0	21	27	24	24	24	23	24	18	25	
Ab	76	74	81	73	73	75	73	75	74	76	74	76	75	75	75	73	76	74	77	75	4	75	75	74	75	74	73	6	76	4	79	73	75	74	75	77	75	82	75	
Or	0	1	0	1	0	0	2	1	2	0	2	1	1	2	2	2	2	1	1	0	0	96	2	1	1	2	2	2	94	0	96	0	0	1	1	1	0	1	0	

Explanation: Microstructures: Ab – albitized; M – matrix; My – myrmekite; Ph – phenocryst. End members: Ab – albite; An – anorthite; Or – orthoclase.

Explanation: Re – re-equilibrated biotite; Sec – secondary; Re M and Sec M – biotite from mafic xenolith; * - biotite used for apatite-biotite geothermometer.

E) Muscovite

	M7S																			
Wt.%																				
SiO ₂	45.79	45.71	45.26	45.40	45.25	47.26	45.78	45.49	45.47	45.26	46.28	45.85	47.02	45.02	45.03	45.72	45.02	45.77	45.58	45.15
TiO ₂	1.57	1.06	1.36	0.85	0.96	1.26	0.81	1.23	1.19	1.51	1.73	1.09	0.94	0.47	1.31	1.21	1.47	0.88	0.42	1.61
Al ₂ O ₃	29.13	29.12	28.93	28.66	29.08	29.76	28.89	29.22	29.25	29.29	27.51	28.40	29.35	29.65	28.66	28.71	29.09	30.58	29.55	28.91
FeO	3.89	4.25	3.84	4.23	3.83	3.70	3.80	4.12	3.61	3.99	3.89	3.68	4.14	4.09	3.74	3.91	4.29	3.93	3.90	3.87
MnO	b.d.l.	0.24	b.d.l.	b.d.l.	b.d.l.															
MgO	1.68	1.72	1.56	1.70	1.57	1.75	1.81	1.67	1.45	1.56	1.75	1.54	1.87	1.58	1.44	1.82	1.84	1.48	1.77	1.57
CaO	b.d.l.	b.d.l.	b.d.l.	b.d.l.	0.26	b.d.l.	0.41	0.37	b.d.l.	b.d.l.	b.d.l.									
Na ₂ O	b.d.l.	0.26	b.d.l.	b.d.l.	b.d.l.	b.d.l.	0.63	b.d.l.	b.d.l.	b.d.l.	b.d.l.	b.d.l.	b.d.l.	0.21	b.d.l.	b.d.l.	0.22	0.26	b.d.l.	b.d.l.
K ₂ O	10.88	10.74	10.47	10.78	10.47	11.09	10.51	10.90	10.80	10.56	10.64	10.90	10.71	10.66	10.70	10.33	10.56	10.71	10.66	10.76
BaO	b.d.l.	b.d.l.	b.d.l.	b.d.l.	b.d.l.	b.d.l.	0.88	0.82	0.80	0.67	b.d.l.	0.58	0.94	0.94	b.d.l.	b.d.l.	b.d.l.	b.d.l.	b.d.l.	b.d.l.
F	0.80	b.d.l.	0.62	b.d.l.	b.d.l.	b.d.l.	b.d.l.													
Cl	b.d.l.																			
H ₂ O	3.93	4.30	4.25	4.24	4.25	4.41	4.28	4.30	4.27	4.29	4.27	4.25	4.38	4.26	4.23	3.99	4.29	4.35	4.27	4.26
Total	97.33	97.16	95.67	95.86	95.67	99.23	96.51	97.81	96.86	97.26	96.74	95.71	98.99	96.88	96.05	96.46	97.39	97.96	96.15	96.13
Structural formula based on 11 oxygen atoms																				
Si	6.37	6.38	6.39	6.41	6.39	6.43	6.41	6.35	6.38	6.33	6.50	6.47	6.44	6.34	6.38	6.41	6.29	6.31	6.40	6.36
Ti	0.16	0.11	0.14	0.09	0.10	0.13	0.09	0.13	0.13	0.16	0.18	0.12	0.10	0.05	0.14	0.13	0.15	0.09	0.04	0.17
Al ^{IV}	1.63	1.62	1.61	1.59	1.61	1.57	1.59	1.65	1.62	1.67	1.50	1.53	1.56	1.66	1.62	1.59	1.71	1.69	1.60	1.64
Al ^{VI}	3.15	3.16	3.20	3.19	3.23	3.19	3.18	3.15	3.21	3.16	3.05	3.20	3.18	3.25	3.17	3.15	3.07	3.28	3.29	3.15
Fe	0.45	0.50	0.45	0.50	0.45	0.42	0.45	0.48	0.42	0.47	0.46	0.43	0.47	0.48	0.44	0.46	0.50	0.45	0.46	0.46
Mn																	0.03			
Mg	0.35	0.36	0.33	0.36	0.33	0.35	0.38	0.35	0.30	0.33	0.37	0.32	0.38	0.33	0.30	0.38	0.38	0.30	0.37	0.33
Ca					0.04											0.06	0.06			
Na		0.07						0.17								0.06		0.06	0.07	
K	1.93	1.91	1.88	1.94	1.89	1.92	1.88	1.94	1.93	1.88	1.91	1.96	1.87	1.91	1.94	1.85	1.88	1.88	1.91	1.93
Ba									0.05	0.05	0.04	0.04		0.03	0.05	0.05				
OH*	3.65	4.00	4.00	4.00	4.00	4.00	4.00	4.00	4.00	4.00	4.00	4.00	4.00	4.00	4.00	3.73	4.00	4.00	4.00	4.00
F	0.35															0.27				
Cl																				
TOTAL	18.04	18.11	18.01	18.08	18.03	18.02	18.14	18.09	18.04	18.04	18.00	18.03	18.03	18.14	18.05	18.02	18.14	18.09	18.07	18.04
Al total	4.78	4.79	4.81	4.77	4.84	4.77	4.77	4.80	4.84	4.83	4.55	4.72	4.74	4.92	4.79	4.74	4.79	4.97	4.89	4.80
Fe/Fe+Mg	0.57	0.58	0.58	0.58	0.58	0.54	0.54	0.58	0.58	0.59	0.55	0.57	0.55	0.59	0.59	0.55	0.57	0.60	0.55	0.58

F) Carbonate

Wt% element	M7F						M7F	M7K	M7S			
	Siderite						Calcite	Calcite	Calcite	Calcite	Calcite	Calcite
CaO	5.83	4.38	4.23	3.86	1.32	1.36	1.05	52.01	51.67	52.89	52.97	52.79
MgO	1.82	4.36	4.16	3.05	0.43	0.75	0.50	b.d.l.	b.d.l.	b.d.l.	b.d.l.	b.d.l.
MnO	1.18	1.50	1.38	1.85	1.19	0.99	0.67	0.75	0.57	b.d.l.	b.d.l.	b.d.l.
FeO	49.21	47.43	48.60	49.68	56.33	56.49	57.49	0.53	1.27	b.d.l.	b.d.l.	b.d.l.
CO ₂	37.44	38.18	38.49	37.94	36.75	37.10	37.00	41.60	41.68	41.51	41.57	41.43
Total	95.48	95.85	96.86	96.38	96.02	96.69	96.71	94.89	95.20	94.39	94.54	94.22
Atoms per formula unit on the basis of 6 O												
Ca	0.24	0.18	0.17	0.16	0.06	0.06	0.04	1.96	1.95	2.00	2.00	2.00
Mg	0.11	0.25	0.24	0.18	0.03	0.04	0.03					
Mn	0.04	0.05	0.04	0.06	0.04	0.03	0.02	0.02	0.02			
Fe	1.61	1.52	1.55	1.60	1.88	1.87	1.90	0.02	0.04			
C	2	2	2	2	2	2	2	2	2	2	2	2
% carbonate composition												
CaCO ₃	12.23	9.00	8.62	7.99	2.81	2.87	2.23	98.11	97.28	100.00	100.00	100.00
MgCO ₃	5.32	12.47	11.80	8.78	1.28	2.20	1.47					
MnCO ₃	1.95	2.43	2.23	3.02	2.01	1.66	1.13	1.12	0.85			
FeCO ₃	80.51	76.10	77.35	80.21	93.90	93.27	95.18	0.78	1.87			
Total	100	100	100	100	100	100	100	100	100	100	100	100

G) Epidote

	M7F epidotes													
Wt%														
SiO ₂	36.18	37.40	36.77	36.76	36.92	37.63	37.92	38.25	38.07	38.00	37.11	38.02	37.18	38.55
TiO ₂	b.d.l.	b.d.l.	b.d.l.	b.d.l.	b.d.l.	b.d.l.	b.d.l.	b.d.l.	b.d.l.	b.d.l.	b.d.l.	b.d.l.	b.d.l.	b.d.l.
Al ₂ O ₃	23.17	27.12	22.86	23.92	22.68	23.45	23.63	28.29	22.62	23.87	22.18	23.75	22.68	25.05
Fe ₂ O ₃	10.91	6.41	12.30	10.44	12.25	13.41	12.45	7.28	13.13	12.93	13.79	12.36	12.71	10.79
MnO	b.d.l.	b.d.l.	0.35	0.34	b.d.l.	b.d.l.	b.d.l.	0.47	b.d.l.	b.d.l.	b.d.l.	b.d.l.	b.d.l.	b.d.l.
MgO	b.d.l.	b.d.l.	b.d.l.	b.d.l.	b.d.l.	b.d.l.	b.d.l.	b.d.l.	b.d.l.	b.d.l.	b.d.l.	b.d.l.	b.d.l.	b.d.l.
CaO	22.90	23.70	23.67	23.04	22.43	23.89	23.61	23.38	23.65	23.47	22.82	23.33	22.47	23.74
SrO	b.d.l.	b.d.l.	b.d.l.	b.d.l.	b.d.l.	b.d.l.	b.d.l.	b.d.l.	b.d.l.	b.d.l.	b.d.l.	b.d.l.	b.d.l.	b.d.l.
Na ₂ O	b.d.l.	b.d.l.	b.d.l.	b.d.l.	b.d.l.	b.d.l.	b.d.l.	b.d.l.	b.d.l.	b.d.l.	b.d.l.	b.d.l.	b.d.l.	b.d.l.
K ₂ O	b.d.l.	b.d.l.	b.d.l.	b.d.l.	b.d.l.	b.d.l.	b.d.l.	b.d.l.	b.d.l.	b.d.l.	b.d.l.	b.d.l.	b.d.l.	b.d.l.
TOTAL	93.16	94.63	95.95	94.50	94.28	98.38	97.61	97.67	97.47	98.27	95.90	97.46	95.04	98.13
Structural formula based on 25 oxygen atoms														
Formula														
Si	6.37	6.59	6.48	6.47	6.50	6.63	6.68	6.74	6.70	6.69	6.54	6.70	6.55	6.79
Ti														
Al	4.81	5.63	4.74	4.96	4.71	4.87	4.90	5.87	4.69	4.95	4.60	4.93	4.71	5.20
Fe ³⁺	0.72	0.42	0.81	0.69	0.81	0.89	0.83	0.48	0.87	0.86	0.91	0.82	0.84	0.72
Mn			0.05	0.05				0.07						
Mg														
Ca	4.32	4.47	4.47	4.35	4.23	4.51	4.45	4.41	4.46	4.43	4.31	4.40	4.24	4.48
Sr														
Na														
K														
TOTAL	16.22	17.11	16.55	16.53	16.25	16.89	16.86	17.57	16.73	16.93	16.36	16.85	16.34	17.18

H) Ilmenite

	Ilmenite					
	M7F	M7K		M7S		
Wt%						
SiO ₂	5.05	b.d.l.	b.d.l.	0.56	b.d.l.	0.34
TiO ₂	45.75	49.56	49.46	49.11	46.94	48.80
Al ₂ O ₃	2.34	b.d.l.	b.d.l.	b.d.l.	b.d.l.	b.d.l.
Fe ₂ O ₃	3.22	3.96	4.25	3.40	8.84	5.61
FeO	39.69	35.43	35.61	27.36	27.42	27.93
MnO	2.20	9.03	8.53	17.26	14.61	16.16
MgO	2.64	b.d.l.	b.d.l.	b.d.l.	b.d.l.	b.d.l.
CaO	0.44	b.d.l.	0.19	b.d.l.	b.d.l.	b.d.l.
TOTAL	101.33	97.99	98.04	97.69	97.82	98.84
Atoms units per 6 oxygen						
Si	0.24	0.00	0.00	0.03		0.02
Ti	1.64	1.92	1.92	1.91	1.83	1.87
Al	0.13					
Fe ³⁺	0.12	0.15	0.16	0.13	0.34	0.22
Fe ²⁺	1.58	1.53	1.53	1.18	1.19	1.19
Mn	0.09	0.39	0.37	0.75	0.64	0.70
Mg	0.19					
Ca	0.02		0.01			
TOTAL	4	4	4	4	4	4

I) Hematite

	Hematite								
	M7M								
	D	D	D	D	D	N	N	N	N
Point#	3	5	6	7	8	9	10	1	14
SiO ₂	b.d.l.	b.d.l.	b.d.l.	b.d.l.	b.d.l.	b.d.l.	b.d.l.	0.02	b.d.l.
TiO ₂	b.d.l.	b.d.l.	b.d.l.	b.d.l.	b.d.l.	b.d.l.	b.d.l.	b.d.l.	b.d.l.
Al ₂ O ₃	0.08	0.10	0.12	0.11	0.17	0.12	0.08	0.08	0.10
Cr ₂ O ₃	0.09	0.08	0.06	0.08	0.08	0.06	0.07	0.07	0.08
V ₂ O ₃	0.23	0.16	0.21	0.21	0.25	0.22	0.20	0.21	0.23
Fe ₂ O ₃	99.35	99.54	99.49	99.52	99.32	98.76	98.80	98.24	98.94
FeO	0.00	b.d.l.	0.00	b.d.l.	0.00	b.d.l.	0.00	0.02	b.d.l.
MnO	b.d.l.	b.d.l.	b.d.l.	b.d.l.	0.01	b.d.l.	b.d.l.	b.d.l.	b.d.l.
MgO	0.01	0.00	0.06	b.d.l.	b.d.l.	b.d.l.	0.01	b.d.l.	b.d.l.
CaO	b.d.l.	b.d.l.	b.d.l.	b.d.l.	b.d.l.	b.d.l.	b.d.l.	b.d.l.	b.d.l.
ZnO	b.d.l.	b.d.l.	b.d.l.	b.d.l.	0.26	b.d.l.	b.d.l.	b.d.l.	b.d.l.
TOTAL	99.76	99.89	99.94	99.92	100.09	99.16	99.17	98.64	99.36
Atoms per formula unit on the basis of 6 O									
Si								0.00	
Ti									
Al	0.01	0.01	0.01	0.01	0.01	0.01	0.01	0.01	0.01
Fe ³⁺	3.99	3.99	3.99	3.99	3.99	3.99	3.99	3.99	3.99
Fe ²⁺	0.00		0.00		0.00		0.00	0.00	0.00
Mn	0.00	0.00	0.00	0.00	0.00	0.00	0.00	0.00	0.00
Mg	0.00	0.00	0.00	0.00	0.00	0.00	0.00	0.00	0.00
Ca	0.00	0.00	0.00	0.00	0.00	0.00	0.00	0.00	0.00
TOTAL	4	4	4	4	4	4	4	4	4

Explanation: N – normal grey zone; D – darker grey zone

J) Sulfide

wt.%	M7F		M7M		M7S		
	Pyrite	Sphalerite	Pyrite		Pyrite		
Zn		55.87					
Fe	48.14	0.32	45	44.86	47.2	46.56	47.52
S	39.94	31.17	53.04	53.49	53.67	54.17	53.88
Total	88.08	87.36	98.04	98.35	100.87	100.73	101.4
Number of Sulfur 13							
Zn		0.47					
Fe	0.41	0.00	0.33	0.32	0.34	0.33	0.34
S	0.59	0.53	0.67	0.68	0.66	0.67	0.66
Total	1	1	1	1	1	1	1

L) Magnetite

	M7M					M7K
	L	L	L	L	L	N
Point#	11	12	13	2	4	1
SiO ₂	b.d.l.	b.d.l.	0.0904	b.d.l.	b.d.l.	0.02
TiO ₂	0.06	b.d.l.	b.d.l.	b.d.l.	b.d.l.	b.d.l.
Al ₂ O ₃	0.09	0.09	0.10	0.07	0.11	b.d.l.
Cr ₂ O ₃	0.09	0.08	0.08	0.09	0.08	b.d.l.
V ₂ O ₃	0.27	0.27	0.22	0.16	0.19	0.15
Fe ₂ O ₃	68.08	68.08	67.72	68.28	67.94	68.57
FeO	30.97	30.92	30.87	31.01	30.85	30.86
MnO	b.d.l.	b.d.l.	b.d.l.	b.d.l.	b.d.l.	b.d.l.
MgO	b.d.l.	b.d.l.	b.d.l.	b.d.l.	b.d.l.	b.d.l.
CaO	b.d.l.	b.d.l.	b.d.l.	b.d.l.	b.d.l.	0.19
ZnO	b.d.l.	b.d.l.	b.d.l.	b.d.l.	b.d.l.	b.d.l.
TOTAL	99.56	99.43	99.08	99.61	99.17	99.80
Atoms per formula unit on the basis of 32 O						
Si			0.03			0.01
Ti	0.01					
Al	0.03	0.03	0.04	0.03	0.04	
Cr	0.02	0.02	0.02	0.02	0.02	
V	0.07	0.07	0.05	0.04	0.05	0.04
Fe ³⁺	15.85	15.88	15.83	15.91	15.89	15.95
Fe ²⁺	8.01	8.02	8.02	8.03	8.02	7.98
Mn						
Mg						
Ca						0.06
Zn						
TOTAL	24.00	24.02	23.99	24.03	24.02	24.03

Explanation: N – normal grey zone; D – darker grey zone